# Simulations of the muon-induced neutron background of the EDELWEISS-II experiment for Dark Matter search

Zur Erlangung des akademischen Grades eines
DOKTORS DER NATURWISSENSCHAFTEN
von der Fakultät für Physik der
Universität Karlsruhe (TH)

genehmigte

DISSERTATION

von

Dipl. Phys. Oliver Markus Horn
aus Heidelberg

Tag der mündlichen Prüfung: 21.12.2007

Referent: Prof. Dr. J. Blümer
Institut für Experimentelle Kernphysik, Universität Karlsruhe (TH)
Korreferent: Prof. Dr. J. Jochum
Physikalisches Institut, Eberhard-Karls Universität Tübingen

# Zusammenfassung

Ein Schwerpunkt in der Astroteilchenphysik ist die Frage nach der Natur der Dunklen Materie. Die wohl vielversprechendste Hypothese geht davon aus, dass es sich hierbei um bisher unentdeckte Elementarteilchen handelt, den sogenannten WIMPs. Das EDELWEISS Experiment versucht, diese direkt über Kernrückstöße an Germaniumkernen in kryogenen Bolometern nachzuweisen. Um eine Diskriminierung der sehr seltenen Kernrückstöße von häufigen Elektronenrückstößen auf der Basis einzelner Ereignisse zu erzielen, wird ein Energieeintrag in jeweils zwei Signalen ausgelesen, als Temperaturanstieg und als Ionisation des Halbleiters. Bei dieser experimentellen Technik verbleiben Neutronen als Hauptuntergrundquelle.
Außer durch ($\alpha$,n) Reaktionen der natürlichen Radioaktivität werden Neutronen auch in Teilchenschauern kosmischer Myonen im Gestein oder in der Abschirmung des Experiments erzeugt. Um auf die sehr niedrigen zu erwartenden Ereignisraten bei der Suche nach Dunkler Materie sensitiv zu sein, müssen Experimente wie das EDELWEISS-II Experiment diesen Neutronenuntergrund effizient unterdrücken. Die vorliegende Arbeit ist daher der Untersuchung des Myon-induzierten Neutronenflusses im Untergrundlabor LSM und der damit zusammenhängenden Ereignisrate in den Germaniumkristallen gewidmet. Hierfür wurden Monte Carlo Simulationen mit Hilfe des Programmpakets *Geant4* entwickelt. Um verlässliche Resultate zu erhalten, wurde zunächst die im Programmpaket implementierte Physik in Bezug auf die Neutronenproduktionsmechanismen untersucht. Die Ergebnisse innerhalb eines vereinheitlichten Versuchsaufbaus konnten anschließend mit experimentellen Messdaten sowie mit den Ergebnissen anderer Simulationspakete verglichen werden. Die spezielle Energie- und Winkelverteilung des Myonenflusses im Untergrundlabor LSM als Folge der ungleichen Gesteinsüberdeckung wurde implementiert. In einem Vergleich mit ersten Daten des EDELWEISS-II Myonendetektors konnte eine gute Übereinstimmung des simulierten Myonenflusses mit gemessenen Raten gefunden werden. Darüber hinaus wurde der von kosmischen Myonen erzeugte Untergrund an Kernrückstoßereignissen in Germanium-Kristallen simuliert. Diese Ereignisse in Koinzidenz mit einem Energieeintrag in den Plastikszintillatormodulen des Myonendetektors bestimmen die Vetoeffizienz. Die verbleibende Untergrundrate konnte auf näherungsweise $\Gamma_{\mathrm{bg}} \lesssim 10^{-5}\ \mathrm{kg}^{-1}\mathrm{d}^{-1}$ reduziert werden. Damit ist die zu erwartende Vetoeffizienz besser als $(99.94 \pm 0.01\ ^{+0.06}_{-0.1})\%$. Dies entspricht einem Unterdrückungsfaktor von $R \approx \mathcal{O}(10^3)$. Das Ergebnis der Simulationen zeigt, dass der Myon-induzierte Untergrund etwa zwei Größenordnungen besser als bisher erwartet reduziert werden kann. Dies bedeutet, dass die Sensitivität des EDELWEISS-II Experiments auf einen WIMP-Nukleonen-Wirkungsquerschnitt von bis zu $10^{-10}$pb prinzipiell nicht durch Myon-induzierten Untergrund limitiert wird.

# Abstract

In modern astroparticle physics and cosmology, the nature of Dark Matter is one of the central problems. Particle Dark Matter in form of WIMPs is favoured among many proposed candidates. The EDELWEISS direct Dark Matter search uses Germanium bolometers to detect these particles by nuclear recoils. Here, the use of two signal channels on an event-by-event basis, namely the heat and ionisation signal, enables the detectors to discriminate between electron and nuclear recoils. This technique leaves neutrons in the underground laboratory as the main background for the experiment. Besides ($\alpha$,n) reactions of natural radioactivity, neutrons are produced in electromagnetic and hadronic showers induced by cosmic ray muons in the surrounding rock and shielding material of the Germanium crystals. To reach high sensitivities, the EDELWEISS-II experiment, as well as other direct Dark Matter searches, has to efficiently suppress this neutron background.
The present work is devoted to study the muon-induced neutron flux in the underground laboratory LSM and the interaction rate within the Germanium crystals by using the Monte Carlo simulation toolkit *Geant4*. To ensure reliable results, the implemented physics in the toolkit regarding neutron production is tested in a benchmark geometry and results are compared to experimental data and other simulation codes. Also, the specific energy and angular distribution of the muon flux in the underground laboratory as a consequence of the asymmetric mountain overburden is implemented. A good agreement of the simulated muon flux is shown in a comparison to preliminary experimental data obtained with the EDELWEISS-II muon veto system. Furthermore, within a detailed geometry of the experimental setup, the muon-induced background rate of nuclear recoils in the bolometers is simulated. Coincidences of recoil events in the Germanium with an energy deposit of the muon-induced shower in the plastic scintillators of the veto system are studied to determine the veto efficiency. Finally, the remaining background rate of muon-induced bolometer hits after applying the veto condition is approximately $\Gamma_{\mathrm{bg}} \lesssim 10^{-5}\mathrm{kg}^{-1}\mathrm{d}^{-1}$. The muon detection efficiency in the simulations of the EDELWEISS-II veto system corresponds to $(99.94 \pm 0.01\ ^{+0.06}_{-0.1})\%$. This translates to a potential reduction of the muon-induced background in the order of $R \approx \mathcal{O}(10^3)$. As a result of this work, the sensitivity of the EDELWEISS-II experiment is in principle not limited by muon-induced background down to a WIMP-nucleon cross section in the range of $10^{-10}$pb.

# Contents


**1 Cosmology and Dark Matter** **1**
- 1.1 Cosmological Standard Model . . . 1
- 1.2 Cosmological observations . . . 3
  - 1.2.1 Hubble's expansion . . . 3
  - 1.2.2 Cosmic Microwave Background Radiation (CMB) . . . 4
  - 1.2.3 Rotation Curves of Spiral Galaxies . . . 8
  - 1.2.4 Large Scale Structure Formation . . . 10
  - 1.2.5 Big-Bang Nucleosynthesis . . . 11
- 1.3 Dark Matter candidates . . . 14
  - 1.3.1 Baryonic candidates . . . 14
  - 1.3.2 Non-Baryonic candidates . . . 15
- 1.4 WIMP detection methods . . . 21
  - 1.4.1 Indirect detection . . . 21
  - 1.4.2 Direct Detection . . . 22
  - 1.4.3 WIMP Detector Technologies . . . 24

**2 The EDELWEISS Experiment** **31**
- 2.1 EDELWEISS-I . . . 31
  - 2.1.1 Detection principle and calibration . . . 31
  - 2.1.2 Final results of EDELWEISS-I . . . 37
- 2.2 EDELWEISS-II . . . 40
  - 2.2.1 The new shielding concept . . . 41
  - 2.2.2 Muon veto system . . . 42
  - 2.2.3 Detector Improvements . . . 44
  - 2.2.4 Sensitivity goal . . . 46

**3 Geant4 simulations of muons interacting with matter** **47**
- 3.1 The simulation toolkit *Geant4* . . . 47
- 3.2 The *Geant4* - physics list . . . 49
  - 3.2.1 Electromagnetic interactions . . . 49
  - 3.2.2 Muon nuclear interaction . . . 51
  - 3.2.3 Hadronic interactions . . . 53
  - 3.2.4 *Geant4* particle production cuts . . . 55
- 3.3 Neutron yield for varying muon energies . . . 56
  - 3.3.1 Neutron yield by individual physics processes . . . 59
- 3.4 Neutron yield in various materials . . . 60
- 3.5 Kinetic energy spectrum of $\mu$-induced neutrons . . . 63

3.6 Angular distribution of $\mu$-induced neutrons . . . . . 64

**4 The muon flux at the LSM** **67**
4.1 The muon flux underground . . . . . 67
4.2 Muon distribution in the LSM underground laboratory . . . . . 72
4.3 First measurements with the EDELWEISS-II muon veto system . . . 76

**5 EDELWEISS-II simulations with Geant4** **77**
5.1 The EDELWEISS-II muon veto system . . . . . 77
5.1.1 Mean muon energy deposit per module . . . . . 78
5.1.2 Geometrical efficiency of the muon veto system . . . . . 81
5.2 The EDELWEISS-II simulation setup . . . . . 83
5.2.1 LSM experimental hall and muon generator . . . . . 83
5.2.2 The EDELWEISS-II detectors and shielding . . . . . 86
5.3 *Geant4* simulation results . . . . . 88
5.3.1 Geometrical muon rates . . . . . 89
5.3.2 Total energy deposit per module . . . . . 90

**6 Muon veto efficiency for coincident bolometer events** **93**
6.1 Muon-induced background in the EDELWEISS-II bolometers . . . . . 93
6.1.1 Muon energy considerations for the simulations . . . . . 94
6.1.2 Muon-induced bolometer events . . . . . 96
6.1.3 Nuclear recoils by muon-induced neutrons . . . . . 99
6.2 Muon veto and bolometer coincidences . . . . . 102
6.2.1 Remaining background rate . . . . . 102
6.2.2 Remaining background events . . . . . 104
6.2.3 Veto energy threshold dependence . . . . . 106
6.3 Conclusions . . . . . 107

**7 Conclusions and Outlook** **109**

**A Muon flux underground** **113**

**B Geant4 materials** **117**

**Bibliography** **119**

# 1 Cosmology and Dark Matter

The basis of modern cosmology is Einstein's General Theory of Relativity and Quantum Field Theory. By additional assumptions one can solve Einstein's equations and find a description of the universe and the manner in which it evolves. Already Einstein himself assumed that on average the universe looks the same from every vantage point ($\rightarrow$ *homogeneity*), as well as it looks the same in every direction ($\rightarrow$ *isotropy*). To Einstein's initial surprise, the solutions found described an either expanding or contracting universe. At that time, this was in contrast to the common belief among scientists of an infinitely expanded and static cosmos. In fact, as experimental observations by Vesto Slipher or Edwin Hubble indicated, the universe was not static, but expanding. This lead to the current famous cosmological *Big Bang Model* in which the universe, starting from a tremendously hot and dense initial state, has been expanding for over thirteen billion years. In the following years the controversially discussed Big Bang theory developed both from further experimental observations of the structure of the universe as from theoretical considerations done for example by Alexander Friedmann or Georges Lemaître. Since the discovery of the Cosmic Microwave Background radiation by Arno Penzias and Robert Wilson though, the Big Bang model is nowadays widely accepted as the best theory of the origin and evolution of the cosmos and evolved to the Cosmological Standard Model discussed in this chapter.

## 1.1 Cosmological Standard Model

The Cosmological Standard Model is based on the assumption that the universe is homogeneous (translational invariance) and isotropic (rotational invariance) on sufficient large spatial scales. This *Cosmological Principle* is verified by the observation that the mass distribution, e.g. the distribution of galaxies in the universe on large scales above $100 Mpc$ is rather homogeneous and isotropic. The further assumption that the spatial component of the metric describing the universe can be time dependent leads to the *Friedmann-Lemaître-Robertson-Walker* (or Robertson-Walker) metric:

$$ds^2 = dt^2 - a^2(t)\left(\frac{dr^2}{1-kr^2} + r^2 d\theta^2 + r^2 sin^2(\theta) d\phi^2\right) \tag{1.1}$$

where $a(t)$ is the time-dependent scale parameter describing the expansion or contraction of the universe. The energy content of the universe is directly connected to the curvature parameter $k$, which can have three possible values for an open, infinite universe with hyperbolic curvature ($k = -1$), a flat, infinite universe with no curvature ($k = 0$) or a closed and finite universe with spherical curvature ($k = +1$).

Within the Robertson-Walker metric, Einstein's equations of general relativity simplify to the so-called *Einstein-Friedmann-equations*. They describe the time evolution of the cosmic scale factor $R(t)$ dependent on the density $\rho(t)$ and the pressure $p(t)$ of the cosmic substrate, as well as on the cosmological constant $\Lambda$:

$$\left(\frac{\dot{R}(t)}{R(t)}\right)^2 = H(t)^2 = \frac{8\pi G}{3} \cdot \rho(t) - \frac{k}{R^2(t)} + \frac{\Lambda}{3} \tag{1.2}$$

$$\frac{\ddot{R}(t)}{R(t)} = -\frac{4\pi G}{3}\left(\rho(t) + 3p(t)\right) + \frac{\Lambda}{3} \tag{1.3}$$

where $k$ is the curvature parameter, $G$ is the gravitational constant and $H(t)$ is the time dependent *Hubble* parameter. The density and the pressure can be divided into two components: $\rho_m$ or $p_m$ for matter and $\rho_r$ and $p_r$ for radiation, respectively. One can define a critical density $\rho_{c,0}$ at the present epoch $t = t_0$ as:

$$\rho_{c,0} = \frac{3H_0^2}{8\pi G} \tag{1.4}$$

This term was originally used as a means to determine the geometry of the universe where $\rho_c$ is the critical density for which the universe is flat (assuming a vanishing cosmological constant). Since this value depends only on constants, it is itself a universal constant, except for the not yet certain, accurate value for the Hubble constant $H_0$. By introducing the dimensionless Hubble scaling factor:

$$h_0 = \frac{H_0}{100\ km\ s^{-1}Mpc^{-1}} \tag{1.5}$$

the present value is:

$$\rho_{c,0} = h_0^2 \cdot 18.8 \cdot 10^{-30} g\ cm^{-3} \tag{1.6}$$

By introducing the total density parameter:

$$\Omega = \frac{\rho}{\rho_c} \tag{1.7}$$

and the equivalent density parameter for the cosmological constant:

$$\Omega_\Lambda = \frac{\Lambda}{3H_0^2} \tag{1.8}$$

one can rewrite equation 1.2 to:

$$1 + \frac{k}{R^2 H_0^2} = \Omega_M + \Omega_\Lambda \tag{1.9}$$

Like this, the present total energy density $\Omega = \Omega_M + \Omega_\Lambda$ of the universe is directly linked with its curvature.
The equations (1.2) and (1.3), together with the values of $\Omega_M$ and $\Omega_\Lambda$ determine the history and the fate of the universe. Observations in the last decade securely

indicate that the universe is best described by models with a cosmological constant $\Lambda \approx 0.75\ \Omega_{\text{crit}}$. These models are called *Friedmann-Lemaître models* or Friedmann-Lemaître-Robertson-Walker models named by the four scientists developing the underlying metric. The non-vanishing term $\Omega_\Lambda$ can be attributed within the framework of quantum field theory to the energy density of the vaccuum and is often called *Dark Energy*. The associated negative pressure of the quantum vacuum causes in general relativity a gravitational repulsion. In consequence, for models with a positive $\Lambda$ the before slowed down expansion can become an accelerated expansion in a later phase of the universe. The ultimate fate of all models with $\Lambda \neq 0$ are determined by the present values of $H_0$, $\Omega_{M,0}$ and $\Omega_{\Lambda,0}$. Hence great observational effort is made to determine these values as precisely as possible. The major astrophysical observations supporting the Standard Cosmological Model together with observational evidence for Dark Matter and Dark Energy will be discussed in the next chapter.

## 1.2 Cosmological observations

In the last decade in almost every cosmologically relevant field, outstanding improvements were made to further control the parameters of the Cosmological Standard Model. The preponderance of evidence, based on measurements of for example the Hubble constant, the abundance of light elements in the universe, the distributions of galaxies on large scales and first and foremost precise measurements of the Cosmic Microwave Background favors a universe that will not collapse. Moreover, models with a non-vanishing cosmological constant $\Lambda$ and an actual accelerating universe are strongly favored. In this section experimental observations are shown and their historical relevance together with present-day constraints to the standard model of cosmology and the Dark Matter contribution are discussed.

### 1.2.1 Hubble's expansion

In the early years of the nineteenth century, cosmologists generally believed in a static and infinitely expanded universe. However, observations done by Vesto Slipher already in 1912 pointed at a non-static but rather dynamic cosmos. He was the first to observe the redshift of spectral lines from the nearby Andromeda nebulae [Sli13], and soon discovered that almost all such nebulae, respectively spiral galaxies, recede from Earth [Sli15]. But not until a decade later, the astronomer Edwin Powell Hubble (1889-1953) made the famous discovery of a linear relation between distances and the redshift of galaxies nowadays known as *Hubble's law*. Observations of Cepheid variable stars in spiral galaxies enabled him to calculate the distances of these objects. Combining his measurements of the distances $D$ of various nearby galaxies with Slipher's measurements of the redshifts $z = \Delta\lambda/\lambda_0$ associated with these galaxies, Hubble established a linear relation [Hub29]:

$$cz = v = H_0 \cdot D \tag{1.10}$$

with the approximation of a Doppler-shift $z = v/c$ for $v \ll c$ and introducing the proportionality factor $H_0$, the *Hubble-constant*. Historically, this led to the view of

an expanding universe, taking into account Einstein's theory of General Relativity. This was independently derived theoretically by Alexander Friedmann [Fri22] and later by Georges Lemaître [Lem31]. Hereby the velocity of distant galaxies (peculiar velocities are negligible) can be interpreted as an expression of the expanding space in a homogeneous and isotropic universe. The expansion of space in Einstein's equations is expressed with the time-dependent scale factor $R(t)$ and hence the redshift $z$:

$$1 + cz = \frac{R_0}{R(t_E)} \tag{1.11}$$

where $R_0 = R(t_0)$ is the present value of the scale factor and $R(t_E)$ the scale factor at the time $t_E$ of the radiation emission of the distant galaxy, which can be observed today with the redshift $z$. In first order expansion $R(t) = R_0 + (t - t_0)\dot{R}_0$ one finds together with (1.10) and (1.11):

$$cz = \frac{R_0}{R_0 - \Delta t \dot{R}_0} - 1 \simeq c\Delta t \frac{\dot{R}_0}{R_0} = D\frac{\dot{R}_0}{R_0} = DH_0 \tag{1.12}$$

Hence one can see that the Hubble-constant or more generally the expansion rate of space is not a constant but a function of time:

$$H(t) = \frac{\dot{R}(t)}{R(t)} \tag{1.13}$$

with the present value $H_0 \equiv H(t_0) = \dot{R}_0/R_0$.

The Hubble-constant determines the size of the observable universe. Measuring such a fundamental quantity has been of great interest among astronomers over the last century. Hubble obtained a very high value for $H_0 = 500\ km\ s^{-1}Mpc^{-1}$, due to errors in his distance calibrations. Nowadays, still facing tremendous difficulties in determining distances on cosmic scales, results vary for the value of $H_0$ between:

$$50 < H_0 < 100\ km\ s^{-1}Mpc^{-1} \tag{1.14}$$

with the best fit value by the Particle Data Group [Yao06] combining ΛCDM models and WMAP three year data [Spe07] to:

$$H_0 = 73^{+3}_{-4}\ km\ s^{-1}Mpc^{-1} \tag{1.15}$$

where $1Mpc = 3.086 \cdot 10^{19}\ km$. Sometimes, the Hubble constant is expressed in a dimensionless form $h_0$, see equation (1.5).

### 1.2.2 Cosmic Microwave Background Radiation (CMB)

If the universe evolved from an early stage with extremely high density according to the Big Bang model, one expects in the early phase (before galaxy or star formation) a hot, dense plasma, where radiation and ionised matter were in equilibrium. After

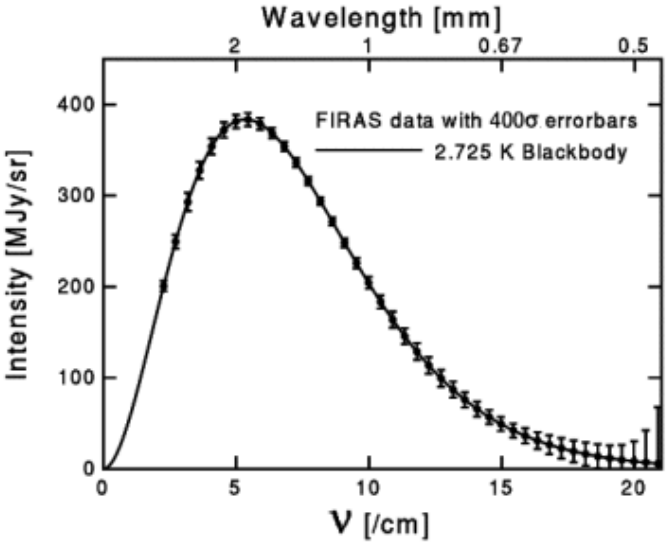


**Figure 1.1:** CMB spectrum plotted in wavenumber or waves per centimeter vs. intensity. The solid curve shows the expected intensity from a single temperature blackbody spectrum ($T = 2.725\ K$). The error bars have been multiplied by 400 for visualisation [Mat94].

the plasma cooled down due to expansion to $\sim 10^5\ K$, protons and electrons formed neutral hydrogen atoms and the radiation decoupled.

Already in 1948 George Gamov, Ralph Alpher and Robert Herman [Gam46; Gam48] expected as remainder of that primordial plasma a *Planck black-body* radiation with a corresponding temperature in the order of $T \sim 3 - 10\ K$. Only in 1964 A.A. Penzias and R.W. Wilson discovered an excess radio background at $\lambda = 7.35\ cm$ corresponding to a temperature of 2.5 to 4.5 $K$ [Pen65]. In the following years, up to the satellite experiment *Cosmic Background Explorer* (COBE) starting in the year 1989 [Smo92], the spectrum of the radiation was measured up to the *mm*-range and the agreement with a theoretical Planck spectrum at a temperature of $2.725 \pm 0.002\ K$ is impressive as can be seen in figure 1.1.

The data were taken at 34 positions equally spaced along this curve and match the curve so exactly, with error uncertainties less than the width of the blackbody curve, that it is impossible to distinguish the data from the theoretical curve. For visualisation, the error bars are multiplied by 400 in figure 1.1. The results show the most precise blackbody spectrum ever measured and illustrate the predictions of the Big Bang theory to an extraordinary degree. See [Mat94; Fix96] for more details.

The detection of the CMB and its precise black-body nature are the most spectacular evidence for the Big Bang theory after the discovery of the expansion of the universe by Hubble. Although the isotropic nature of the CMB clearly supports a homogeneous universe in the early stage, it poses questions about the present epoch of the universe. Obviously, the average temperature and density of galaxies differ

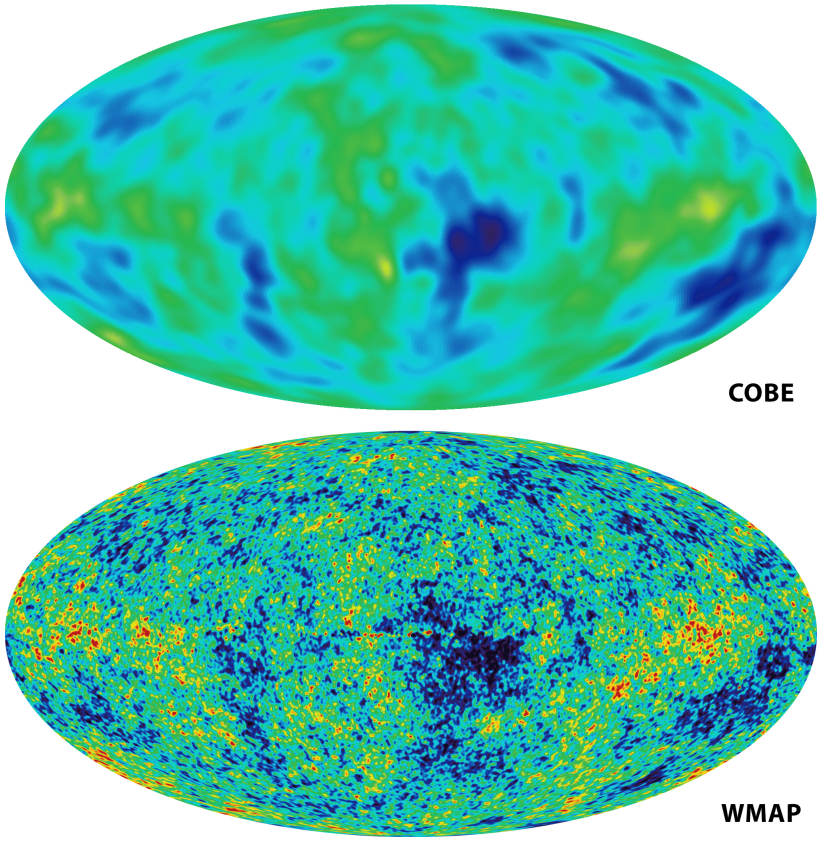


**Figure 1.2:** Full sky maps of the CMB anisotropies computed by data measured with the COBE (upper) and WMAP (lower) experiment corrected by the foreground of the galactic plane and effects by the local motion [Smo92; Spe03].

dramatically from that of the space between them. In the Big Bang model, small perturbations of density in the otherwise homogeneous matter distribution of the early universe will, due to gravitational attraction, grow and eventually form the stars and galaxies known to exist today [Ber06a]. These initial density fluctuations at the time the radiation decoupled ($z \approx 1000$) leave an imprint on the distribution of the CMB photons. Nowadays, density fluctuations $\delta$ on scales of galaxies are certainly $\delta \gg 1$ and $\delta \approx 1$ on scales of galaxy clusters or super clusters. To make large scale structures possible today, the density fluctuations at $z \approx 1000$ must be of order $\delta \sim 10^{-3}$ and fluctuations of the CMB are expected to be of the same order ($\Delta T/T \sim 10^{-3}$). The observation of tiny angular anisotropies of the CMB was first achieved by the COBE DMR (Differential Microwave Radiometers) 1992 [Smo92] and with much higher accuracy by the *Wilkinson Microwave Anisotropy Probe* (WMAP) 2003 [Spe03]. The full sky maps of minute temperature variations, determined by the two experiments respectively, are shown in figure 1.2. The relevant physical processes leading to these anisotropies are described in more details in [Sco95].

| parameter | value |
|---|---|
| $\Omega_M$ | $0.268 \pm 0.0180$ |
| $\Omega_\Lambda$ | $0.732 \pm 0.018$ |
| $\Omega_b$ | $0.044 \pm 0.0014$ |
| Hubble constant $H_0$ | $70.4^{+1.5}_{-1.6}\ km\ s^{-1}\ Mpc^{-1}$ |
| Age of Universe $t_0$ | $13.73^{+0.16}_{-0.15}\ Gyr$ |

**Table 1.1:** The cosmological parameters as estimated by the three year data set from the WMAP experiment [Spe07]

The temperature fluctuations measured by the two experiments are however on a level of $\Delta T/T \sim 10^{-5}$. Following the discussion above, the corresponding density fluctuations at the time the radiation decoupled could not have evolved to the observed structures today yielding to the presence of Dark Matter. Since the photons interact only with baryonic matter, the density fluctuations of the CMB only reflect the distribution of baryonic matter. The Dark Matter distribution at the time of decoupling, could have in contrast higher density fluctuations yielding to gravitational potentials for the baryonic matter. The non-existence of temperature fluctuations in the CMB in the order of $\Delta T/T \sim 10^{-3}$ hence is one of the most convincing arguments for the existence of Dark Matter in the universe.

The CMB anisotropies in principle depend on all parameters relevant for the cosmological model, e.g. $\Omega_0$, $\Omega_b$, $\Omega_\Lambda$, $\Omega_\nu$ and $H_0$. Consequently, a multitude of information can be obtained by the observation of the CMB. While studying the temperature fluctuations in more detail, it is convenient to use the spherical decomposition, since any function on the unit sphere can be expanded in spherical harmonics, thus in particular the measured temperature fluctuation. By comparing the measured expansion coefficients with theoretical ones obtained by varying all cosmic parameters one can achieve very good accuracy on many parameters. This has been done to a considerable extent by the satellite experiment WMAP analysing three years of data [Spe07]. The shape of the obtained power spectrum contains several 'acoustic peaks', due to oscillations of the cosmic fluid in the early universe [Sak65], and is shown in figure 1.3. The location of these peaks, as well as their relative heights, are very sensitive to the total energy density $\Omega_{\text{tot}} = \Omega_M + \Omega_\Lambda$. The results from WMAP corresponds with excellent accuracy to a flat universe with $\Omega_{\text{tot}} = 1.0 \pm 0.1$. Together with results from other observations and experiments, e.g. supernova luminosity/distance relationship, a 'concordance model' has emerged during the last few years. This model favours the existence of a cosmological constant $\Lambda$ and has a significant amount of (cold) Dark Matter with $\Omega_M \sim 0.3$ and $\Omega_\Lambda \sim 0.7$ and is therefore also denoted $\Lambda$CDM model. The best fit model parameters to the WMAP data are summarised in table 1.1.

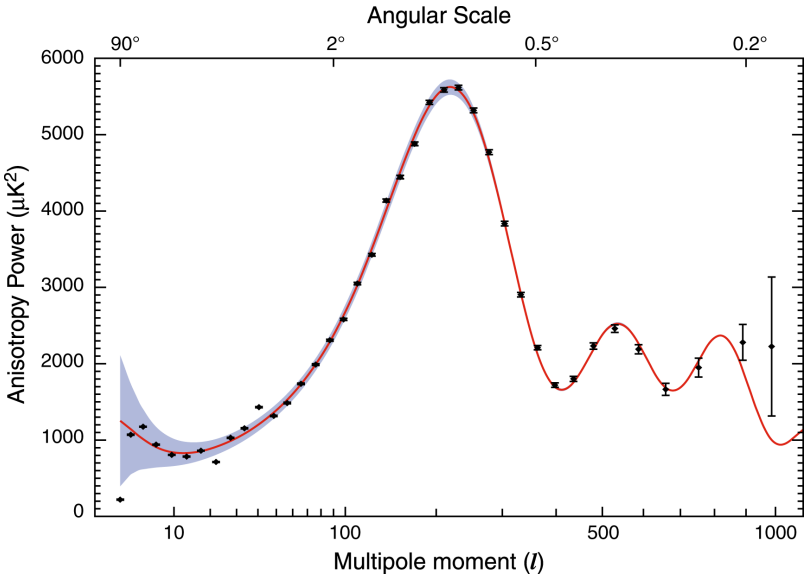


**Figure 1.3:** The data on the CBR measured by the WMAP experiment, together with the best fit ΛCDM model, with parameters given according to table 1.1 [Spe07].

### 1.2.3 Rotation Curves of Spiral Galaxies

Already in the year 1933 Fritz Zwicky [Zwi33] postulated the existence of Dark Matter in the universe while studying the velocity distribution of galaxy clusters. He concluded that the clusters contain far more dark matter than luminous matter by translating the luminosity of the galaxies into a corresponding mass. The gravitational force of these masses derived by the measured velocity dispersion of these galaxies with the help of the *virial theorem* then was not sufficient to keep the galaxy clusters bound together. Therefore the mass density associated with the luminous matter cannot account for the observed dynamics [Raf97]. Further observations since then made on galactic scale, i.e. stars, hydrogen clouds, x-ray gas in clusters, etc. strongly support the theory of Dark Matter. The probably most direct and impressive observation of these will be discussed in more detail in the following section.

Spiral galaxies, like our own galaxy, the Milky Way, and the nearby Andromeda galaxy M31, consist of a central bulge and a thin disk. This disk with a spiral structure is stabilised against collapse by angular momentum conservation. By measuring the orbital velocities of the disk with the redshift of spectral lines, one can obtain rotation curves, i.e. the orbital velocity as a function of radius from the centre. Since the luminosity of the disk falls off exponentially with radius one would expect that most of the galactic mass is concentrated within a few scale-lengths of the bulge. The orbital velocity outside the central mass would then be a function of the radius according to Kepler's third law:

$$v_{rot}(r) = \sqrt{\frac{G_N M}{r}} \tag{1.16}$$

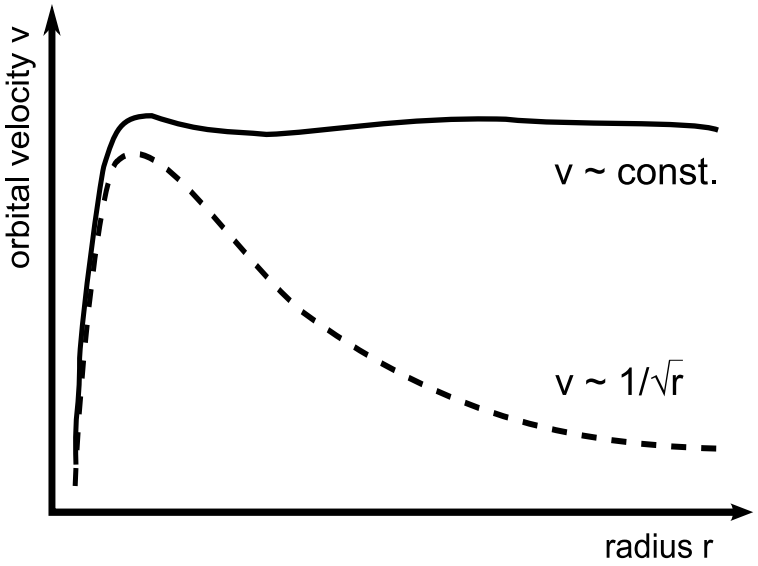


**Figure 1.4:** Schematic rotation curve as a function of radius from the centre of a typical spiral galaxy. The dashed line represents the predicted curve according to Kepler's law ($v \propto 1/\sqrt{r}$) and the solid line represents observations ($v \sim const$).

where $G_N$ is Newton's constant and $M$ is the central mass of the galaxy. The velocity would then behave in analogy to the Keplarian law $v_{rot} \propto r^{-1/2}$ as illustrated in figure 1.4. M. Persic and P. Salucci [Per96] as well as V.C. Rubin et.al. [Rub80; Rub85] have collected in total the rotation curves of around 1000 spiral galaxies by systematic optical studies.

More convincing evidence for the unexpected galactic rotation curves arises from radio observations. In the disks of spiral galaxies neutral hydrogen can be observed by its 21 $cm$ line emission. Since purely optical observations of tracers typically stop at $2-4$ scale-lengths, hydrogen can be observed to much larger galactic radii. Line ratios of two $CO$ transitions are also very sensitive density tracers extending to large radii. As shown in figure 1.5, a study of a broad sample of galactic rotation curves show in almost all investigated galaxies that the orbital velocity remains constant ($v(r) \sim constant$) after a rise near the galactic centre.

The difference of the observed rotation curves to the ones expected by the luminous material is ascribed to the gravitational effect of Dark Matter. A constant orbital velocity can be obtained by introducing an additional spherically symmetric 'halo' component, so that the total mass is $M(r) \propto r$ and the density is $\rho(r) \propto r^{-2}$. This dark matter halo is furthermore supported by additional observations, e.g. vertical velocity dispersions that support the fact, that the dark matter cannot be contained alone in the disk, as well as material orbiting perpendicularly to the normal disk, which concludes to an almost spherical gravitational potential [Raf97].

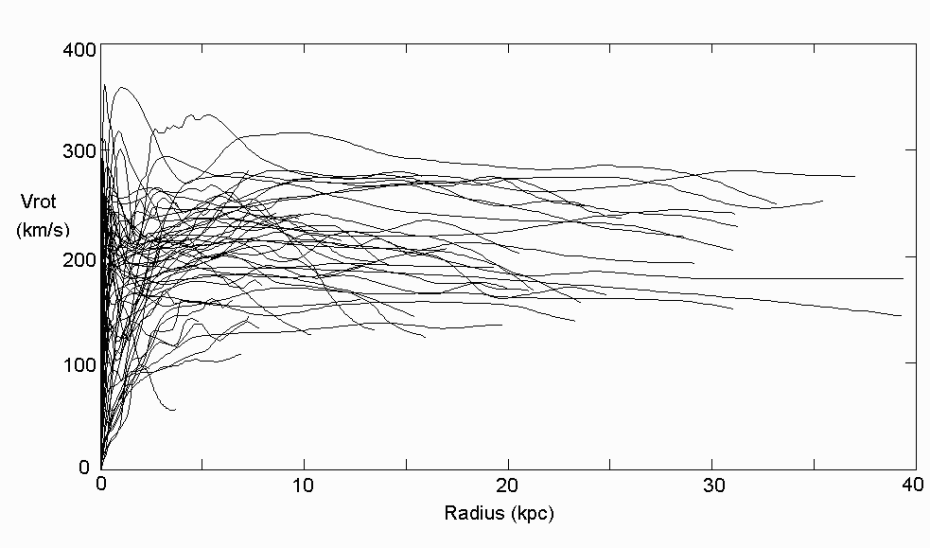


**Figure 1.5:** Rotation curves for a multitude of spiral galaxies obtained by optical, H I, H$\alpha$ and CO line spectroscopy. The rotation curves generally show a steep nuclear rise and high-velocity central rotation, followed by a broad maximum in the disk and then a flat rotation due to the massive Dark Matter halo. For details see [Suf99] and references therein.

### 1.2.4 Large Scale Structure Formation

Very rigorous constraints on the cosmological model as well as on the Dark Matter distribution arise from arguments of cosmic structure formation. As mentioned in the previous section, the precise black-body nature of the Cosmic Microwave Background radiation (CMB) supports the theory of an almost perfectly homogeneous early universe with tiny modulation of its density field, yielding to the small anisotropies of the CMB. These density contrasts are enhanced by gravitation force with time, leading eventually to the formation of galaxies or clusters if the self-gravity of an overdense region becomes large enough to decouple from the overall Hubble expansion.
Currently, the *Sloan Digital Sky Survey* (SDSS) is systematically mapping a quarter of the entire sky and determining the position and absolute brightness of more than 100 million celestial objects [Yor00]. Using this galaxy survey measuring the geometry of the universe through the distance-redshift relation, one could extract oscillatory features in the matter power spectrum as predicted in the baryon acoustic oscillations [Pee93]. The latest results [Per07], combining the obtained matter distribution with the WMAP data of the CMB, also lead to a ΛCDM scenario with a best-fit value of

$$\Omega_M = 0.256^{+0.029}_{-0.024} \quad (68\% \text{ C.L.}) \tag{1.17}$$

This value does not include any information from the overall shape of the power

spectra and hence is an extremely clean cosmological measurement expected to be independent of systematics.

Among cosmologists there is much work done which attempts to model the observed large-scale structure of the universe, e.g. SDSS, by numerical computer simulations. Particularly *N-body*-simulations are done based on the Big Bang model. Starting with assumptions about the type of matter that makes up the universe and initial density perturbations, it is possible to simulate the evolution of the distribution of matter in time. The results can then be compared with the observations to support or refute cosmological models and hence constrain the model parameters. Within the simulations one can distinguish mainly two different scenarios describing the matter properties. On the one hand, one speaks of **Hot Dark Matter** (HDM), if the particle masses are very low ($m \leq 100\ eV$), so they stay relativistic for a long time. Due to their relativistic behaviour, primordial density fluctuations of galactic sizes or smaller are damped by free streaming of these particles. Hence large scale structures form first and later fragment into smaller ones, e.g. galaxies. Neutrinos with non-zero rest mass, a HDM candidate within the standard model of particle physics, could in principle contribute significantly to the matter content of the universe. However, neutrino streaming results in very low density contrast on galactic scales, thus making galaxy formation nearly impossible [Dav81]. The neutrino as a Dark Matter candidate will also be discussed in section 1.3.2. On the other hand, one speaks of **Cold Dark Matter** (CDM), if the matter would consist of very massive particles. Unlike baryons that are frozen to the radiation field prior to recombination, these heavy particles could decouple from the cosmic fluid much earlier and be free to cluster as soon as they become non-relativistic. Thus initial density fluctuations show no damping by free streaming at physically relevant scales. In this picture the smallest structures, e.g. of sub-galactic size, form first driven by the CDM.
The outcome of these numerical simulations to study large scale structure formation also strongly support models with a cosmological constant $\Lambda \neq 0$ and a large fraction of non-baryonic Cold Dark Matter [Blu84]. Hot Dark Matter does not provide a good fit with observations, since essentially all small-scale structures corresponding to supercluster scale or below are wiped out. For more details about Hot and Cold Dark Matter and the according major particle candidates, see. chapter 1.3.

### 1.2.5 Big-Bang Nucleosynthesis

Many astrophysical constraints on the cosmological model and the fraction of Dark Matter contributing to the total energy density of the universe can be made, as discussed in the previous sections. The natural question arises, if the Dark Matter can be composed of normal baryonic matter in some non-luminous form, e.g. stellar remnants as black holes or molecular hydrogen clouds. However, the overall baryonic content of the universe is strongly constrained by Big Bang Nucleosynthesis (BBN), which treats the number densities of various nuclei the first few seconds up to minutes after the Big Bang when the light elements were synthesised. About one second after

the Big Bang, when the universe cooled down sufficiently to form stable protons and neutrons, the relative abundances of these particles can be calculated using simple thermodynamical arguments. Taking into account the expansion of space, one can calculate the fraction of protons and neutrons based on the temperature at that time. Below a temperature of about 1 $MeV$, the reaction rate between neutrons and protons 'freeze out[1]' and subsequently all the remaining neutrons together with the ambient protons form $^4He$ and traces of deuterium ($D$), $^3He$ and $^7Li$. Shortly thereafter, at three minutes after the Big Bang, the universe becomes too cool for any nuclear fusion to occur. At this point, the elemental abundances are fixed, and only change as some of the radioactive products of BBN (such as tritium) decay. It can be shown within the standard Big Bang model, that the nuclear processes mainly lead to $^4He$, with a primordial mass fraction of about 24%. The other light elements are produced in lesser amounts, e.g. about $10^{-5}$ of $D$ and $^3He$ and about $10^{-10}$ of $^7Li$ by number relative to $H$ [Yao06]. The predicted abundances of the light elements depend almost solely on one unknown cosmological parameter, the baryon number fraction relative to the present day number density of cosmic microwave background photons, $\eta_{10} \equiv 10^{10}\eta = 10^{10} n_B/n_\gamma$. Within the standard model of BBN, this ratio can be directly related to the total mass fraction of baryons $\Omega_b$. The number density of microwave background photons $n_\gamma$ is fixed by the present CMB black body temperature $T = T_0 = 2.725\ K$ [Yao06]:

$$n_\gamma = \frac{2\ \zeta(3)}{\pi^2}\ T^3 \sim 410\ cm^{-3} \tag{1.18}$$

where $\zeta(x)$ are Riemann's zeta functions. Together with the critical density $\rho_{crit}$ (see equation 1.4), the baryon contribution to the density of the universe is:

$$\Omega_b h^2 = 3.66 \times 10^7\ \eta \tag{1.19}$$

where $h$ is the dimensionless Hubble parameter. Accordingly the main source of uncertainties comes from the nuclear reaction rates. Numerical calculations of the abundance of the light elements versus the baryon to photon ratio $\eta$ compared with astrophysical observations, as well as the latest constraints from the WMAP misssion, are shown in figure 1.6.

Between Big Bang nucleosynthesis theory and experimental observations a rather conservative range for the ratio $\eta$ can be determined [Yao06]:

$$4.7\ \times 10^{-10}\ <\ \eta\ <\ 6.5\ \times 10^{-10} \quad (95\%\ \text{C.L.}) \tag{1.20}$$

This corresponds to the baryon content of the universe of:

$$0.017\ \leq\ \Omega_b h^2\ \leq\ 0.024 \quad (95\%\ \text{C.L.}) \tag{1.21}$$

[1]The general criterion for freeze-out to occur is that the annihilation, transformation or decay rate (per particle) of the particle species, which maintains equilibrium with other particle species, falls below the expansion rate of the universe: $\Gamma < H$.

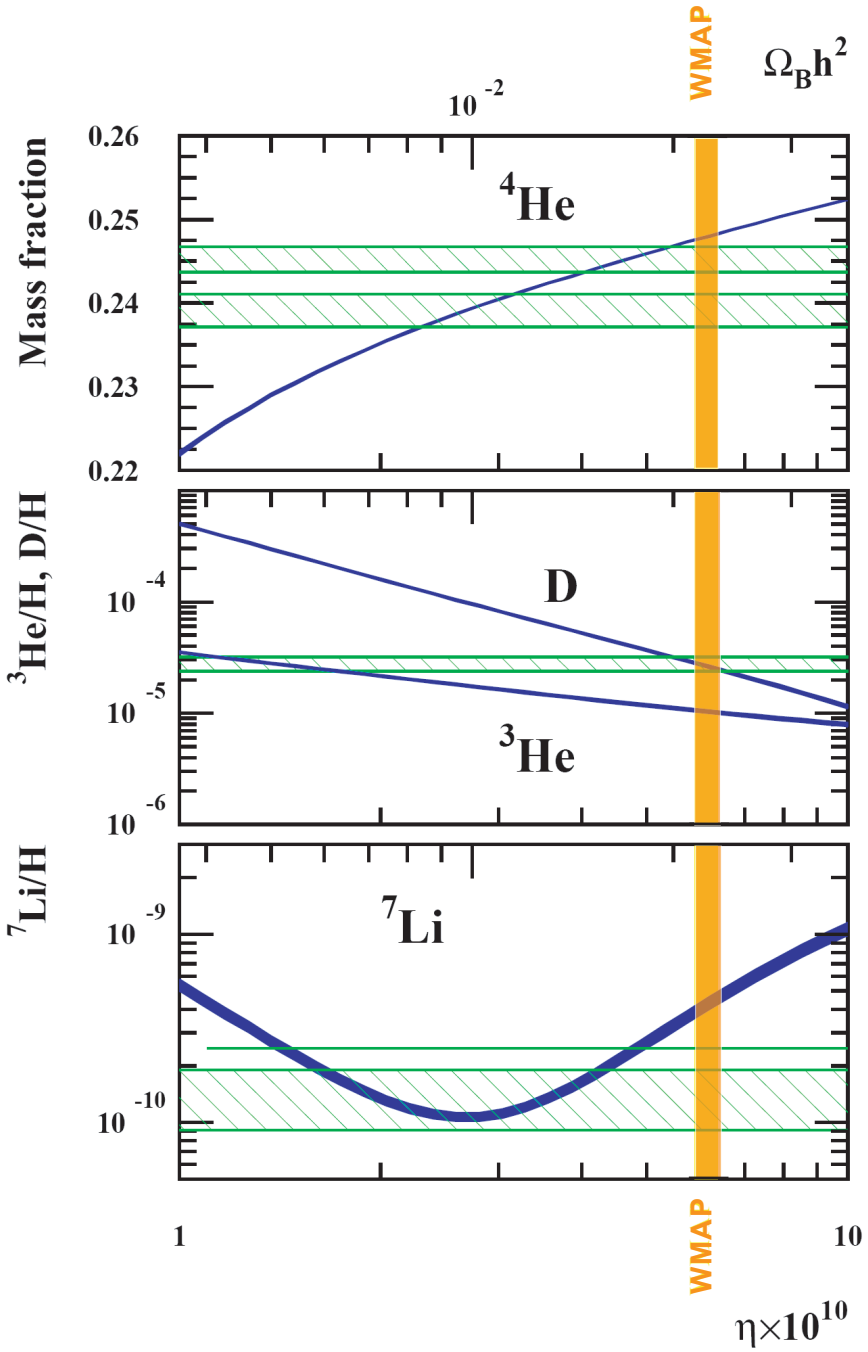


**Figure 1.6:** Abundances of $^4He$ (mass fraction), $D$, $^3He$ and $^7Li$ (by number relative to $H$) as a function of the baryon over photon ratio $\eta$ or $\Omega_b h^2$. The blue lines are obtained from Monte Carlo calculations and respective theoretical uncertainties. Horizontal hatched areas represent primordial $^4He$, $D$ and $^7Li$ abundances deduced from observational data (see [Coc04] and references therein). The vertical stripe represents the (68% C.L.) $\Omega_b h^2$ limit provided by WMAP [Spe03].

The result from the WMAP mission [Spe03; Spe07], deducing the baryon fraction by studying the CMB lie well between these limits:

$$\Omega_b h^2(\text{WMAP}) = 0.02229 \pm 0.00073$$

This result of Big Bang nucleosynthesis not only strongly supports the Big Bang cosmology, but plays also a key role in understanding the matter budget of our universe. The allowed contribution of baryons to the total energy density of the universe $\Omega_b$ (in fact, $\Omega_b h^2$) is experimentally fixed by the cosmic microwave background, since the CMB dominates the number density of photons in the universe. Even by accepting the complete range $0.017 \leq \Omega_b h^2 \leq 0.024$ for the baryonic matter density, one has to conclude that baryonic matter cannot account for the estimates of the cosmological density ($\Omega_{\text{tot}} \sim 1$, or rather $\Omega_M \sim 0.3$). This gives another powerful indication that most of the matter density in the universe must be some kind of non-baryonic Dark Matter.

## 1.3 Dark Matter candidates

All the observational success related to the Cosmic Microwave Background radiation (CMB) and its anisotropies together with the theory of baryo-nucleosynthesis (BBN), as described in the previous section, set stringent limits on the cosmological model and its parameters. The density of matter in the universe in the form of baryons $\Omega_b$ hence can not account for the necessary total matter contribution ($\Omega_M \sim 0.3$). Further on, there is astronomical evidence indicating that there is far more matter needed to maintain Kepler's laws in galaxy dynamics, than can be associated with the luminous parts of the galaxies (see also section 1.2.3). A large number of candidates for this unknown Dark Matter has been proposed by astronomers as well as particle physicists with masses ranging from $10^{-5}\ eV = 9 \times 10^{-72} M_\odot$ (axions) to $10^4 M_\odot$ (black holes). Several possible candidates and their compatibility with the standard cosmological model will be discussed in this section.

### 1.3.1 Baryonic candidates

Even though the theory of Big Bang nucleosynthesis clearly excludes baryonic particles to represent a large fraction of the matter density in the universe a short summary of baryonic candidates will be given. The most popular baryonic candidates are the Massive Astrophysical Compact Halo Objects (MACHOs). A MACHO is made of normal baryonic matter, which emits little or no radiation and drifts through interstellar space unassociated with any solar system. These objects include, for example, brown dwarfs, black holes and neutron stars. But also white dwarfs and very faint red dwarfs have been proposed as candidate MACHOs. The technique of gravitational microlensing is used to search for these kinds of objects. Hereby no distortion in shape of the observed object according to Einstein's General Relativity can be seen, but a change in time of the amount of light received from a background object. If the Dark Matter halo of the Milky Way contains MACHOs,

one will occasionally pass close to the line of sight between the observer and a distant star, e.g. in the Magellanic Clouds. The principle of microlensing events to determine the amount of Dark Matter contained in MACHOs is described in more detail by Paczynski [Pac86]. Various experiments try to detect microlensing events by monitoring millions of stars towards the Large and Small Magellanic Clouds (LMC and SMC), e.g. the MACHO [Alc00] and the EROS [Afo03] experiments. Both experiments do have several candidate events towards these two targets and therefore are able to set upper limits for the population of lenses in the Milky Way. The MACHO collaboration, after almost six years of observation towards the Large Magellanic Cloud, gives a maximum MACHO halo fraction of $\sim 20\%$ for a typical halo model with a 95% confidence interval. Interpreted as a galactic halo population, the most probable MACHO mass is between 0.15 and 0.9 $M_\odot$. A halo totally made of compact objects is ruled out at the 95% C.L. The EROS experiment, with five years of data towards the Small Magellanic Cloud, show that less than $\sim 25\%$ of a standard halo can be made of objects up to 1 $M_\odot$ with a 95% C.L. Lately the EROS-2 experiment [Tis07] considerably lowered the limit set by the MACHO collaboration to $\sim 8\%$ (95% C.L.) of the halo mass and ruled out MACHOs in the mass range $0.6 \times 10^{-7} M_\odot < M < 15 M_\odot$ as the primary occupants of the Milky Way Halo. Much debate has occured about the nature of the observed lenses, but neither invisible, e.g. primordial black holes, nor faint, e.g. cool white dwarfs with hydrogen atmospheres can account to the corresponding level. Primordial black holes form before Big Bang nucleosynthesis and thus are perfect Dark Matter candidates. The current major problem is the lack of plausible creation mechanisms in the early universe for primordial black holes. On the other hand, white dwarfs, though experimentally detected, are not seen with the required density population in multicolour surveys, e.g. the SDSS experiment [Gat04].
As a summary, MACHOs are experimentally detected with gravitational microlensing, but all experimental data limits the contribution to the total halo mass to about $10 - 20\%$. The most important conclusion, however, is that a 100% all MACHO halo is ruled out at the 95% C.L. Together with the results from BBN, this strongly supports non-baryonic Dark Matter candidates described in the next section.

### 1.3.2 Non-Baryonic candidates

Having reviewed the need for non-baryonic Dark Matter candidates, the most prominent and most discussed candidates will be explored in more details in this section.

#### Light Neutrinos

Within the standard model of particle physics, only one non-baryonic Dark Matter candidate is currently known to exist: the neutrino $\nu$ with non-zero masses as required by the experimentally well established phenomenon of neutrino oscillations [Fuk98; Ahm02; Egu03; Kat07]. Even though neutrinos are disfavoured as the dominant Dark Matter constituent because they damp small density fluctuations at the early universe, their great abundance could contribute significantly to the total den-

sity. One can calculate the contribution of the neutrinos to the total density of the universe $\Omega_\nu$ as a function of their assumed masses $m_\nu$ (in fact, the sum of the three different neutrino species $\Sigma m_{\nu_i}$):

$$\Omega_\nu = \frac{8\pi G}{3H_0^2}\, n_\nu\, \Sigma m_{\nu_i} \tag{1.22}$$

with the number density $n_\nu$ of the present day neutrinos. The neutrinos decouple from other particles, e.g. electrons and photons, at a temperature $T \sim 1\ MeV$ when their reaction rate becomes less than the expansion rate of the universe. Light neutrinos with $m_\nu < 1\ MeV$ are therefore still relativistic when they decouple (Hot Dark Matter) and their number density is linked to the photon density $n_\gamma$ [Dav81; Pee93]:

$$n_\nu = \frac{3}{4} \cdot \frac{4}{11} \cdot n_\gamma \ \simeq\ 113\ cm^{-3} \tag{1.23}$$

where the factor 3/4 comes from Fermi statistics and the factor 4/11 is due to the rise of $n_\gamma$ by $e^+e^-$-annihilation. The total density contribution for a Dirac neutrino (or half of this for a Majorana neutrino) can then be written together with equation (1.4) as [Jun96]:

$$\Omega_\nu = \frac{\Sigma m_{\nu_i}}{93eV}\ h^{-2} \tag{1.24}$$

The experimental limits on the neutrino masses are dominated by experiments determining the kinematics of triton decays ${}^3_1H \rightarrow\ {}^3_2H + e^- + \bar{\nu}$ [Kra05a]:

$$m_{\nu_e} < 2.3\ eV \quad (95\% C.L.) \tag{1.25}$$

This limit will be improved significantly by the upcoming Karlsruhe Tritium Neutrino Experiment (KATRIN) with an expected sensitivity of 0.2 $eV$ (90% C.L.) and a discovery potential of $m_{\nu_e} = 0.35\ eV$ with $5\sigma$ significance [Ang04].
Despite the experimental success and outlook on the neutrino mass measurements, astrophysical observations can also be used to limit the neutrino mass. The most stringent limit on the sum of all neutrino masses can be made by the combined study of the WMAP satellite data with the 2dF galaxy survey [Han07]:

$$\Sigma m_{\nu_i} \leq 0.65\ eV \quad (95\% C.L.) \tag{1.26}$$

and thus limiting the contribution of the neutrino masses to the total density of the universe to an almost negligible magnitude. However, neutrinos may still play an important role as Dark Matter and for structure formation if they are a subdominant component of a Cold Dark Matter (CDM) scenario. Leaving the fact that neither baryonic matter nor neutrinos can account for the full amount of Dark Matter needed in the universe, a new yet unknown component ought to be postulated from cosmology. This coincides with extensions to the standard model of particle physics providing a natural solution to this problem, which will be discussed in the next section.

### Weakly Interacting Massive Particles (WIMPs)

Since neither baryons nor massive neutrinos manifest the key contribution to the cosmic matter, as discussed in the previous sections, the question about the nature of the dominant Dark Matter component is still unsolved. To summarise, the non-baryonic candidate for Cold Dark Matter (CDM) must satisfy several conditions:

- it must be stable on cosmological time scales (e.g. about 10 $Gyr$),
- it must interact weakly to qualify as *dark*,
- it must have the right relic density $\Omega$ in the order of 0.25 $\Omega_{\text{tot}}$ and
- it must be heavy to account for CDM.

The most general candidates are therefore generically *Weakly Interacting Massive Particles*, so-called WIMPs, generally denoted $\chi$. The typical mass range for WIMPs is between 10 $GeV$ and a few $TeV$ and cross sections in the order of the weak strength, as will be discussed below. The present relic density of these particles can be easily calculated in the framework of the Big Bang theory.
In the very early universe, the particles $\chi$ were in thermal equilibrium since the temperature was much higher than the masses of the particles ($T \gg m_\chi$, where $m_\chi$ is the mass of $\chi$). The number density of these relativistic particles in the ideal gas approximation is $n_\chi \propto T^3$ [Bör93]. They are rapidly converting to lighter particles and vice versa via processes like $\chi\bar{\chi} \leftrightarrow l\bar{l}$, where $l\bar{l}$ are quark-antiquark, lepton-antilepton pairs, or as well Higgs and/or gauge boson pairs, if the mass $m_\chi$ is larger than the masses of these particles. After the temperature of the universe drops below $m_\chi$, the number density exponentially falls ($n_\chi \propto e^{-m_\chi/T}$) and the annihilation rate of the WIMPs $\Gamma_\chi = \langle\sigma v\rangle n_\chi$ with the thermal averaged total annihilation cross section $\sigma$ times the relative velocity $v$ becomes smaller than the expansion rate of the universe, that is $\Gamma_\chi < H$. The annihilation of the particles then becomes inefficient and a relic abundance remains, they 'freeze-out'. Quantitavely using the Boltzmann equation one can determine a matter contribution of the WIMPs to [Jun96]:

$$\Omega_\chi = \frac{8\pi G}{3H_0^2} m_\chi n_\chi \simeq \left(\frac{3 \times 10^{-27} cm^3 sec^{-1}}{\langle\sigma v\rangle}\right) h^{-2} \tag{1.27}$$

This approximation is independent of the WIMP-mass but is only determined by the total annihilation cross section. Figure 1.7 shows numerical solutions of the Boltzmann equation. The equilibrium (solid line) and actual (dashed lines) abundances per comoving volume are plotted as a function of $x \equiv m_\chi/T$, which increases with increasing time. As the annihilation cross section is increased, the WIMPs stay in equilibrium longer and the relic abundance today is smaller [Jun96].
Thus, to obtain a sufficiently large cosmological mass density, the cross section of these particles should be on the weak scale,

$$\sigma_{weak} \simeq \frac{\alpha^2}{m_{weak}^2} \tag{1.28}$$

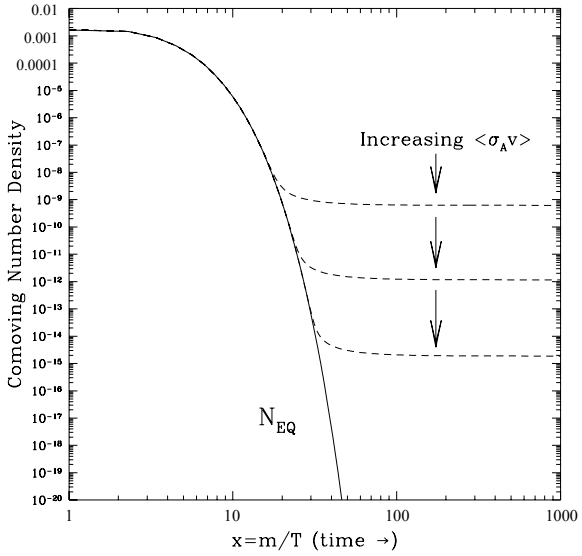


**Figure 1.7:** Comoving number density of a WIMP in the early universe. The dashed curves are the actual abundances and the solid line is the equilibrium abundance (taken from [Jun96]).

with $\alpha \simeq \mathcal{O}(0.01)$ and $m_{weak} \simeq \mathcal{O}(100\ GeV)$.

Within the standard model of particle physics, a heavy neutrino could be an ideal candidate. But as described in the previous section, the experimental mass limits of the known $\nu_e$, $\nu_\mu$ and $\nu_\tau$ exclude them. A fourth generation heavy neutrino was a possibility until measurements of the $Z^0$ width showed that there are exactly three neutrino families [Yao06]. Additionally a so-called 'sterile' neutrino [Oka97], a hypothetical neutrino that does not interact via any of the fundamental interactions but gravity is recently also experimentally disfavoured [Kat07].
However, extensions to the standard model, called *Supersymmetry*, predict a doubling of the existing particle. This theory is motivated to solve the hierarchy problem of particle physics as well as to unify the electro-weak forces with gravity towards a Grand Unified Theory (GUT). The new symmetry relates elementary particles of one spin to another particle that differs by half a unit of spin and are known as superpartners. Since the spectrum of the standard model does not provide such particles, the symmetry must be broken to allow the superpartners to have different masses, in fact much higher masses and are therefore not yet discovered. Normal and supersymmetric particles also differ by a new quantum number called R-parity. This quantum number may be conserved so that a lightest supersymmetric particle (LSP) would have to be stable. A detailed theoretical description of the motivations for supersymmetry, the framework of supersymmetric Lagrangians and the concepts of the Minimal Supersymmetric Standard Model (MSSM) can be found in [Mar97] and references therein.

Assuming supersymmetric models with the LSP being the lightest mass eigenstate of a general superposition of neutral spin-1/2 fermions, namely the photino (the superpartner to the photon), the Zino (the superpartner of the $Z^0$-boson) and the Higgsino (the superpartner of the neutral Higgs boson), the so-called 'neutralino' turns out to be an ideal Dark Matter candidate. The cosmic abundance of the neutralino would be determined by the freeze-out from thermal equilibrium, see eqn. (1.27), with their annihilation and scattering cross sections, as well as masses depending on specific parameters of the assumed supersymmetric model. Despite the strong theoretical motivation for supersymmetry, no convincing experimental evidence for the existence of supersymmetric particles has been found until today. The search for supersymmetric particles, with masses proclaimed to be around the weak scale, is one of the prime goals of future accelerators, most notably the Large Hadron Collider (LHC) at CERN, starting to operate in 2008. Until then, the cosmological need for a suitable CDM candidate is the strongest empirical hint to supersymmetry, with stringent limits on the neutralino mass and interaction cross sections from the nonobservation at present accelerators (see also [Yao06]).
Beyond the discussed neutralino, there are other particle Dark Matter candidates, which currently seem almost impossible to detect and which are beyond the scope of this work. For instance, the gravitino, the spin-3/2 superpartner of the graviton, the mediator particle of gravity states from the 'hidden sector' and thought responsible for supersymmetry breaking, can be a stable particle with masses in the $TeV$ range. This would be the case, if the gravitino is the LSP of R-parity conserving supersymmetric models. Another candidate is the axino, the spin-1/2 superpartner of the axion which will be discussed in the next section. For more details on supersymmetric particles and the current experimental limits to them, see [Yao06] and references therein.

### Axions

The axion is a hypothetical elementary particle to resolve the violation of the combined symmetries of charge conjugation and parity (CP violation) in quantum chromodynamics (QCD) as postulated by R. Peccei and H. Quinn [Pec77]. The idea is to promote the violating CP term in QCD to a field (thus a particle). This is accomplished by adding a new global symmetry (called Peccei-Quinn-symmetry) to the standard model that becomes spontaneously broken. Once this symmetry is broken, a new particle results and naturally relaxes the CP violation to zero. This new particle is hence called the axion. Explicit calculations of non-trivial QCD vacuum effects provide axion masses $m_A$ in a wide range of $10^{-12}\ eV \lesssim m_A \lesssim 10^6\ eV$ [Tur90]. The abundant non-thermal production of axions in the early universe makes the axion a compelling cold Dark Matter candidate. The axion's couplings to matter are thought to be extremely small, however, its conversion into two photons can be stimulated with the help of a resonant cavity and a strong magnetic field. This conversion also determines the principle of detection. Several ongoing experiments, such as *CAST* (CERN Axion Solar Telescope) [Zio05], *ADMX* (Axion Dark Matter eXperiment) [Ros04] and *PVLAS* (Probing Vacuum with polarised Light) [Zav06], are trying to

detect axions, so far without conforming success. Together with astrophysical and cosmological constraints, e.g. considering effects of axions on the evolution of stars of all types the limit on the axion mass is set to [Yao06]:

$$m_A \lesssim 10^{-2}\ eV \tag{1.29}$$

with an allowed mass window of interest to Dark Matter of $\mu eV \lesssim m_A \lesssim meV$. Ongoing and future experiments are expected to probe the couplings of axions to various particles and set limits on the contribution of axions to the Dark Matter content of the universe.

### MOdified Newtonian Dynamics (MOND)

As long as there is no experimental evidence for particle Dark Matter in the form of supersymmetric extensions to the standard model of particle physics, other solutions should be considered as well. Among these is the theory of *MOdified Newtonian Dynamics* (MOND), that proposes a modification of Newton's Second Law of Dynamics (and with it General Relativity), to explain for example the galaxy rotation problem. There have been a number of proposals as to how standard gravitational dynamics might be modified so as to correctly explain galactic dynamics without Dark Matter. Basically the modification first published by Mordehai Milgrom 1983 [Mil83] states that the simple equation $\vec{F} = m\vec{a}$ should be:

$$\vec{F} = m \cdot \mu(a/a_0) \cdot \vec{a}, \quad \text{with} \tag{1.30}$$

$$\begin{aligned} \mu(x) &= 1 \quad \text{if } x \gg 1 \\ \mu(x) &= x \quad \text{if } |x| \ll 1 \end{aligned}$$

This idea is based on the fact that Newton's law has never been verified in the case where the acceleration is extremely small, hence at the scale of galaxies, where the gravitational force is extremely small due to the very large distances. MOND has to face a lot of criticism among physicists and astronomers, since its based on experimental observations, rather than on fundamental physical principles as Einstein's General Relativity. Nevertheless, the idea keeps re-emerging with various modern justifications including relativistic expansions [San02; Bek04] and should be considered as an, though exotic, alternative to particle Dark Matter.

### Other candidates

This list of discussed candidates for Dark Matter is by no means exhaustive. Several more possibilities are considered, including 'fuzzy' CDM (particles with masses $m \sim 10^{-22} eV$), Chaplygin Gas (a type of fluid arising in certain string-inspired models involving $d$-branes), Q-balls (non-topological solitons in supersymmetric theories), primordial black holes and theories on Universal Extra Dimensions, where the

four-dimensional space time is embedded in a higher dimensional space. Special attention is set on the latter, since excitations of Standard Model states along the orthogonal dimensions, called Kaluza-Klein excitations, may be very viable Dark Matter candidates [Ser03]. The stability of the lightest of the Kaluza-Klein excitations can be arranged by a parity symmetry and masses around 1 $TeV$ provide reasonable relic densities, similar as with supersymmetric models. For further information, the reader is referred to [Yao06] and references therein.

## 1.4 WIMP detection methods

The observed existence of Dark Matter (DM) in the universe, together with the theoretical motivation by supersymmetric models, strongly favours dark matter particles not in form of familiar objects but of new weakly interacting particles. The lack of knowledge about the nature of the WIMP encourages astrophysicists to experimentally determine the particle properties, and a vast number of experiments are on the quest to detect DM. In principle, one can distinguish two methods to search for DM, either direct or indirect. Direct detection experiments depend on DM particles actually passing through detectors and physically interacting with them, while indirect searches are trying to detect secondary particles produced by annihilation of DM particles elsewhere. The basic concepts and the experimental challenges of the respective methods will be discussed in this section.

### 1.4.1 Indirect detection

Assuming the supersymmetric nature of WIMPs, the neutralino $\chi$ is its own antiparticle $\bar{\chi}$ (Majorana particles) and thus can annihilate while conserving R-parity via the following channels:

$$\chi\bar{\chi} \rightarrow l\bar{l},\ q\bar{q},\ W^+W^-,\ \text{or}\ Z^0Z^0,$$

with $l\bar{l}$ being lepton-antilepton and $q\bar{q}$ quark-antiquark pairs. Indirect dark matter searches are trying to detect the signal rate of WIMP annihilations by studying the products of these processes [Sil85; Kra86]. In case the produced leptons are **neutrinos**, the signal rate can be enhanced by the trapping of WIMPs in massive bodies, such as the Sun, the Earth or the Galactic centre. Due to the gravitational field of these objects, the WIMP density is enhanced until the annihilation rate equals the capture rate. Both quantities depend on the cross sections of the WIMPs and are usually calculated within the constraints on supersymmetric models. The neutrino flux can be derived taking into account the branching ratios for WIMP annihilations into neutrinos. The neutrino products are typically in the $GeV$ energy range and are hence accessible to existing solar neutrino experiments. However, the predicted rates are only a few events for kiloton detectors per year, while background events by cosmic ray muons occur at a much higher rate [Ber98]. Currently no neutrino telescope could determine any enhancement of neutrino fluxes towards massive cosmological objects, but with the planned enlargements

of current experiments, e.g. by the Amanda-IceCube collaboration [Ahr03] or with new future experiments, e.g. the proposed LENA experiment [Obe05], new sensitivities could be reached.

Cosmic $\gamma$**-rays** can also be found as WIMP annihilation signatures, since both continuum emission from $\chi\bar{\chi} \rightarrow \gamma Z$ and line features from $\chi\bar{\chi} \rightarrow \gamma\gamma$ are predicted [Ste89]. The continuum emission fluxes were predicted to be about two orders of magnitude lower than the diffuse galactic background. However, some enhancement would be expected in the direction of the galactic centre. Latest results by reanalysing the data from the EGRET space telescope on the diffuse $\gamma$-ray background claim a signal from dark matter annihilation [dB05]. A WIMP mass between 50 $GeV$ and 100 $GeV$ is deduced using background models for the diffuse photon background and constraint supersymmetric models to calculate the WIMP signal. Furthermore, a spherical isothermal DM halo model with substructures in the galactic plane leading to the peculiar shape of the galaxy rotation curve, is claimed to be consistent with the data. A similar approach on the extragalactic gamma ray background also measured by the EGRET telescope determines a WIMP mass $\sim 500\ GeV$ with systematic errors $\sim 30\%$ [Els05]. The upcoming satellite experiment GLAST [Geh99] will measure the diffuse galactic $\gamma$-ray spectrum up to energies $\sim 300\ GeV$, which is an order of magnitude higher than measured by EGRET. This higher energy range will make it possible (in case of a lower WIMP mass) to search for a cut-off of a DM annihilation signal at the WIMP mass.

Since in the products of WIMP annihilations matter and antimatter are equally distributed, **positron** and **antiproton** fluxes are expected to be produced in measurable enhancements. The positron flux from neutralino annihilation features around $50-100\ GeV$ and may be visible as bumps in the otherwise smooth background spectrum due to cosmic ray interactions with interstellar gas [dB02]. Antiproton fluxes from WIMP annihilation were expected to produce measurable enhancements above background fluxes in the low-energy antiproton spectrum. However, both signals are expected to be much below background levels, thus long-duration space missions will be needed to collect sufficient statistics. The long-planned NASA space instrument AMS [Bar04] and the satellite-borne apparatus launched in the year 2006 PAMELA [Pic07] will measure antimatter fluxes to determine a DM annihilation signal.

### 1.4.2 Direct Detection

Even though there exists firm evidence for a halo of Dark Matter in galaxies from the observed rotational curves and hints on their supersymmetric nature by annihilation signals from the galactic centre, it is essential to directly detect such matter. Hereby elastic collisions with the nuclei of a suitable target are studied. The possibility of such detection, however, relies on the nature of the dark matter particles [Goo85]. Besides, the theoretical and experimental results of direct detection depend on the Dark Matter distribution in our galaxy. The most

commonly used profile is the isothermal *NFW* (Navarro-Frenk-White) profile, with $\rho \propto r^{-2}$ to account for flat rotation curves, a local density of $\rho_0 = 0.3\ GeV\ cm^{-3}$ and a Maxwell-Boltzmann velocity distribution with a typical galactic virial velocity of $v_0 = 270\ km\ s^{-1}$ [Nav97] Together with WIMP masses of $m_\chi \geq 30\ GeV$ the energy transfer in elastic collisions with the nuclei of an appropriate target detector would be in the range of 1 to 100 $keV$.

Thus, the experimental task of direct detection experiments is to identify such small energy depositions in the target detector and to cope with the extremely low expected event signal rate. This event rate depends primarily on the coupling of WIMPs to the nuclei. Although supersymmetry is well motivated and theoretically highly developed, even in the minimal supersymmetric extensions of the standard models there are many undetermined parameters. Therefore numerical calculations of the event rate depend on various assumptions and are largely model dependent.

The WIMP couples potentially to a nucleus through a scalar interaction or to the spin through an axial-vector (spin) interaction. It is common to focus only on WIMPs with either scalar or spin interactions, although the most general WIMP may comprise a combination of both. Assuming a detector consisting of nucleus ${}^{Z}_{A}X = N$, the conventionally used total WIMP-nucleus cross section $\sigma_A$ can be written as:

$$\sigma_A = 4G_F^2 \mu_A^2 C_A \tag{1.31}$$

with the Fermi constant $G_F$ and the WIMP-target reduced mass $\mu_A = \frac{m_\chi m_A}{(m_\chi + m_A)}$ for WIMP mass $m_\chi$ and nucleus mass $m_A$, and an enhancement factor $C_A$ [Jun96]. Following [Jun96], the enhancement factor $C_A$ can be expressed in terms of WIMP-nucleon (i.e. free proton or neutron) cross sections $\sigma_p$ and $\sigma_n$ which can be calculated theoretically within specific supersymmetric models. By this convention, the comparison of various experiments using different target materials is essentially model independent, assuming only the general phenomenon of coherent scattering scaling as $A^2$.
The factor $C_A$ has to be calculated for the spin-independent scalar interaction between neutralino and the nucleus (SI) as well as for spin-dependent interaction (SD), respectively. For SI interaction, the experimentally deduced value of $\sigma_A$ is proportional to the mass square of the atomic number, since the effective WIMP couplings to the protons and neutrons are of the same magnitude for Majorana particles.

In the SD case, however, the situation is more complex. Here the enhancement factor is given by:

$$C_A = \frac{8}{\pi}(a_p \langle S_p \rangle + a_n \langle S_n \rangle)^2 \frac{J}{J+1} \tag{1.32}$$

where $a_p$ and $a_n$ are effective WIMP-proton and WIMP-neutron couplings and $\langle S_{p,n} \rangle = \langle N | S_{p,n} | N \rangle$ are the expectation values of the proton and neutron spins within the nucleus and $J$ is the total nuclear spin. It is clear that converting

experimentally deduced values of $\sigma_A$ to WIMP-proton cross sections $\sigma_p$ becomes problematic in the case of spin-dependent interactions due to the WIMP-model dependent coefficients $a_p$ and $a_n$.

### 1.4.3 WIMP Detector Technologies

A variety of techniques are presently in use for WIMP searches. Due to the numerous ways to achieve sensitivities to the WIMP properties; e.g. high $A$, high target mass, low threshold, low background, background-rejection and -subtraction techniques, etc.; only a few, among those the most successful and most promising ones, are discussed in this section. One of the main difficulties of any such technique is the low signal rate to be expected from supersymmetric model calculations. The typical counting rates are in the range of $1/kg/d$ to $1/t/y$, much lower than the usual radioactive backgrounds. Therefore, common to all WIMP searches is the goal to reduce the natural radioactive contamination by using extremely pure substances and to actively reject background events by special techniques.

Experimentally, there are several ways of particular importance to measure the event rate of WIMP-nucleus collisions discussed previously. First, one may search for scintillation light created by the energy deposit of the WIMP in the target detector, e.g. $NaI$ or $Xe$ detectors. Hereby, the recoiling particle directly or indirectly excites electrons to energy levels above their ground states, from which they may decay by emission of ultraviolet or visible photons. Due to the reasonably low backgrounds, by using ultrapure materials, and large masses achievable, scintillators are naturally used for annual-modulation searches[2] This has been successfully done by the DAMA-collaboration [Ber00], which claimed to have found an annual modulation on data taken over seven annual cycles. With the measured effect, the collaboration obtains a model independent evidence for the presence of a Dark Matter particle component in the galactic halo at $6.3\sigma$ C.L. However, the deduced value for the WIMP-mass $m_\chi = (59^{+17}_{-14})GeV$ and the WIMP-proton cross section $\sigma_p = (7.0^{+0.4}_{-1.2}) \times 10^{-6} pb$ remains the only claimed direct observation of WIMPs. No other experiment could yet confirm the observed signal. Moreover, the complete allowed parameter region by the DAMA-evidence is now excluded by other experiments, see figure 1.9. This incompatibility appears to hold regardless of modifications on the halo model or if spin-dependent interactions dominate [Ull01; Cop03; Sav04; Kra05b]. Though there remains debate particularly for the spin-dependent case to allow compatibility, the DAMA-collaboration is now running an expanded array, namely the 250 $kg$ LIBRA experiment [Ber06b] in operation since 2003, and plans a further upgrade towards one ton of target material [Ber07]. To test the results with an independent $NaI$-based detector, a 107 $kg$

[2] As a consequence of its annual revolution, the Earth should be crossed by a larger flux of Dark Matter particles roughly around June 2nd (when its rotational velocity is summed to the one of the solar system with respect to the Galaxy), hence leading to a higher event rate. Respectively, around December 2nd (when the two velocities are subtracted) the event rate is smaller.

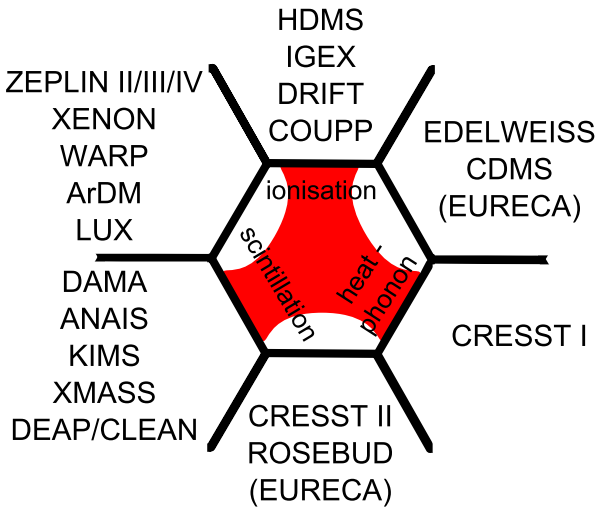


**Figure 1.8:** Summary of current and upcoming direct Dark Matter search experiments grouped according to the investigated signal channels. This list is not exhaustive.

$NaI$ experiment is being built at the underground laboratory Canfranc (Zaragoza, spain) [Ama06]. Also, the KIMS experiment based in South Korea has recently published competitive limits with $CsI$ detectors [Lee06] and excluding the complete DAMA-region as seen in figure 1.9.

Without regard to the exception of annual modulation, the described detection technology offers little or no direct background rejection capability. An important background rejection technique possible with many detectors is nuclear-recoil discrimination. In $NaI$ scintillators, this can be achieved by pulse shape, since nuclear recoils yield more quickly decaying scintillation pulses than electron recoils. The DAMA-collaboration has also demonstrated pulse-shape discrimination. However, the exclusion limit turns out to be dominated by the $2-3$ $keVee$ (electron equivalent) energy bin, in which they have essentially no discrimination capability due to a low signal-to-noise ratio.

Liquid noble gas detectors with scintillation readout have shown recently competitive WIMP sensitivities. Most notably has been liquid Xenon ($LXe$), started by the DAMA/LXe experiment [Ber02], but also recently liquid Neon and liquid Argon in the DEAP/CLEAN experiments [Bou04; Bou06]. Liquid Argon is also used in the current WARP-collaboration which has recently published very competitive exclusion limits [Ben07a]. Furthermore, Argon is also used for the yet-in-prototype stage ArDM experiment [Rub06] aiming towards one ton two-phase liquid Argon detector. $LXe$ as a target for WIMP detection, on the other hand, has particularly

good intrinsic properties, e.g. high mass, high scintillation and ionisation efficiency and high radiopurity. However, the recoil discrimination achievable is of greater importance. This is realised firstly, as in $NaI$ scintillators by pulse shape analysis of the scintillation light, which is the basis of single-phase $LXe$ experiments such as XMASS [Kim06] in Japan and UK-based ZEPLIN-I [Aln05b]. More powerful discrimination in $LXe$ can be achieved by recording also the ionisation produced by the WIMP-interaction. The recoiling nucleus travels through the target material before stopping, ionising atoms as it passes. The lower velocities of nuclear recoils though, induce less ionisation relative to the ionisation induced by electromagnetic interactions with electrons of the shell by $\beta$ and $\gamma$ radiation. This so called **quenching** helps to significantly lower the background rate for dark matter searches. In liquid noble gas detectors this yields to a different ionisation/scintillation ratio for nuclear and electron recoils, respectively. This detection principle is implemented by the ZEPLIN-II/III/IV [Wan05; Sum05; Ata05], the XENON 10/100 [Apr05], the XMASS-II [Kim06] and the recently formed LUX [Gai07a] experiments. To obtain stable operation conditions the current experiments use two-phase $LXe$. Hereby, the charge produced by the recoil first drifts out of the liquid into a gaseous phase, where a proportional scintillation signal (electroluminiscence) can be observed. Impressive results in terms of WIMP sensitivity has been made recently with both ZEPLIN-II [Aln07] and XENON10 [Ang07] experiments yet to be published. The exclusion limits determined by the two experiments is shown in figure 1.9.

Another way to detect WIMP-nucleus collisions in a target detector is to search for the ionisation signal in a semiconductor, notably in high-purity Germanium detectors. These detectors were initially used to look for the spectral-line signature of neutrinoless double $\beta$-decays of an isotope in the detector itself. The main problem of detectors of that type is the large background rate from natural radioactivity. However, the best limits have been achieved by the Heidelberg-Moscow and IGEX experiments [Bau01; Mor02]. Next generation experiments aim at a further reduction in activity and have been proposed, e.g. GENIUS [KK99] or are currently being built, e.g. the GERDA [Sch05] and MAJORANA [Aal05] experiments, all primarily aimed at neutrinoless double $\beta$-decays.

A further possibility to search for the energy deposition by a WIMP-nucleus scattering is the 'cryogenic' or 'bolometric' approach. Whereby one may cool the target to very low temperatures of around 10 $mK$, so that a 10 $keV$ energy deposit causes a measurable proportional increase in the detector temperature. This heating can be measured e.g. by a superconducting thermometer attached to the target which is shifted toward the normal conducting phase by the temperature increase. The initial prospect of detectors of this type was to obtain very low recoil energy thresholds combined with a very high energy resolution. However, it was soon demonstrated that a simultaneous measurement of the ionisation signal, together with the heat or phonon signal, also provides a good discrimination against electron recoils. Hereby as well, a recoiling nucleus produces proportionally less ionisation than an electron recoil of the same energy. Experiments using the hybrid

technique of simultaneous ionisation and heat collection are the EDELWEISS experiment ([Eit06], see chapter 2 for more details), as well as for example the CDMS experiment [AF05]. The latest sensitivity limits on the WIMP mass and WIMP-nucleon cross section of these experiments is also shown in figure 1.9.

As an alternative, the CRESST-collaboration [Bra99] has developed cryogenic $CaWO_4$ phonon detectors and pursued the use of scintillation for the second signal channel, next to the heat signal. Hereby instead of using photomultipliers to obtain the scintillation signal, a second phonon-mediated detector with a light absorber is placed adjacent to the primary detector. Results so far have been obtained using two 300 $g$ crystals at the Gran Sasso underground laboratory and are shown as well in figure 1.9. A similar approach with scintillating sapphire bolometers is undertaken by the ROSEBUD collaboration [Ceb02].

All the cryogenic experiments are currently progressing towards significant upgrades. CDMS proposes towards one ton of detector material in three subsequent phases [Ake06], as well as moving to a deeper underground laboratory, namely the SNOLAB site. The CRESST experiment is in its second phase [Ang05] currently taking data with ten $CaWO_4$ crystals ($\sim$ 3 $kg$) and first preliminary results have been presented at the TAUP2007 conference [Sei07]. Also the EDELWEISS experiment has reached its ambitious second phase with extensive upgrades concerning the cryostat housing the bolometers and the passive lead and polyethylen shielding, together with the installation of an active muon veto to tag cosmic ray induced background events. More details about EDELWEISS-II can be found in chapter 2. Besides the current progress of the CRESST and EDELWEISS collaboration, the next generation experiment, called EURECA [Kra06], as a joint effort of both collaborations (enlarged by new participants) is already in its early planning stage. EURECA aims towards a one ton cryogenic array using various targets and possibly both ionisation/thermal and scintillation/thermal bolometers with a sensitivity goal beyond $10^{-45}cm^2$ ($= 10^{-9}pb$) on the WIMP-nucleon cross section.

Besides the well established techniques discussed in this section, further approaches to detect Dark Matter directly are investigated. One promising technique uses superheated droplets detectors or 'bubble detectors'. The goal of these detectors is to detect single bubbles induced by nuclear recoils in heavy liquid bubble chambers. In this implementation of the method, the metastable state of the target liquid is preserved by dispersing it into a viscous/inmiscible gel, effectively resulting in a collection of mini-bubble chambers. The great advantage of this technique, besides the low costs, the room temperature operation and the well known detector technology is the nuclear recoil discrimination power. The energy distribution by an electron recoil is too distributed to cause a bubble to boil, contrary to nuclear recoils. Two ongoing experiments exploit this technique, namely SIMPLE [Gir05] and PICASSO [Aub06] and recently the COUPP experiment was installed at FermiLab in Chicago [Col07].

Finally, a powerful, though technologically challenging possibility to proof that a signal is of galactic origin is to correlate events with the earth's motion through the galactic WIMP halo. So, the goal is to measure the direction of the recoiling particle and to make use of the extreme diurnal modulation of the signal due to directionality of the WIMP 'wind'. This is the motivation behind the DRIFT [SI00; Aln05a], MIMAC [San07] and NEWAGE [Miu07; Nis07] experiments. An overview of the discussed Dark Matter detection experiments, not being exhaustive, in terms of signal channels of recoil events, is given in figure 1.8.

The expected interaction rate of WIMPs with the target nuclei depends, as mentioned above, mainly on two unknowns, the mass and the cross section of the WIMP. Hereby one has to take into account the uncertainties from the Halo model [Kam98]. The experimental observable of the experiments described in this section is the scattering rate as a function of energy. It is usually expressed (in case of SI WIMP-nucleon interaction) as a contour in the WIMP mass — WIMP-nucleon cross section plane, or rather as exclusion limits due to the non-observation of WIMPs. An overview of the actual best limits of some of the described experiments together with theoretical expectations from supersymmetric models [Bal03; Bal04; Bat04; Ros07] is given in figure 1.9. An overview of the estimated sensitivities of ongoing and future experiments in the same plane is given in figure 1.10.

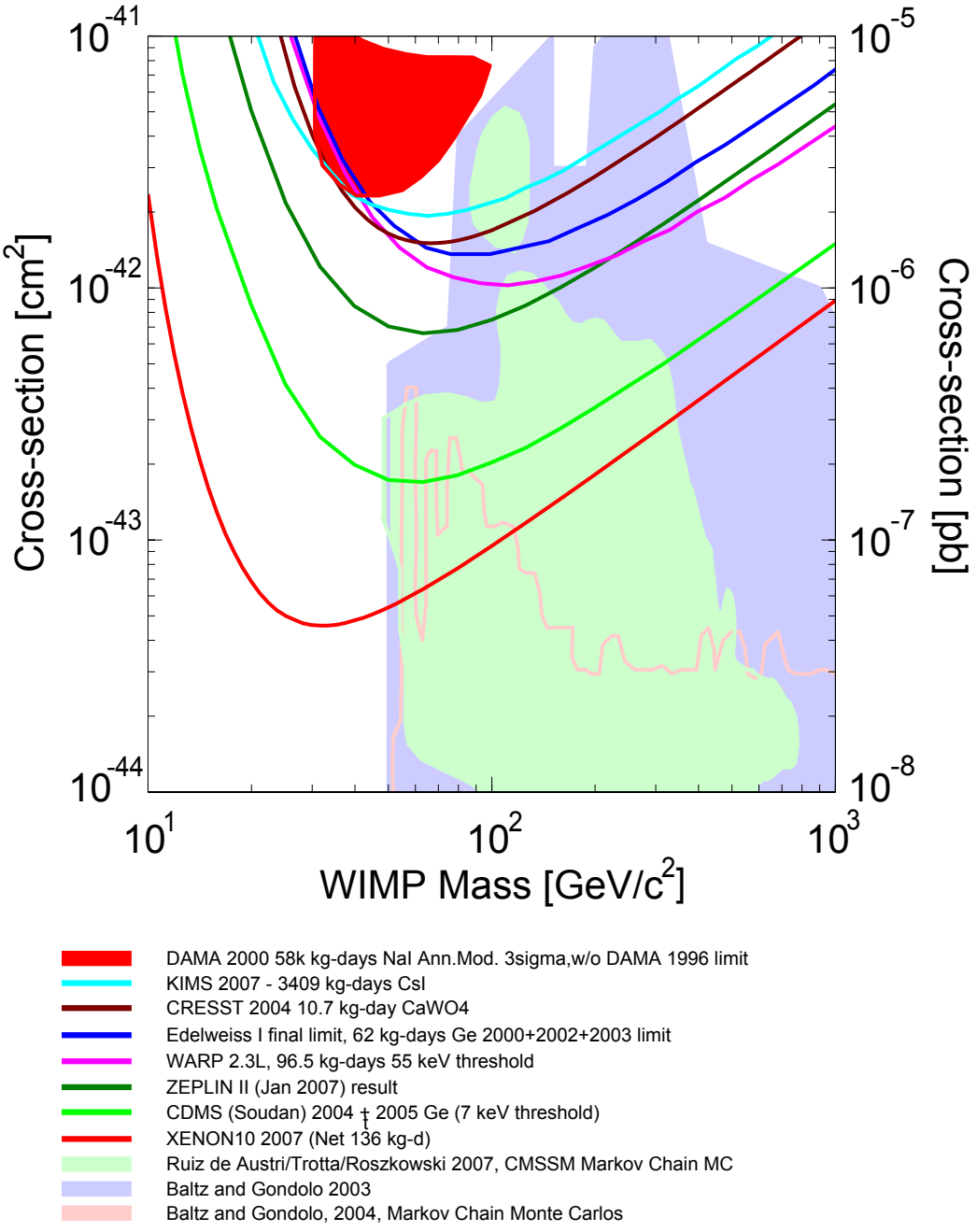


**Figure 1.9:** Current limits from various direct Dark Matter search experiments in the WIMP mass — WIMP-nucleon cross section (normalised to nucleon) plane. Figure is generated using [Gai07b]. For references of experimental data, see text.

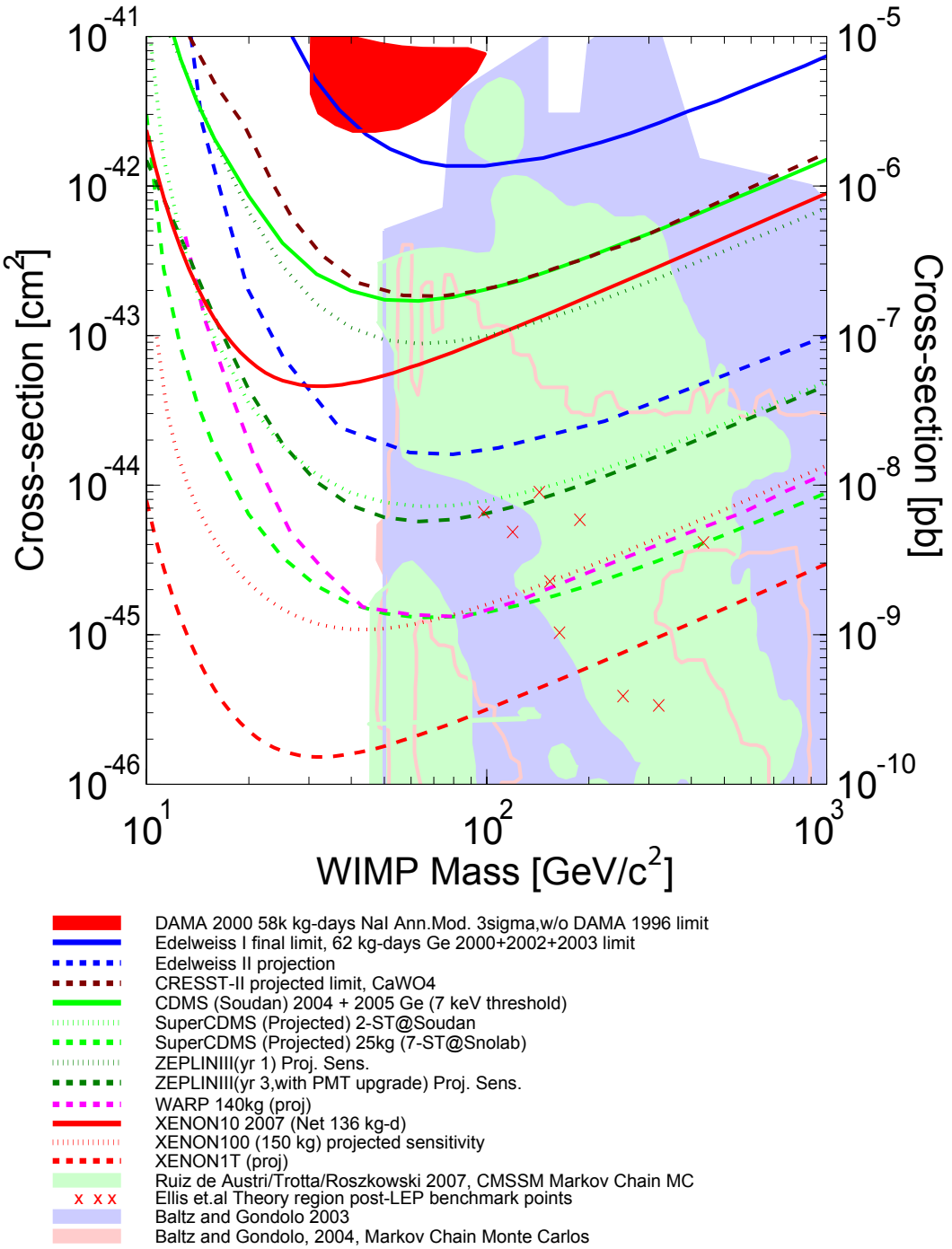


**Figure 1.10:** Current and expected limits from various direct Dark Matter search experiments in the WIMP mass — WIMP-nucleon cross section (normalised to nucleon) plane. Figure is generated using [Gai07b]. For references of experimental data, see text.

# 2 The EDELWEISS Experiment

The EDELWEISS (*Expérience pour DEtecter Les Wimps En Site Souterrain*) experiment is dedicated to directly detect Dark Matter in our galaxy. It is installed in the underground labaratory LSM (*Laboratoire Souterrain de Modane*) on the Fréjus highway tunnel between France and Italy. The collaboration consists of about 50 scientists from universities and research centres in France, Germany and Russia. Among those are the University of Karlsruhe (TH) and the Forschungszentrum Karlsruhe, currently merging into the Karlsruhe Institute of Technology (KIT). The goal of the experiment is to detect nuclear recoil events by the well-motivated Dark Matter candidate, the Weakly Interacting Massive Particle (see chapter 1.3 for details), scattering off the nuclei of the detector material. The detection principle of the EDELWEISS experiment, the results of the first phase (EDELWEISS-I) and the upgrade to the second phase (EDELWEISS-II) are the subjects of this chapter.

## 2.1 EDELWEISS-I

Already in 1994, the first installation of the EDELWEISS experiment was made in the underground laboratory of Modane [dB96a; Yvo96]. The main purpose of the first phase of the experiment, EDELWEISS-I, was to prove the principle of measuring simultaneously the heat and ionisation components of the energy deposit induced by the elastic scattering of a WIMP off a Germanium nucleus. By the final analysis of the EDELWEISS-I data with a total exposure of 62 $kg \cdot d$, see section 2.1.2, the experiment set the most sensitive limits on the WIMP mass and WIMP nucleon cross section until May 2004, see also section 1.4.3.

### 2.1.1 Detection principle and calibration

As described in chapter 1.4.2, the WIMP couples weakly to the nucleus of the detector material. Therefore one expects at most detection rates in the order of one event per kilogram detector material and day ($\Gamma \sim 1\ kg^{-1} \cdot d^{-1}$) [Yao06]. In contrast, natural radioactivity as well as cosmic rays generate by far higher rates of background events. Besides careful material selection in respect of radiopurity and operation in an underground laboratory to shield against cosmic rays, a sophisticated method to discriminate background events from WIMP-recoil events has to be installed. For this purpose, the EDELWEISS collaboration uses cryogenic Germanium crystals. The high-purity Germanium detectors, as shown in figure 2.1, have a mass of $m = 320\ g$ and are of cylindrical shape. The diameter is 70 $mm$ and the height is 20 $mm$. On the sides, the thickness reduces to 4 $mm$ due to beveled

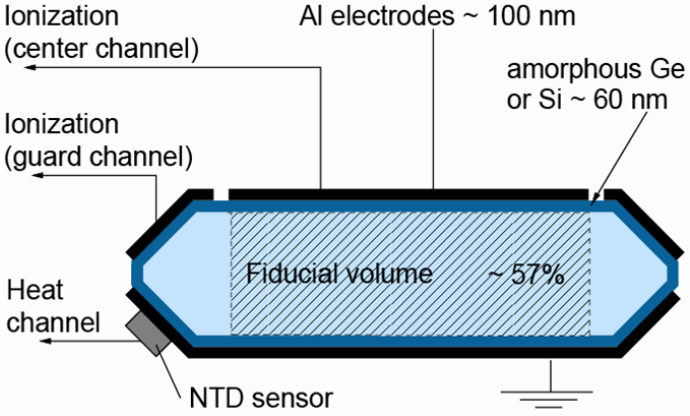


**Figure 2.1:** Schematic overview of an EDELWEISS heat and ionisation Germanium detector. The electrodes, the amorphous layer and the NTD thermometer are not represented to scale [Fio07].

edges in a 45° angle [Nav00].

These bolometers[1] experimentally acquire two signal channels per event simultaneously. First, the total recoil energy of the WIMP-nucleus interaction is determined by the overall temperature rise of the detector. The energy $\Delta E$ deposited in a calorimetric crystal by a scattering particle causes a temperature rise $\Delta T$:

$$\Delta E = C(T)\ \Delta T \tag{2.1}$$

where the calorimetric heat capacity $C(T) \propto (T/T_D)^3$ below the Debye temperature, e.g. $T \ll T_D$. For Germanium, the Debye temperature is approximately $T_D \approx 360\ K$. Consequentially, to lower the heat capacity and achieve a measurable temperature rise for very low energy deposits, the crystals need to be operated at very low temperatures. In case of the EDELWEISS experiment, the detectors have a base temperature of $T \sim 10 - 20\ mK$. As a result, an energy deposit of a scattering particle of for example $E \sim 10\ keV$ in a cryogenic Germanium detector of mass $m \sim 300\ g$, operated at a base temperature of $T \sim 20\ mK$, causes a temperature rise of $\Delta T \sim 1\ \mu K$. There are several ways to experimentally measure this tiny heating of the bolometers. For the EDELWEISS experiment, two of these methods are developed. As a reminder, phonons are quantised modes of vibration occurring in a solid crystal lattice. Once thermalised, these excitations correspond to the energy deposit in the crystal $\Delta E$ by a scattering particle. However, immediately after the collision, the phonons are not thermalised and $\Delta E$ and $\Delta T$ are not defined yet (until equilibrium is reached). Thus, e.g. rapid thermal sensors, sensible to athermal phonons (phonon signal) or slow sensors sensible to thermal phonons only

[1]The term bolometer is used for radiation detectors sensitive to the heat rise of an absorber resulting by any energy left inside the detector. The operating principle is similar to that of a calorimeter in thermodynamics but in the approximation of ultra low temperatures.

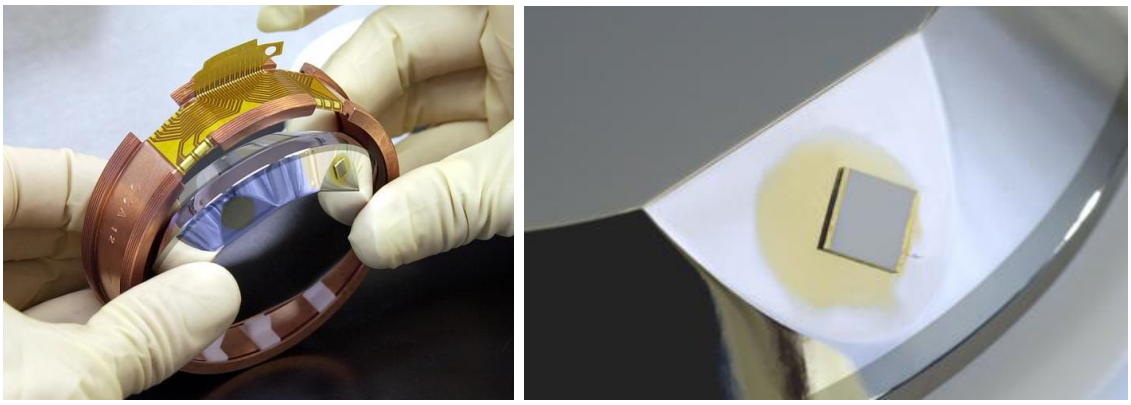

**Figure 2.2:** The EDELWEISS Germanium detectors. *Left:* Crystal within holding structure and the NTD thermistor glued on a golden pad on the beveled part of the crystal. *Right:* Close-up of the NTD thermistor.

(heat signal) can in principle measure the corresponding energy deposit [San05a].

The detectors used in the EDELWEISS-I experiment measured the heat signal of particles scattering in the crystal by a thermal resistor (or thermistor). The energy deposit by the thermal phonons in the absorber will induce a change of the resistance according to:

$$R(T) = R_0 e^{\sqrt{T_0/T}} \tag{2.2}$$

where $T_0$ is the characteristic temperature of the resistor and $R_0$ is a material dependent resistance. The values are typically in the order of a few $K$ or a few $\Omega$, respectively. For example, assuming a base temperature of $T \sim 20\ mK$, the resistance is $R \sim$ few $M\Omega$. The change of resistance of the thermistor at the boundaries of the crystal is proportional to the energy deposit of the incident particle. The thermistors of the EDELWEISS-I bolometers are 7 $mm^3$ Neutron Transmutation Doped (NTD) Germanium crystals[2] glued on a sputtered gold pad on the main Germanium crystal, see figure 2.2.
The sensors are polarised by individual constant currents $I$. In this manner the rise of temperature in the absorber gives rise to a variation $\Delta R$ of the thermal resistance and induces a voltage fluctuation $\Delta V$ corresponding to the heat signal:

$$\Delta V = \Delta R \times I \tag{2.3}$$

For example, for the above mentioned temperature rise of $\Delta T \sim 1\mu K$, the voltage change is $\Delta V \sim 1\ \mu V$.

Apart from the NTD-thermistors, the EDELWEISS collaboration also developed thin film detectors to measure the athermal phonon signal [Mar98]. These films

[2]The NTD thermometers have been produced by J.P. Torre (IAS, Orsay) and J. Mangin (Université de Bourgogne, Dijon) and by Haller-Beeman Associates.

are obtained by evaporating various materials, mainly $NbSi$, on the surface of the crystals, whose electric resistance is strongly dependent on the temperature. The advantage of these thin film phonon detectors is the possibility to determine, by comparing the signal ratio of each side of the crystal, the position of the interaction. This is of great importance to reduce near-surface events with bad charge collection misinterpreted as nuclear recoil events (see also section section 2.2.3 for more details on detector improvements).

The second signal channel, namely the ionisation yield of recoiling particles, is measured with the EDELWEISS-crystals by applying a bias voltage to the crystal and collecting the electron-hole pairs created by the interaction in the polarised crystal. The electrodes are made of 100 $nm$ thick Aluminium layers sputtered on the upper and lower side of the detectors. The top electrode is divided into a central part and a guard ring, electrically decoupled for radial localisation of the charge collection. The bottom electrode is the common reference. Between the electrodes a moderate voltage between $\pm 3\ V$ and $\pm 9\ V$ is applied. The charge carriers (i.e. electron-hole pairs) created in the crystal by the particle interaction drift along the electrical field lines towards the electrodes where they are collected. The shape and the rise time of the resulting charge signal are dependent on the position of the interaction. The average electron drift time $t$ in the Germanium crystals of $d = 2\ cm$ thickness and an applied electrical field $E = U/d$ is approximately [San05a]:

$$t = \frac{d}{v_D} = \frac{d^2}{\mu\ U} \approx 3.3\ \mu s \tag{2.4}$$

where $v_D = \mu\ E$ is the drift velocity in the electrical field. The electron mobility in Germanium is $\mu \approx 2 \times 10^5\ cm^2 s^{-1} V^{-1}$. For the applied voltage of the EDELWEISS bolometers, e.g. $U = 6\ V$, the electron drift time can be approximated to $t \approx 3.3\ \mu s$. The complete charge collection is essential to determine the type of interaction, i.e. electron or nuclear recoil, see also section 1.4.3. However, incomplete charge collection can occur by three different phenomenons. First of all, in Germanium electrons and $\alpha$-particles (with kinetic energies of several tens of $keV$) have a mean free path of only a few $nm$. Therefore the interaction of these particles, for Dark Matter searches considered as background events, in principle takes place very close to the surface of the crystals [Ben00]. It is possible that the created charge carriers are collected by the inadequate (or wrong-signed) electrode due to the proximity of the interaction to the electrodes. For these near-surface events, the measured ionisation signal may represent for example only a half of the in reality deposed charge carriers. In [Shu00] it is shown that introducing an additional amorphous layer between the electrodes and the crystal significantly reduces the collection of wrong-signed charges. An amorphous dead layer of either Germanium or Silicon is used for all EDELWEISS-I detectors and has a thickness of $d \sim 60\ nm$, see figure 2.1. The second phenomenon leading to incomplete charge collection is due to the presence of inpurities in the crystal. Charge carriers created by the interaction can be trapped and induce the formation of space charges which impede the flow of charge carriers. To limit this effect degradation or regeneration phases are

conducted every few hours during data taking [Cen04]. Thirdly, inregularities of the electrical field lines, e.g. on the lateral sides where electric field lines can escape before they reach the electrodes, can also lead to incomplete charge collection. Therefore the segmented electrode (centre and guard ring electrode) is used to additionally acquire information on the position of the interaction. Altogether, in the data analysis a fiducial volume is defined, where the electric field is the most uniform, a reliable charge collection is expected and the detector is better shielded from its environment.

Though increasing the applied voltage, and thus the electrical field, would in principle improve charge collection, a moderate voltage, typically between $\pm 3V$ and $\pm 9V$ depending on the detector, is essential to limit additional heating of the crystal due to the drift of the charge carriers. This effect is generally known as the Neganov-Luke-effect [Neg85; Luk88] and has to be subtracted in the analysis of the heat signal:

$$E_R = (1 + \frac{V}{\epsilon_\gamma})E_H - \frac{V}{\epsilon_\gamma}E_I \tag{2.5}$$

where $E_R$ is the energy deposit by the particle interacting in the detector, $V$ the bias voltage and $\epsilon_\gamma = 3\ V$ the mean electron-hole pair creation potential in Germanium for $\gamma$-ray interactions (electron recoils). $E_I$ and $E_H$ are the ionisation and heat signal amplitudes as obtained by calibration of the detectors [Mar04b]. It is very convenient to define a new value, the so-called *quenching*-value $Q$ as:

$$Q = \frac{E_I}{E_H} \tag{2.6}$$

since nuclear and electron recoils correspond to different ionisation efficiencies. In the EDELWEISS experiment, $E_I$ and $E_H$ are calibrated using $\gamma$-ray sources, so by definition $Q \equiv 1$ for electron recoils. For nuclear recoils, e.g. by neutrons as well as by the possible WIMP-nucleus interaction, the $Q$-value is on average three or four times lower than for electron recoils depending on the energy. This effect of a reduced ionisation yield for nuclear recoils has been extensively studied and experimentally measured repeatedly. In these experiments, the ionisation signals are first calibrated using $\gamma$-ray sources producing electron recoils. The detectors are then exposed either to monoenergetic neutron beams or to a well known neutron source, e.g. $^{252}Cf$, and the quenching factor $Q$ is determined. For each individual detector of the EDELWEISS-I experiment, the average value of the quenching factor $\langle Q_n \rangle$ for nuclear recoils is measured for different recoil energies $E_R$. In general, $\langle Q_n \rangle$ can be parametrised as [Lin63]:

$$\langle Q_n \rangle (E_R) = a\ (E_R)^b \tag{2.7}$$

with the values $a$ and $b$ resulting from the experimental data. As quoted in [dS01], measurements for all EDELWEISS-I detectors were performed and the values $a = 0.16$ and $b = 0.18$ are found to be consistent within the statistical errors.

In analogy with the ionisation quenching factor $Q$, one can introduce a quenching factor $Q'$ for the heat signal in thermal detectors. This factor is expected to be close to unity, i.e. $Q' \approx 1$. However, the determination of the energy calibration for nuclear recoils, and consequently the energy threshold of the detectors, rely on the value of $Q'$. Possible sources for a deviation of $Q'$ are expected to be small, but precise measurements are very scarce. For the Germanium detectors used by the EDELWEISS collaboration, the heat quenching factor is indirectly measured using measurements of the ratio $Q/Q'$ by neutron calibrations and the direct measurement of $Q$. The result for the quenching factor is $Q' = 0.91 \pm 0.03 \pm 0.04$ for recoil energies between $20 < E_{\mathrm{rec}} < 100\ keV$, where the two errors are the contribution from the $Q$ and $Q/Q'$ measurements, respectively [Ben07b].

Besides the experimentally determined quenching factor $Q$, to define confidence intervals to separate electron from nuclear recoils, the statistical standard deviations of the electronic and nuclear distribution $\sigma_{Q_\gamma}$ and $\sigma_{Q_n}$ respectively must be calculated. By propagation of the experimental values $\sigma_I$ and $\sigma_H$ in (2.5) and (2.6), one obtains:

$$\sigma_{Q_\gamma}(E_R) = \frac{1 + V/3}{E_R}\sqrt{\sigma_I^2 + \sigma_H^2} \tag{2.8}$$

$$\sigma_{Q_n}(E_R) = \frac{1}{E_R}\sqrt{(1 - \frac{V}{3}\langle Q_n\rangle)^2\sigma_I^2 + (1 + \frac{V}{3})^2\langle Q_n\rangle^2\sigma_H^2} \tag{2.9}$$

Using this information one can project the events from the calibration runs for each detector in the $(E_R, Q)$ plane, the so-called $Q$-plot. Figure 2.3(a) shows the $Q$-plot for one of the detectors used in the EDELWEISS-I setup, namely GGA1[3]. Also included in this figure are the 90% C.L. zones for electron and nuclear recoils respectively ($\pm 1.645\sigma$ to $\langle Q_\gamma\rangle$ and $\langle Q_n\rangle$). In this representation events associated with the inelastic scattering of neutrons on $^{73}Ge$ with 13.26 and 68.75 $keV_{ee}$ excitation levels, respectively, are expected to follow the dashed lines. The experimental ionisation threshold corresponds in this plane to the dotted hyperbolic line, which is determined by the trigger efficiency of a single detector reaching 50%.
In figure 2.3(b) the recorded data during a neutron calibration run is plotted with different triggering conditions. First, events with any other detector triggering (*here:* GeAl9 or GeAl10) represented by the solid line and secondly events with the additional condition of GGA1 also triggering (hatched area). 100% trigger efficiency is reached at an energy $E_I = 5\ keV_{ee}$ corresponding to a recoil energy $E_R = 20\ keV$ [Mar04b].

[3]The different detectors used in the EDELWEISS-I experiment are named and consecutively numbered according to their composition, e.g. *GeAl* are Germanium crystals with an Aluminium layer as electrode sputtered on the surface after etching. *GGA* crystals have an additional hydrogenated amorphous Germanium layer under the electrodes, while *GSA* detectors have an amorphous Silicon layer.

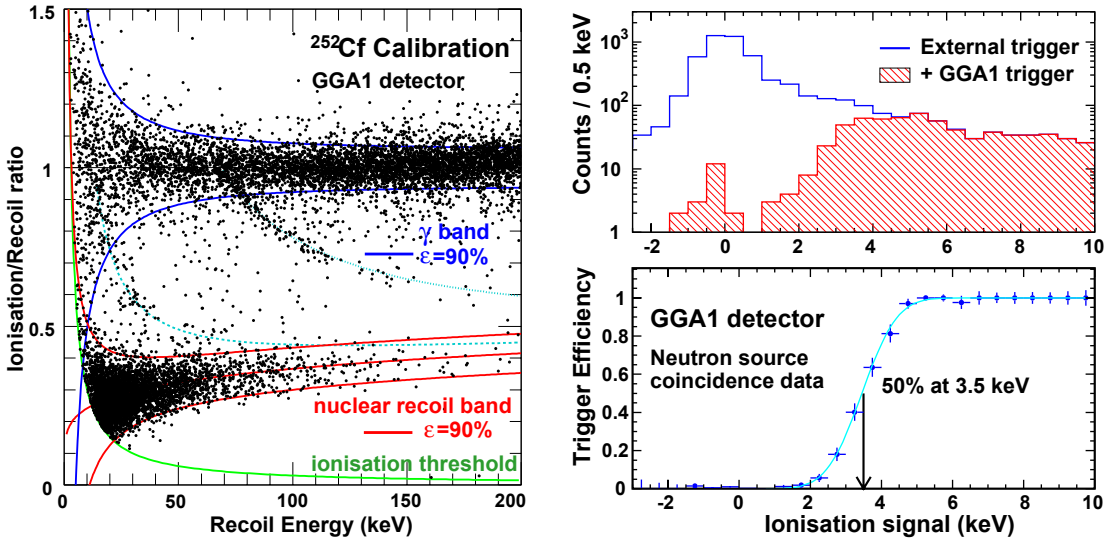


(a) neutron calibration

(b) ionisation trigger efficiency

**Figure 2.3:** (a) Events collected in the GGA1 detector during a calibration run, with the 90%*c.l.* zones for electron and nuclear recoils (*solid*), ionisation threshold of $E_I = 3.5\ keV_{ee}$ (*dotted*) and lines associated with inelastic scattering (*dashed*). (b) *Top:* Data recorded with the GGA1 detector during neutron calibration. *Bottom:* Experimental efficiency curve corresponding to the ratio of the two distributions from the top panel. See text for details.

### 2.1.2 Final results of EDELWEISS-I

The EDELWEISS experiment is located in the LSM underground laboratory which provides an approximately 4600 *m.w.e.* rock shielding against cosmic ray muons, see chapter 4 for more details on the rock overburden and muon background issues. In the first phase of the experiment, up to three 320 $g$ Germanium detectors were operated in a low-background dilution cryostat at a temperature of 17 $mK$. The accumulated data of EDELWEISS-I represents a total fiducial exposure of 62 $kg \cdot d$. The experimental setup is described in detail in [Ben01; Ben02; Mar04b], but the most relevant aspects will be summarised here shortly. The base temperature was reached with the use of a so-called dilution cryostat. In this type of cryostat, a special mixture between two helium isotopes (10% of $^3He$ and 90% of $^4He$) separates into two phases below a temperature of 0.8 $K$, one enriched with $^3He$ and one with $^4He$. The migration of $^3He$ from the former phase to the latter is a phase transition and occurs with a heat absorption. Such kinds of cryostats reach temperatures as low as $T = 2\ mK$.

The EDELWEISS-I cryostat, considering background issues in terms of natural radioactive isotopes, was made mostly out of ultrapure copper. To shield the cryostat from the radioactive environment, 10 $cm$ of copper and 15 $cm$ of lead [dB96b] was surrounding the experiment. Around the cryostat pure nitrogen gas

was circulated to reduce Radon accumulation. An external 30 $cm$ of polyethylene further protected the experiment from neutrons created in the surrounding rock. To minimise intrinsic contamination, the radioactivity of all materials in the close vicinity of the detectors was measured using dedicated low-background Germanium $\gamma$-ray detectors. Inside the cryostat, the detectors are shielded from the radioactivity of the electronic components by 7 $cm$ of archaeological lead[4]. A photograph of the innermost part of the cryostat, including three installed bolometers and the archaeological lead, is shown in figure 2.4(a). Figure 2.4(b) represents a schematic cut view of the cryostat inside its copper (orange) and lead (grey textured) shields as implemented in *Geant3* Monte Carlo simulations. Not represented here is the polyethylene shielding. The inset of figure 2.4(b) shows the Germanium detectors encased into their individual copper casings and holding structures in more detail.

Though great effort was made to shield the detectors from external radiation, the remaining interactions in form of $\gamma$-rays exceed the one expected from WIMPs by at least a factor of $10^5$. Therefore the active discrimination method of the EDELWEISS-experiment to separate electron recoils (by $e^{\pm}$ and $\gamma$) from nuclear recoils (by neutrons and WIMPs) is of great importance. Using the fact, that for the same interaction energy the ionisation efficiency for nuclear recoils is less than for electron recoils (see also section 1.4.3 and 2.1.1), it is possible to reject more than 99.9% of the gamma interactions while keeping a 90% efficiency for the nuclear recoils down to an energy of 10 $keV$ [San05b]. As discussed in section 2.1.1, the EDELWEISS bolometer technology uses an additional layer of amorphous Germanium (GGA detector type) or Silicon (GSA detector type) just below the electrodes to minimise near-surface events with incomplete charge collection. Furthermore, the twofold electrode (a center part and an outer guard ring) allows to define a fiducial volume for data analysis of around $\sim 57\%$ of the total crystal volume, see figure 2.1.

The first phase of the EDELWEISS experiment showed over periods of four months stable running conditions and accumulated a total fiducial exposure of 62 $kg \cdot d$ using several different Germanium detectors and up to three simultaneously. An energy threshold better than 15 $keV$ could be achieved with the detectors. The accumulated events of three detectors (representing a total exposure of 22.7 $kg \cdot d$) are shown in figure 2.5(a). However, in the total exposure of 62 $kg \cdot d$, 59 nuclear recoil candidates are recorded between 10 and 200 $keV$, with three of them in the critical energy range for establishing limits on WIMP interactions between 30 and 100 $keV$. The average count rate between 30 and 200 $keV$ is $6 \times 10^{-4}$ counts/$keV$/$kg$/$d$. The recoil energy spectrum of all these events together with simulated WIMP spectra using a WIMP-nucleon scattering cross-section $\sigma_{W-n} = 10^{-5}$ $pb$ for WIMP masses $M_W = 20$, 40, 100 and 500 $GeV/c^2$ is shown in figure 2.5(b). As can be seen, the distribution of events is not consistent with a WIMP-recoil spectra and thus these events may be

[4]Archaeological lead is used since $^{210}Pb$ has a half-life of $t_{1/2} \sim 22.3y$ and in old lead, aged over several centuries, the $^{210}Pb$ content is negligible. The archaeological lead used for EDELWEISS was retrieved from a sunken antique roman ship [L'H87].

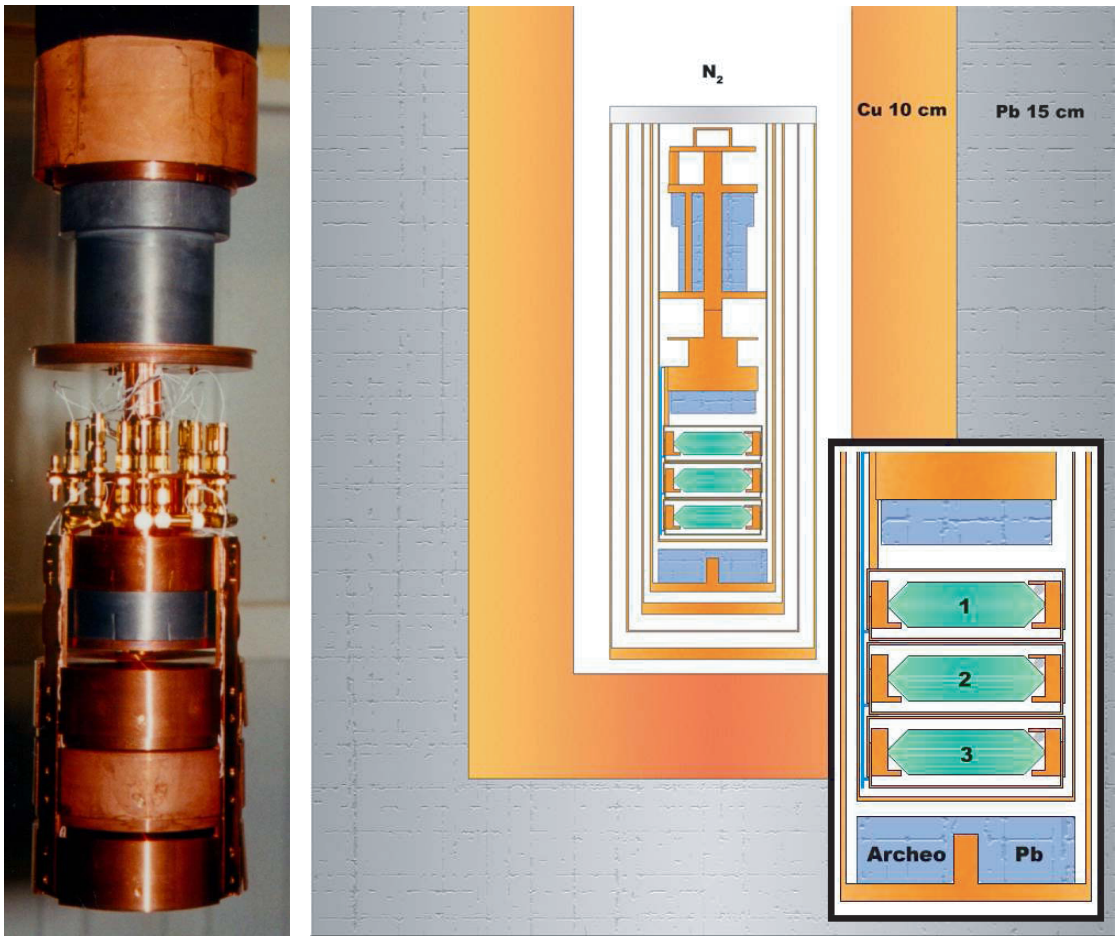


(a) Photograph (b) Schematic view of EDELWEISS-I

**Figure 2.4:** Photographic (a) and schematic (b) overview of the EDELWEISS-I cryostat. The inset of (b) shows three Germanium detectors encased into individual copper casings [Fio07].

interpreted as background. Two likely sources of background can be revealed by studying detector coincidences and the charge collection signal: a residual neutron background and surface electron recoils events [Lem06; Nav07].

The optimum interval method derived in [Yel02] was used to extract an upper limit on the spin-independent WIMP-nucleon cross section as a function of the WIMP mass. The final result of EDELWEISS-I is illustrated in figure 1.9 (blue line). Since the EDELWEISS-I experiment was limited by background, a new setup including better shielding and larger detector volume was proposed to overcome the limitation. This second phase of EDELWEISS is the subject of the following section.

The EDELWEISS experiment, using Germanium bolometers with natural abundances on $^{73}Ge$ (7.8%), a high-spin Ge isotope, set also limits on the spin-dependent WIMP-nucleon cross section. The complete data set of the first phase contains a fiducial exposure of 4.8 $kg \cdot d$. The determined sensitivity is competitive in compar-

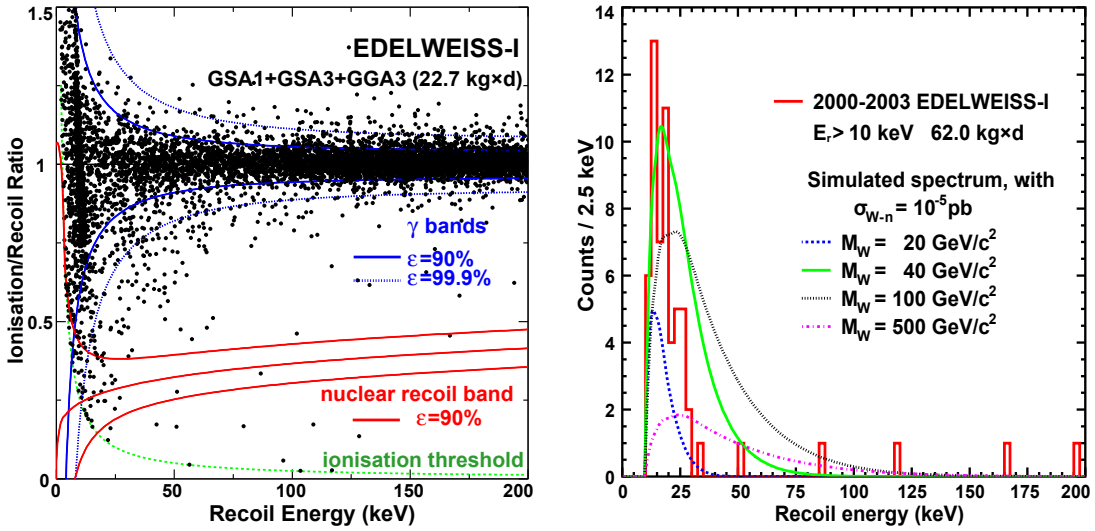


(a) EDELWEISS-I accumulated data of three detectors (GSA1, GSA3 and GGA3)

(b) Recoil energy spectrum of EDELWEISS-I recoil candidates

**Figure 2.5:** (a) Accumulated events in the fiducial volume of three detectors (GSA1, GSA3 and GGA3) and the 90%*c.l.* (solid) and 99.9%*c.l.* (dotted) zones for electron and nuclear recoils respectively. The hyperbolic dashed curve represents the ionisation threshold [San05b]. (b) Recoil energy spectrum of events in the nuclear recoil selection $E_R > 10\ keV$ for a total fiducial exposure of 62 $kg \cdot d$ compared with simulated WIMP spectra [San05b]. See text for details.

ison to other spin-sensitive WIMP Dark Matter experiments, but is still two orders of magnitude higher than the most optimistic supersymmetric model predictions [Ben05].

## 2.2 EDELWEISS-II

The first phase of the EDELWEISS experiment successfully proved the detection method of the heat-and-ionisation Germanium crystals. The experimental volume in the EDELWEISS-I setup however was limited to one liter. To significantly increase the rate at which exposure can be accumulated a larger size dilution cryostat is used in the setup of the second phase of the experiment, denoted by EDELWEISS-II [dS05]. To accomplish the envisioned increase in sensitivity on the spin-independent WIMP-nucleon cross-section of EDELWEISS-II by a factor of ×100 [Ger05] a new shielding concept had to be realised, see section 2.2.1. Furthermore an active muon detector is installed to veto muon-induced neutrons as possible background, see section 2.2.2. New detectors are also developed within the second phase of the experiment to further improve the rejection of near-surface events, see section 2.2.3.

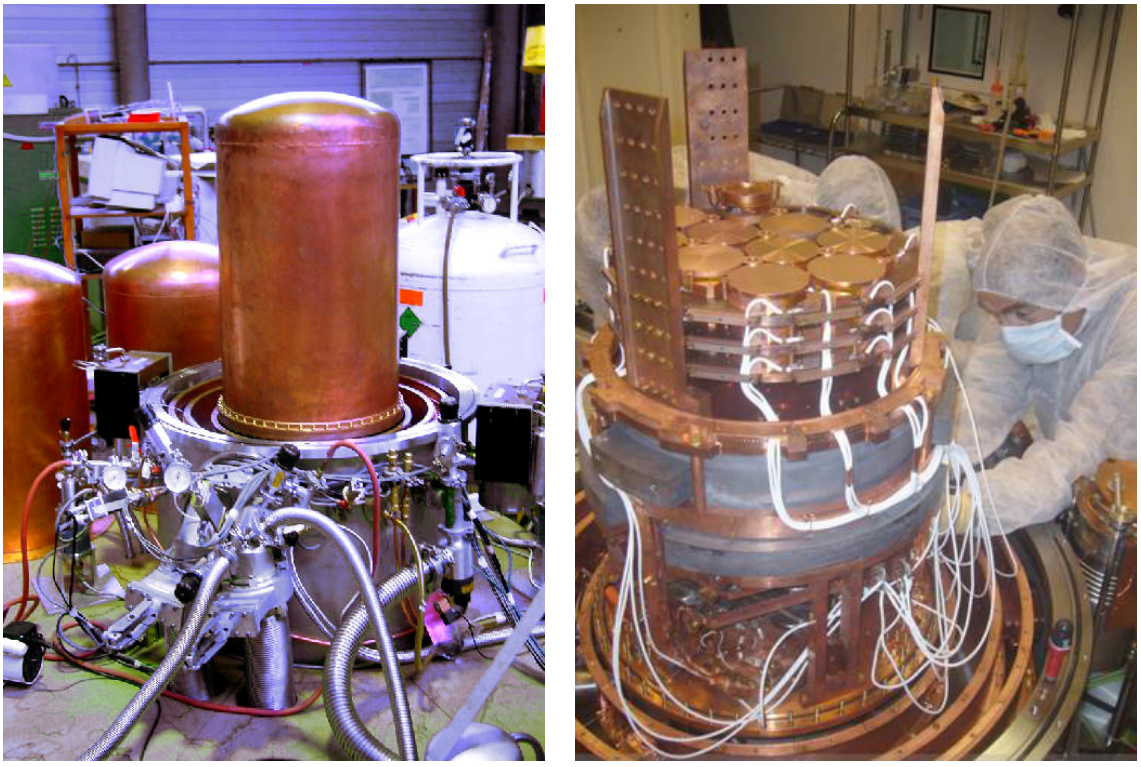

**Figure 2.6:** The EDELWEISS-II inverse cryostat before installation at LSM (right) and at current phase (September 2007) with 28 bolometers installed at LSM (left) [Ger07].

### 2.2.1 The new shielding concept

Theoretical predictions by supersymmetric extensions to the standard model of particle physics expect a WIMP-nucleon cross section well below $10^{-42} cm^2 (= 10^{-6} pb)$. To reach this sensitivity one has to increase foremost the total exposure time of the detectors significantly. Because of the limitation of the EDELWEISS-I setup to accommodate a maximum of only three $320g$ Germanium detectors in the cryostat, a larger cryostat is used in the second phase of the experiment. The new EDELWEISS-II cryostat has a total volume of $V \sim 100\ l$ and can accommodate up to 120 bolometers with a total mass of 38.4 $kg$. Its operating temperature of $T = 10\ mK$ with fluctuations less than $\pm 10\ \mu K$ is reached by the principle of a dilution refrigerator. The working principle of such cryostats is explained in section 2.1.2.

The inverted geometry of the newly developed EDELWEISS-II cryostat, as illustrated in figure 2.6, simplifies the installation and maintenance of the detectors as well as reduces the susceptibility to vibrations by the pumping system. Furthermore, by placing the complete cryogenic pumping system with all supply tubes below the bolometers, a more uniform shielding of the detectors can be realised.

The innermost shielding of the bolometers, besides their individual copper casings and some archaeological lead inside the cryostat, are the copper walls of the cryostat itself, followed by 20 *cm* of lead and 50 *cm* of polyethylene. Since all materials in the close vicinity of the detectors are subject to radiopurity limitations, the innermost 2 *cm* of the total 36 *t* of lead comes from archaeological sources [dB96b]. The contamination by $^{238}U$ in this lead is less than 1 *ppb*. The main purpose of the polyethylene shielding is to moderate and absorb neutrons from natural radioactivity in the rock surrounding the underground laboratory. The mean neutron energy of these processes is around a few $MeV$. After the moderator material, the energy of most of the neutrons is therefore not sufficient to penetrate the lead shielding. Thus the neutron flux towards the detectors from radioactivity in the rock can be significantly reduced [Cha04], see also chapter 5 and 6.

To allow easy access to the cryostat for installation and maintenance purposes, the experimental setup of EDELWEISS-II is separated into two horizontal levels. The lower part[5], 'Niveau 0', below an inserted ceiling, houses most of the cryogenic system. The upper part, 'Niveau 1', consists of two movable waggons with the lead and polyethylene shielding mounted on tracks. Hence the complete shielding can be opened to access the cryostat as illustrated in figure 2.7. The complete Niveau 1 of the experiment is placed in a permanent cleanroom[6] of class 10000 and while accessing the cryostat a temporary cleanroom of class 100 is installed.

### 2.2.2 Muon veto system

To reach the high sensitivity goal of EDELWEISS-II, it is important to consider also formerly negligible background sources. Headmost, neutrons induced either directly by cosmic ray muons or indirectly by electromagnetic processes in the shower of a muon have to be considered as a limiting background source. Therefore the new setup of EDELWEISS-II also contains an active muon shield. The main purpose of this so called muon veto counter is to reject neutron recoil events in the bolometers by associating them with a cosmic ray muon in the vicinity of the experiment. The muon detector consists of plastic scintillator modules placed almost hermetically around the experiment to maximise the muon detection efficiency.

As illustrated in figure 2.7, in total 42 plastic scintillator modules of the type BC-412 from BICRON® Saint-Gobain Industrial Ceramics, Inc.[7] are used for the EDELWEISS-II setup. The single modules are 65 *cm* wide, 5 *cm* thick and have lengths of 2 *m*, 3.15 *m*, 3.75 *m* or 4 *m* and adding up to a total area of $\sim$ 100 $m^2$. Groups of four 2″ Philips® VALVO XP 2262 photomultipliers are

[5]Notations in French language became customary within the collaboration.

[6]Cleanrooms are classified according to the number and size of particles permitted per volume of air. Class 10000 or class 100 (US FED STD 209E) denotes the number of particles of size 0.5 $\mu m$ or larger permitted per cubic feet ($ft^3$) of air, corresponding to the ISO-146441-1 standards ISO-7 and ISO-5, respectively.

[7]Saint-Gobain Cristaux Europe, 104 Route de Larchant, BP 521, 77794 Nemours CEDEX, France (http://www.bicron.com/).

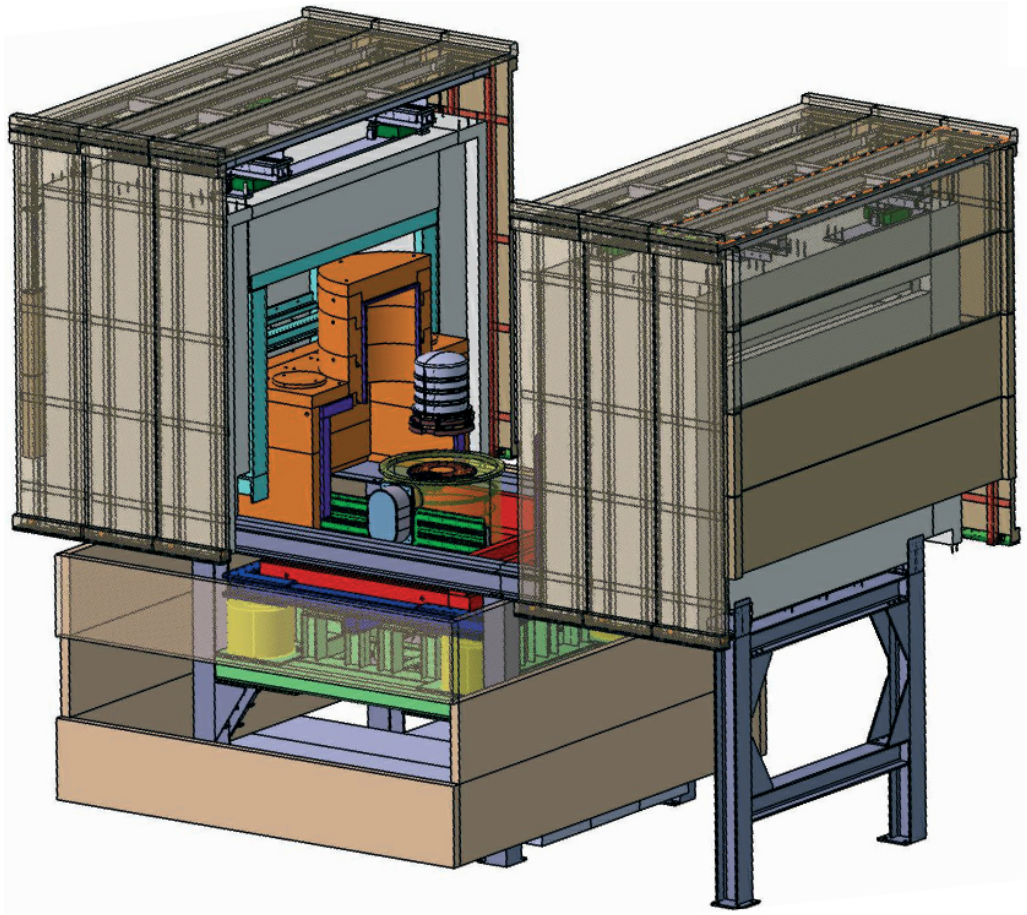

**Figure 2.7:** Schematic view of the passive shielding, the mechanical construction and the muon veto detector of EDELWEISS-II. To access the detectors in the cryostat (light grey), the lead (orange) and polyethylene (grey) shielding of Niveau 1 together with plastic scintillator modules of the muon veto system (brown) are mounted on movable waggons. See text for details.

glued to both ends of the modules with a 180° light bending at both ends of each module. A 10 *cm* long and 6 *cm* thick scintillator bar covering the whole width of the module is used as a light guide supported by highly reflective aluminium sheets at the end of the modules. The narrow sides of the bar as well as the light guide are at an angle of 12° and 7°, respectively, to the vertical axis. A schematic overview as well as a photograph taken at Forschungszentrum Karlsruhe before installation of a scintillator module is shown in figure 2.8. The modules have been used similarly as an muon veto counter in the KARMEN experiment [Arm02]. A complete description of the modules, measurements of the effective attenuation length and spectral quantum efficiency can be found in [Bod90; Rei98] and references therein. For the EDELWEISS-II setup a complete new mechanical construction for the scintillator modules according to the movable shielding concept

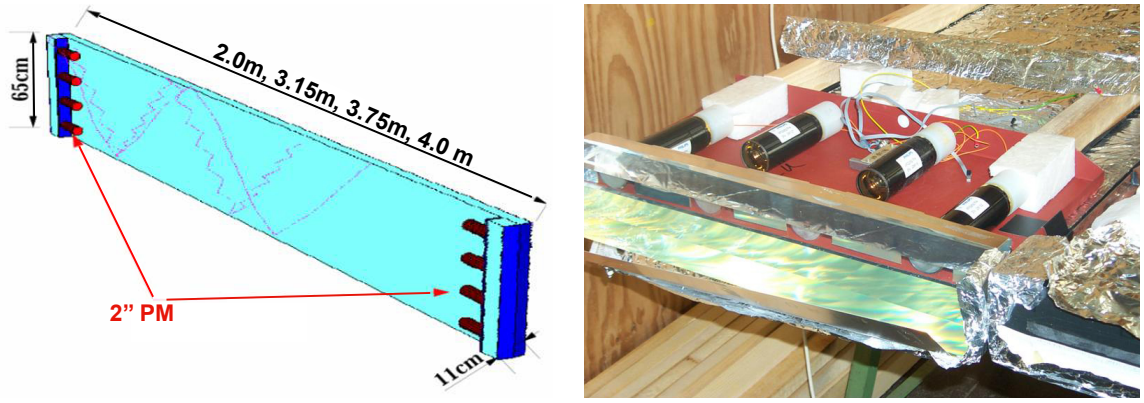


**Figure 2.8:** Plastic scintillator modules of the EDELWEISS-II muon veto system. *Left*: Schematic overview of a single module. *Right*: Photograph of the module end, the lightguide and the removed photomultipliers during packaging of the modules at Forschungszentrum Karlsruhe

has been developed. Furthermore the electronic readout and data acquisition has been adjusted to the new setup. Before the installation of the scintillator modules in the underground laboratory LSM, thorough tests of the modules within the new setup have been performed at Forschungszentrum Karlsruhe [Hab04].

Already since 2006 the muon detector system is taking data with stoppages during installation periods. The data acquisition of the veto system is completely autarkic and only a 10 $\mu s$ time stamp is shared with the data acquisition of the bolometer system. The veto data is stored unrestrictedly and offline rejection of bolometer events with veto activity will be performed [Chaon].

### 2.2.3 Detector Improvements

The main factor limiting the discrimination capabilities of the heat-ionisation Germanium detectors used in the EDELWEISS-I setup are near-electrode events, leading to incomplete charge collection, see also section 2.1.2. Within EDELWEISS-II a new generation of detectors are operated combining the two sensors for charge collection and temperature increase in one. This is achieved by an amorphous thin film, typically of $10-100$ $nm$ thickness, replacing the NTD-thermometer and the Aluminium electrodes on both sides of the Germanium crystal. The material used is $Nb_xSi_{1-x}$, where $x$ is the relative contribution of the elements and is typically around $x \sim 0.085$. The thin film electrodes are divided in a guard ring electrode and an interdigitised central part through 0.5 $mm$ spaced interleaved $Nb$ electrodes with 50 $\mu m$ digit width in a comb-like structure. One of the currently in EDELWEISS-II installed 400 $g$ Germanium detectors with $NbSi$ thin film sensors is shown in figure 2.9. With these detectors two heat channels and two ionisation channels are measured simultaneously. The great advantage of this technique is to reject near-surface events by comparison of the athermal phonon contributions by the two sensors. A parti-

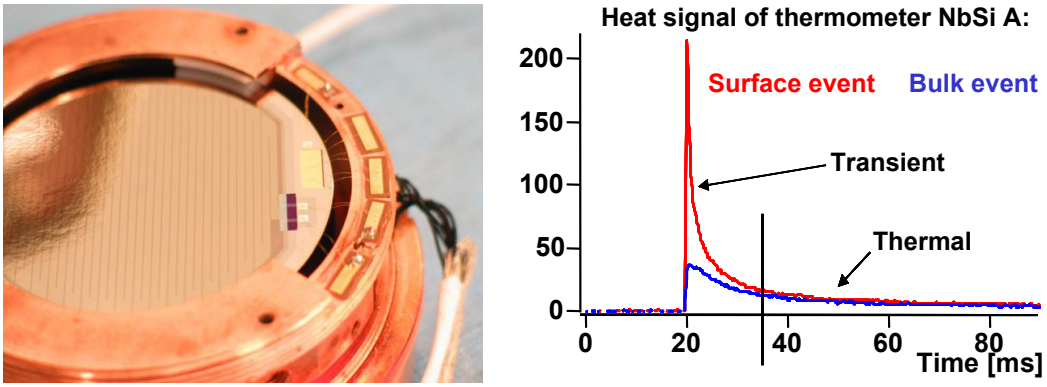


**Figure 2.9:** *Left*: Photograph of one of the 400 $g$ Germanium detectors with $NbSi$ thin film sensors as currently installed in the EDELWEISS-II experiment. *Right*: Heat signal as measured by one thermometer for two different event types (near-surface and bulk event).

cle interaction in the Germanium crystal will produce out-of-equilibrium phonons diffusing away from the impact zone. In the case of a near-surface event, a large amount of these high-energy phonons will be trapped by the nearby $NbSi$ layer and induce an athermal heat signal. This signal will be much larger than the one created by a bulk event of the same energy, while the thermal part related to the deposited energy does not change. Using pulse shape analysis of the two $NbSi$ thermometers allows effective identification of near-surface events [Mar04a; Jui06]. The measured phonon signals by the thermometer on one side of the crystal, here named NbSi $A$, for an interaction taking place near the thermometer (red line) and one in the bulk of the detector (black line) are illustrated in figure 2.9.
In addition to the new $NbSi$ athermal phonon detectors, further investigations point towards a potentially very promising method of surface event rejection with the ionisation signal. In this approach, the classical disk-shaped central Aluminium electrodes are replaced by interleaved concentric strips with typical width of 0.2 $mm$ in a distance of 2 $mm$. Guard electrodes and a neutron transmutation-doped (NTD) Germanium thermometer complete the device. The strips are alternately connected yielding to a set of four electrodes. Charge carriers produced by a particle interaction are drifted along the field lines towards the collection electrodes. Depending on the place of the energy deposition different event populations are then obtained in the electrodes. In principle, one can discriminate three different types of events: bulk events delivering signals on both sides of the crystal, near-surface events which deliver signals only on one side and a third type of events, obtained in specific areas of the detector, resulting in charge division between three measurement channels. A schematic side view of these crystals showing the different charge measurement channels is illustrated in figure 2.10. Also shown are the trajectories of charge carriers (blue and red, respectively) in the electrical field for the described event types [Bro06].

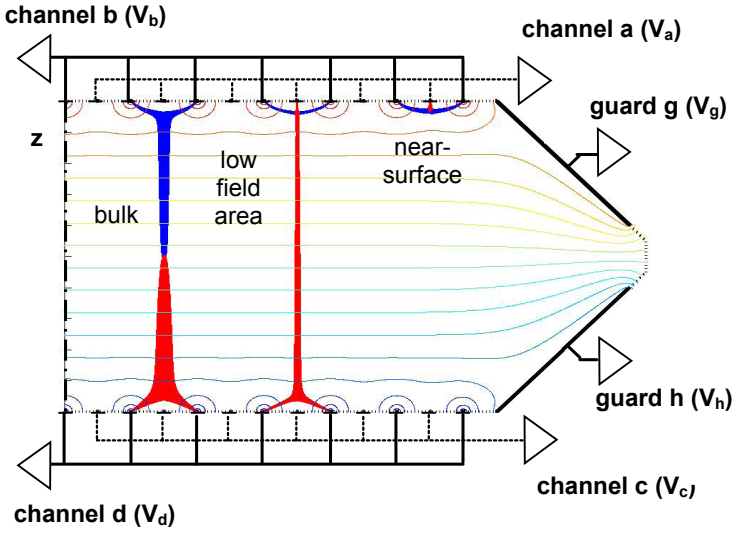


**Figure 2.10:** Schematic side view of Germanium crystals with interdigitised electrodes for surface event rejection using the ionisation signal. Shown are charge carrier trajectories for three representative events [Bro06]

### 2.2.4 Sensitivity goal

The goal of the EDELWEISS experiment is to directly detect Dark Matter by measuring nuclear recoils. In the second phase of the experiment the effective exposure time will be increased by a factor $\times 100$, while the background rate should not exceed the level of $\Gamma_{\mathrm{bg}} < 2 \times 10^{-3}\ kg^{-1} \cdot d^{-1}$ to reach the aimed sensitivity goal. This will be achieved, as described in the previous sections, by several modifications. Already installed in the underground laboratory LSM is a new cryostat able to house up to 120 detectors and the complete new shielding concept with an additional active muon veto detector. After several commissioning runs in 2006 and improvements on hardware components, data taking has started in 2007 with up to 28 ($\sim 9\ kg$) bolometers. Special focus is also set on the development of new detector techniques to improve the identification of background events (see section 2.2.3).

Within the second phase of the EDELWEISS experiment, significant parts of the supersymmetric parameter space for particle Dark Matter, e.g. the neutralino, will be observed. This can be illustrated by projecting the aimed sensitivity of the EDELWEISS-II experiment on the WIMP-nucleon cross-section depending on the WIMP masses, see figure 1.9 and 1.10 on an overview of current best limits and an outlook of ongoing and future Dark Matter search experiments.

# 3 Geant4 simulations of muons interacting with matter

In order to study simulations of the muon-induced neutron flux for the EDELWEISS-II experiment, the reliability of the used simulation code has to be checked. There are only very scarce experimental data available on muon-induced neutron measurements. This makes it very difficult or almost impossible to cross-check Monte Carlo simulations regarding this issue. In view of the lack of data and due to large quantities of feasible computer codes in the physics community and their ongoing development, comparing the different approaches in computation models and computer languages, as well as comparing variable program versions becomes essential. The simulation code `FLUKA`[Fer05; Fas03] is widely used in the field of underground physics for simulating both hadronic and electromagnetic interactions up to 20 $TeV$. Nevertheless, the use of `FLUKA` for the purpose of an experimental setup like the EDELWEISS experiment is not free of problems. In fact it does not treat individual nuclear recoils, e.g. by neutrons, on an event-by-event basis. Furthermore, the energy is conserved only on average, but not necessarily in single reactions which is especially important for Dark Matter experiments. Therefore one is obliged to use additionally for example the simulation code *MCNP* [Bri86] for neutron tracking inside the laboratory. The simulation code *Geant4* [Ago03; All06] however seems more expedient to study the correlation of high energy muons ($E_\mu > 200\ GeV$) in the surrounding rock with low energy neutron recoils ($E_{recoil} < 50\ MeV$) in the bolometers of the EDELWEISS experiment in an end-to-end simulation.

In this chapter, first some general remarks about the simulation package *Geant4* are made. Also, the physics list used in the *Geant4*-simulations will be introduced with special attention on the neutron production mechanisms. Thereafter the dependence of the neutron production yield on the muon energy, the individual production mechanisms and the different materials in the EDELWEISS-II experiment will be discussed and the angular and lateral distribution of neutrons induced by muons will be studied.

## 3.1 The simulation toolkit Geant4

*Geant4* is an object-oriented toolkit to simulate the passage of particles through matter written in the programming language `C++`. It offers a complete range of functionalities including the tracking of a large set of long-lived particles, the realisation of complex geometry designs and the usage of different physics models.

For the *Geant4* simulation toolkit, as the successor of the `Fortran`-based simulation code *Geant3* [Bru93], a major package of CERN software has been redesigned using an object-oriented philosophy. A large degree of functionality and flexibility is given in order to meet new requirements from a variety of different physics areas beside high-energy accelerator physics, e.g. heavy ion physics, cosmic ray physics, space science physics or medical applications. Having said that, on the other hand adding new features or eliminating programming bugs in *Geant3*, with its complex structure driven by historical reasons and the limitations of the `Fortran` programming language, became almost impossible. With the release of version *Geant4* `3.2` in 2001, the maintenance and support of *Geant3* was therefore discontinued.

The physics processes included in the simulation toolkit *Geant4*, e.g. electromagnetic, hadronic or optical processes, are covering a wide range of energies, starting for some models at 250 $eV$ and extending in some cases to the $PeV$ range. A detailed description of the physics implemented in the *Geant4* toolkit is given in the *Geant4 Physics Reference Manual* [GEA07a]. Within the toolkit, the application user has to code a mandatory class, called the 'physics list', to assign the appropriate processes to each particle. In principle, the mean free path of a particle in a certain material is determined by the cross sections of the implemented processes and in case of decaying particles by the lifetime. Each process is randomly chosen to occur according to the implemented models, depending on the type of particle, its energy, etc. After a process occurs, the probabilities are updated to observe proper distributions. Many processes implemented in the *Geant4* toolkit are both theoretically and experimentally well founded. The electromagnetic processes, e.g. bremsstrahlung, delta ray production, pair production, Compton scattering, photo-absorption and multiple scattering are, at least at intermediate energy ranges, well understood and cross sections are experimentally measured. At very low energies, below a few $keV$, modeling of these processes becomes increasingly complex, since atomic properties become important. For very high energies, above several hundred $GeV$, photo nuclear reactions and the production of hadrons has to be taken into account. In the area of nuclear and hadronic interactions, even though the cross sections are well known, the exact distribution of secondaries is not. Large datasets of nuclear properties are used to model nuclear de-excitation. Especially in this field, an increasingly large number of models attempt to produce respectable distributions able to match experiments. It is left to the application user to carefully choose the physics list accordingly. Though all models are subject to continuous validation by the *Geant4* collaboration, it is essential to test a user defined physics list to assess the accuracy of the simulation needed. Since very rare processes are studied in the simulations of this work, no restrictions to particles and physics processes due to computation speed are made. Furthermore, the most detailed descriptions of physics processes available within the toolkit are used. In the following section, the physics lists used in the simulations of this work and the underlying model concepts are described in more detail.

## 3.2 The Geant4 - physics list

*Geant4* offers a vast variety of different physics models, which the application user is advised to choose carefully according to his particular use-case. Within the physics list category all physics processes participating in the interactions of particles in matter are managed. The abstract interface for the physics in *Geant4* allows multiple implementations of physics models which can be selected by energy range, particle type or material. For the simulations of very high energy muons together with low energy nuclear recoils, the provided pre-compiled physics lists by the *Geant4* toolkit are not satisfying. Therefore in all simulations of this work the following individual set of physics models is used.

### 3.2.1 Electromagnetic interactions

Electromagnetic interactions are described by quantum electrodynamics (QED) and can be calculated using Feynman diagrams. In *Geant4* the properties for electron, positron, photon and hadron interactions are handled in a sub-category to the *Geant4* - physics list. The basic processes treated within this class are among others ionisation, bremsstrahlung, multiple scattering, Compton and Raleigh scattering, the photoelectric effect, annihilation, pair conversion, etc. In general, the energy loss processes for all charged particles are very similar. Therefore they are commonly described within the *Geant4* toolkit. Without loss of generality, the energy loss processes are described in more detail in the following only for muons.
The electromagnetic energy loss of a charged particle, e.g. a muon, is described in *Geant4* below a given energy threshold (also referred to production threshold, or depending on the material as energy range cut) as a continuous energy loss. Above this energy threshold, the explicit production of secondary particles according to the implemented physics processes is simulated (see also section 3.2.4). For an incident muon, four basic processes determine the energy loss and the production of secondary particles: ionisation (including the production of high-energy $\delta$-electrons), production of electron-positron pairs, bremsstrahlung and inelastic muon interaction with nuclei (also denoted deep inelastic scattering, or DIS). With the differential cross section for each process, the continuous part to the muon energy loss below threshold is calculated by:

$$\frac{dE}{dx} = -\int_0^{\epsilon_m} \epsilon \, \frac{d\sigma(E,\epsilon)}{d\epsilon} d\epsilon \tag{3.1}$$

where $d\sigma(E,\epsilon)/d\epsilon$ represents the differential cross section for energy $E$ and energy transfer $\epsilon$. The upper limit of the integral $\epsilon_m = min(T_{cut}, T_{max})$ is obtained by the production threshold $T_{cut}$ and the kinematical limit of a given process. This integration is equally done for ionisation, bremsstrahlung and $e^+e^-$-pair production and stored in a $dE/dx$ table for faster computation. The relative importance of a given process depends furthermore on the atomic number $Z$ of the material. The

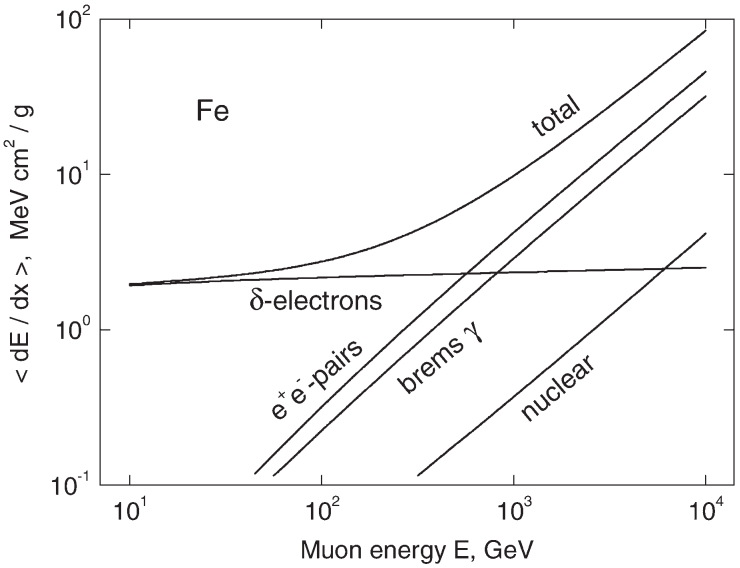


**Figure 3.1:** *Geant4* calculation of different contributions to the energy loss of muons in matter (*here*: iron)[Bog06]

calculation in *Geant4* of the different contributions to the total energy loss of the muon in matter exemplified by iron is illustrated in figure 3.1. One can see, that for relatively low energies ($E_\mu \lesssim 100\ GeV$) the main contribution to the muon energy loss is provided by ionisation. The other processes however become more important with higher muon energies. In first approximation (see Appendix A), the energy loss for muons can be written as:

$$\frac{dE_\mu}{dx} = a \ + \ b\ E_\mu \tag{3.2}$$

where $a$ is given by the mean energy loss of a minimal ionising particle and $b = b_{\text{brems}} + b_{\text{pair}} + b_{\text{DIS}}$ are the fractional energy loss of the radiation processes (see also chapter 4 for a more detailed discussion on muon energy loss).
However, if the energy transfer is above the production threshold, the energy loss is simulated in *Geant4* as a real discrete act of an interaction. The final state of the individual processes and the production of secondaries is sampled with Monte Carlo methods. The underlying physics concepts and the computational methods depend on the choice of the individual user from the physics lists provided by the *Geant4* toolkit.

In the simulations of this work, for all electromagnetic processes for incident photons and all charged particles, the 'standard' electromagnetic package provided by the *Geant4* toolkit is used. This includes for photons the photoelectric effect, Compton scattering and conversion into electron and muon pairs. Common to all charged particles is the description of ionisation including $\delta$-electron production with corrections made to the cross sections by energy variation and energy loss fluctuations in thick absorbers. Furthermore, scintillation and Cerenkov light emission, multiple scattering and ionising collisions by photoabsorption are included. Individual

classes for photon emission through bremsstrahlung exist for electrons and muons, since the cross section is dependent on the mass of the initial particle. Additionally, the so-called 'low energy' package was applied to all charged particles. This package provided by the low energy group of the *Geant4* collaboration extends the coverage of electromagnetic interactions of photons and electrons down to energies of 250 $eV$ and of protons, ions and antiprotons even down to energies around $\sim 1$ $keV$.

### 3.2.2 Muon nuclear interaction

The contribution of muon nuclear interaction to the combined cross section is always relatively small, as illustrated in figure 3.1. However it becomes important at high muon energies ($E_\mu > 10$ $GeV$). With relatively high energy transfers the average energy loss for this process increases almost linear with energy. For $TeV$ muon energies it constitutes about 10% of the total energy loss rate. Furthermore, this process leads to the production of nuclear showers and consequently contributes significantly to the hadron background of Dark Matter experiments. With the goal to study the muon-induced neutron yield in the EDELWEISS-II experiment, the initiatory interaction of the primary muon with a nucleus of the rock or the shielding materials of the experiment is important. As will be discussed in section 3.3.1, the contribution to the total neutron yield in muon showers by muon nuclear reactions is outnumbered by photo nuclear reactions by a factor of $\sim 3$, but the compatibility of the two processes in terms of secondary production is obvious, as will be outlined in the following.
The muon nuclear interaction is usually described in terms of nuclear absorption of virtual photons and is thus often called 'photo nuclear muon' interaction. The Feynman graph of the reaction is shown in figure 3.2. This method of equivalent photons, also called Weizsäcker-Williams approximation, was first published 1934 [Wei34; Wil35] and continuously enhanced [Dal57; Bor75; Bez81]. In the case of a large four-momentum transfer from the muon to the nuclei, e.g. $\sqrt{q^2} \gg 1$ $GeV$, the process is also called muon deep inelastic scattering ($\mu$-DIS).
By this substitution, one can show (see Appendix A) that the muon nuclear cross section depends on the real photo nuclear cross section:

$$\left(\frac{d\sigma}{d\nu}\right)_{\text{DIS}} = \Psi(\sigma_{\gamma N}, \nu)\Phi(E, v) \tag{3.3}$$

where $\nu$ is the energy lost by the muon, $v = \nu/E_\mu$ is the fractional energy loss of the muon and $\sigma_{\gamma N}$ is the interaction cross section of real photons with nucleons. The explicit form of the functions $\Psi$ and $\Phi$ is given in the Appendix A.
The model requires not only knowledge of the photo nuclear cross section, but must also account for the different nuclear reaction mechanisms involved in the initial photo nuclear excitation process and the subsequent decay of the excited nucleus by particle and gamma-ray emission. One can distinguish five main regions according to the energy transfer to the nucleus, i.e. the energy of the virtual photon. At low energies, below about 30 $MeV$, the Giant Dipole Resonance (GDR) is the dominant excitation mechanism, where a collective bulk oscillation of the neutrons

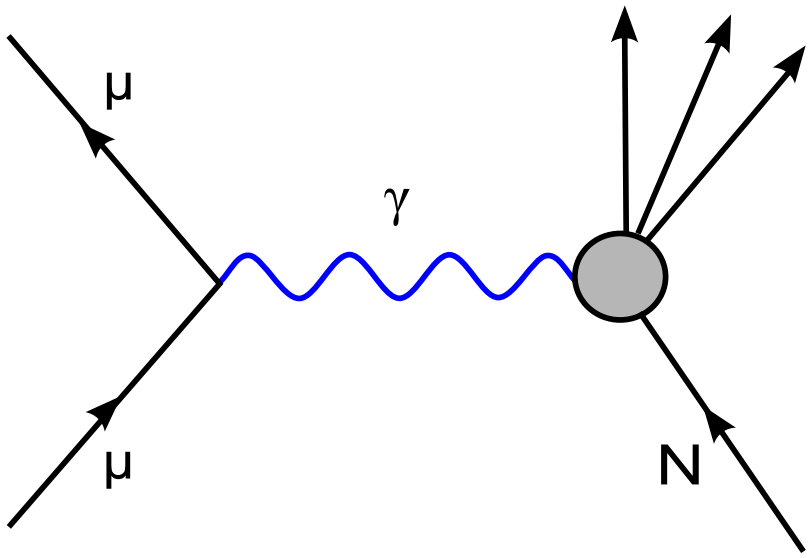


**Figure 3.2:** Feynman graph for the photo nuclear muon interaction.

against the protons of the nucleus occurs. At higher energies up to approximately 150 $MeV$, where the wavelength of the photon decreases, the phenomenological model of photoabsorption on a proton-neutron pair (quasi-deuteron), which has a large dipole moment, becomes important. The dominant feature of the photon interaction above the $\pi$-threshold (140 $MeV < E_\gamma < 500\ MeV$) is the $\Delta$-resonance [Bia96]. At this, the spin of a single nucleon is increased to 3/2 by the absorption of the virtual photon. Above approximately 500 $MeV$ up to 1.2 $GeV$ the excitation mechanism are predominantly $N^*$-resonances (e.g. Roper-resonance [Rop64]). Above this energy region, e.g. the energy of the virtual photon exceeds 1.2 $GeV$, experimental measurements observe a slow rising of the photo nuclear cross section. This rise is well described by assuming a logarithmic dependence of the photo nuclear cross section for high energies, which is an accurate average over further resonance bumps (e.g. Reggeons [Col77]).
The implementation of the photo nuclear cross section in *Geant4* covers all incident photon energies from the hadron production cut upward. For the discussed five energy regions, a set of parametrised functions are fitted to the *Geant4* photo nuclear data base, consisting of measured photo nuclear cross sections of about 50 different nuclei. A schematic overview of the photo nuclear cross section spanning over the discussed energy regions is illustrated in figure 3.3.

In the *Geant4* physics list used in this work, muon-induced spallation or muon nuclear interaction is modelled above 3 $GeV$ muon energy. For lower muon energies, on the one hand the contribution to the energy loss by nuclear muon interactions as shown in figure 3.1 is very low. On the other hand, lower muon energies are not sufficient to generate final states with secondary particles well beyond the standard particle production threshold. Since the interaction of the muon with the nucleus is described by the exchange of a virtual photon, the hadronic photon interaction

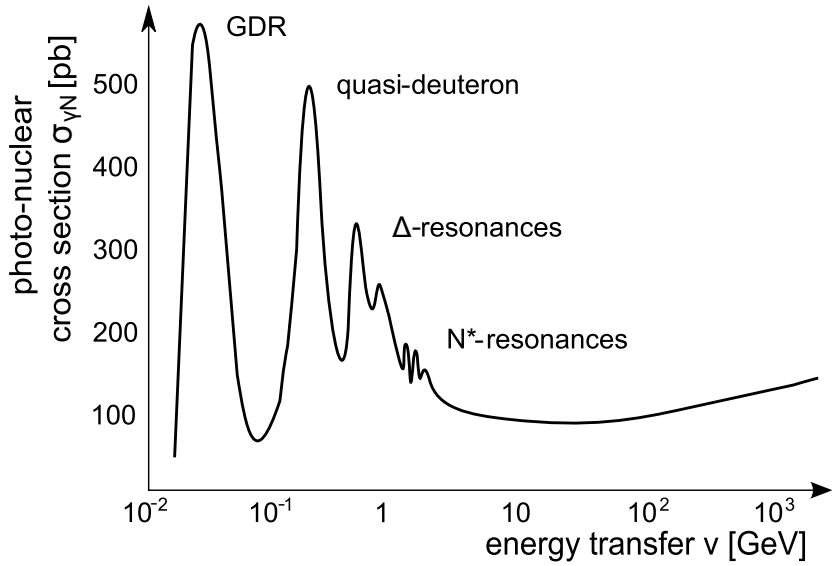


**Figure 3.3:** Schematic photo nuclear cross section $\sigma_{\gamma N}$ in $pb$ as a function of the photon energy $\nu$ in $GeV$. In *Geant4* parameterisations are fitted to data for about 50 individual nuclei.

produces secondaries according to the intra-nuclear cascade model used. A chiral invariant phase space decay model, a non-pertubative three-dimensional parton model parametrised to fit experimental data on many different nuclei, generates the fragmentation below 3 $GeV$ photon energy. A lower threshold of 200 $MeV$ is observed. Though this lower boundary is well above the standard production thresholds, the energy distribution of the final state particles would not contribute significantly to the electromagnetic and hadronic shower development. However, the total number of secondaries produced in muon nuclear reactions is maintained in *Geant4*. For instance, this is the case for neutrons; the energy below the lower threshold is not sufficient for pion production. At higher energies of the photon a theoretical quark-gluon-string parton model, i.e. in *Geant4* the `G4QGSModel`, simulates the final-state fragmentation. Each hadron-nucleon interaction is assumed to be mediated by the exchange of one or more Pomerons [Kai84]. The result of the interaction is one or several excited strings and a nucleus in an excited state. The fragmentation of the excited strings into hadrons is handled by a string fragmentation model. The interaction of secondaries with the excited nucleus is described by a cascade model. The results of *Geant4* simulations for the final state particles, with respect to the energy and angular distribution, are discussed in section 3.3.

### 3.2.3 Hadronic interactions

Given the increasingly large number of available models for hadronic interactions, the models used, especially the energy ranges therein, have a direct effect on the results of the simulations. Possible discrepancies between older *Geant4* versions or

| | | | | | | |
|---|---|---|---|---|---|---|
| neutrons | G4NeutronHP | 250 $keV$ | $<$ | E | $<$ | 19.9 $MeV$ |
| | G4PreCompound | 19.5 $MeV$ | $<$ | E | $<$ | 70 $MeV$ |
| | G4BinaryCascade | 65 $MeV$ | $<$ | E | $<$ | 6.1 $GeV$ |
| | G4LENeutron | 6 $GeV$ | $<$ | E | $<$ | 12.1 $GeV$ |
| | G4QGSModel | 12 $GeV$ | $<$ | E | $<$ | 100 $TeV$ |
| protons | G4PreCompound | 250 $keV$ | $<$ | E | $<$ | 70 $MeV$ |
| | G4BinaryCascade | 65 $MeV$ | $<$ | E | $<$ | 6.1 $GeV$ |
| | G4LEProton | 6 $GeV$ | $<$ | E | $<$ | 12.1 $GeV$ |
| | G4QGSModel | 12 $GeV$ | $<$ | E | $<$ | 100 $TeV$ |
| $\pi$/K/ion | G4BinaryCascade | 250 $keV$ | $<$ | E | $<$ | 1.5 $GeV$ |
| | G4LE-packages | 1.4 $GeV$ | $<$ | E | $<$ | 12.1 $GeV$ |
| | G4QGSModel | 12 $GeV$ | $<$ | E | $<$ | 100 $TeV$ |

**Table 3.1:** *Geant4* physics models for inelastic processes for hadrons as used in the simulations of this work. The overlap at the energy boundaries is demanded by the software. For neutron scattering and absorption cross-section data the `G4NDL3.9` library was used.

simulations done by other groups are mainly ascribed to slight deviations in the hadronic physics lists and the energy ranges therein, besides apparent new features and eliminated programming bugs.

The elastic hadronic scattering processes, e.g. hadron-nucleus collisions, are modelled by the 'low energy' expansion package analogous to the electromagnetic processes. For inelastic hadronic interactions, in the other hand, the situation is not as simple. Here, a set of models is used in various energy ranges for different hadronic particles. These models try to produce respectable distributions of the secondary spectra either by parametrisation to data on nuclear properties or by theoretical assumptions. For example, at very high energies above 12 $GeV$ the inelastic interactions for neutrons, protons and pions, as well as for deuterium, triton, $\alpha$-particles and all generic ions are modelled using the quark-gluon-string parton model (`G4QGSModel`); the same as already used for high energy photo nuclear reactions. The intermediate energy range between $6-12$ $GeV$ for protons and neutrons, and between $1.4-12$ $GeV$ for other particles, is simulated by the 'low energy' (`G4LE`) packages. In these parametrised models, the incident particle collides with a nucleon inside the nucleus and the final state of this interaction consists of a recoil nucleon, the scattered incident particle, and potentially many hadronic secondaries. All of these particles are able to re-interact within the nucleus, thus developing an intra-nuclear cascade. If the energy of the projectile is below $\leq 6$ $GeV$, these intra-nuclear cascades are modelled using the so-called kinematical model *Binary Cascade* (`G4BinaryCascade`). The interactions herein are described by collisions between the primary or secondary particle and an individual nucleon of the target nucleus, therefore the term binary. For the collisions, experimental cross sections are used whenever available. The intra-nuclear cascade terminates when the average and maximum energy of the secondaries are below threshold. The remaining fragment is

| material (range cut $r_c$) | $\gamma$ 10 $cm$ | $e^-$ 1.25 $mm$ | $e^+$ 1.25 $mm$ |
|---|---|---|---|
| $C_nH_{2n}$ | 14.769 $keV$ | 364.659 $keV$ | 355.79 $keV$ |
| polyethylene | 16.781 $keV$ | 402.4 $keV$ | 392.614 $keV$ |
| PVT[1] | 18.865 $keV$ | 412.431 $keV$ | 402.4 $keV$ |
| Fréjus rock | 85.493 $keV$ | 744.691 $keV$ | 708.91 $keV$ |
| Fréjus concrete | 83.197 $keV$ | 658.435 $keV$ | 634.561 $keV$ |
| Germanium | 389.855 $keV$ | 1.038 $MeV$ | 976.329 $keV$ |
| Copper | 849.99 $keV$ | 1.72 $MeV$ | 1.598 $MeV$ |
| Iron | 626.02 $keV$ | 1.559 $MeV$ | 1.484 $MeV$ |
| Lead | 2.249 $MeV$ | 1.678 $MeV$ | 1.559 $MeV$ |

**Table 3.2:** Production thresholds in energy for gammas, electrons and positrons for the materials used

then treated by a *pre-compound* (`G4PreCompound`) deexcitation model for neutrons and protons with energies below 70 $MeV$. This model offers a smooth transition between the kinetic stage of the reaction to the equilibrium stage by de-excitation models, which consider fragmentation, fission, gamma evaporation, Fermi break-up and multi-fragmentation. Furthermore, the transport and interactions of neutrons of energies below $\sim 20$ $MeV$ is simulated with the use of the data-driven *High Precision* (`G4NeutronHP`) model together with the *Geant4* neutron data library version `G4NDL3.9`. An overview of the models for inelastic hadronic processes used in the simulations of this work is shown in Table 3.1. This particular choice of physics models and the energy ranges within is chosen, based on the pre-compiled physics list `QGSP_BIC_HP`, with the objective of highest accuracy regardless of computation speed. For this, the physics lists provided by the *Geant4* toolkit are not satisfactory and are altered in the described way in close collaboration with developers from the *Geant4* collaboration [Wel06].

### 3.2.4 Geant4 particle production cuts

The simulation toolkit *Geant4* requires a particle production threshold (*energy cut*) for gammas, electrons and positrons only, below which no secondary particle will be generated to avoid any infrared divergence. For example, the differential cross section of $\delta$-electron productions and bremsstrahlung grow rapidly for decreasing energies of the secondary particles. To ensure reasonable computation speed traditionally cuts are used to track not all secondary particles. Specific to *Geant4* is that the value of cut is given in terms of distance $r_c$ (*range cut-off*). This definition in range, rather than in energy, results from a more natural concept for the requirement for precision of spatial radioactive dose deposition. Besides, this conception is more strict, provides less handles for user modifications and thus ensures transferable val-

[1]PVT = polyvinyltoluene, a plastic scintillator material the muon veto modules are made out of, see also chapter 2.2.2 for details.

idation between different geometries [GEA07b]. It remains to the user, to provide these production thresholds in distance which will then be internally converted into energy for the material the particle traverses. In this work the overall production cut for gammas is set to $r_c = 10\ cm$, while the ones for electrons and positrons is set to $r_c = 1.25\ mm$. In Table 3.2 the corresponding energy cuts for the various materials used in the simulations are calculated.

## 3.3 Neutron yield for varying muon energies

Comparing the results of different computation approaches with experimental data is essential to assess the precision of the simulations. In this section, the dependence of the neutron production mechanisms on the incident muon energy is studied. A commonly used approximation is made to compare muon-induced neutron production with experimental data. Since the muon energy is generally not simultaneously measured, the neutrons are assumed to be produced by mono energetic muons. The energy of the muons thereby corresponds to the mean muon energy at the depth of the underground laboratory [Agl98; Kha95; Wan01], see chapter 4 for details about the energy distribution of muons underground.

Neutrons are produced by muons either directly in muon photo nuclear reactions or by the electromagnetic and hadronic shower induced by the muon. In an inelastic scattering of a muon with high energy transfer, not only neutrons, but a multiple of hadrons, e.g. $\pi^{\pm}$, $K^{\pm}$, $p$, $\alpha$, etc. are produced. Following this reaction, a hadronic shower develops. According to the energies of the secondary particles, further nuclear reactions can occur producing more neutrons or hadrons. An additional neutron production mechanism is the capture of a low energy $\pi^-$ by a nucleus. On the other hand, in the electromagnetic shower, neutrons and other hadrons are mainly produced by real photo nuclear reactions. In the performed *Geant4* simulations, the physics models for electromagnetic and hadronic interactions are carefully chosen as described in the previous section. An incident $\mu^-$ beam of fixed energies between 10 $GeV$ and 1 $TeV$ is studied passing perpendicular through a wide block of target material with a column density of $X = \rho \cdot x = 4000\ g/cm^2$, where $\rho$ is the density of the material and $x$ is the vertical width. To account for the full lateral neutron production the material has comparable transverse size ($Y = Z = 1000\ g/cm^2$). The material studied is a generic hydrocarbon with the chemical composition $C_nH_{2n}$ and a density of $\rho = 0.8\ g/cm^3$. This abstract material represents well commonly used neutron shielding materials, e.g. polyethylene as well as organic scintillators for which experimental data is available. The neutron production yield is typically written as neutrons per muon and unit path length ($n/\mu/(g/cm^2)$). The *Geant4* neutron production yield for different energies in $C_nH_{2n}$ is shown in figure 3.4.
The neutron production yield along the muon track is determined by considering several effects. The muon-induced cascade requires a certain length of material to develop, hence the neutron yield first increases along the muon track before it reaches equilibrium, see figure 3.5(a). Due to this, neutrons produced in the first

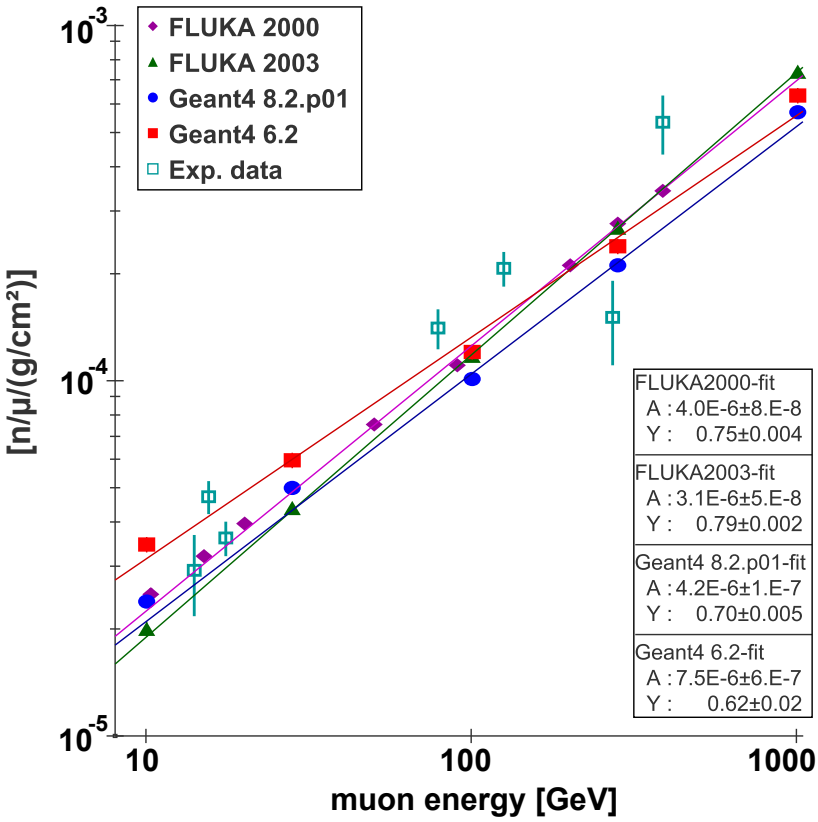


**Figure 3.4:** Neutron yield per unit muon track as a function of muon energies for *Geant4* `8.2.p01` (blue circles), *Geant4* `6.2` (red squares), `FLUKA2003` (green triangles) [Ara05] and `FLUKA2000`[Kud03] (purple diamonds). The lines represent power-law fits. The experimental data (turquoise boxes) are measurements at different underground laboratories with depths between 20 *mwe* and 5200 *mwe*. See text for details.

fifth of the material, i.e. $X < 800\ g/cm^2$, are not considered to determine the neutron production yield per unit muon track (see figure 3.5(b)). Furthermore, the muon looses energy by passing through the block of material. Though this energy loss is negligible for energies above $E_\mu \geq 100\ GeV$, the neutron yield significantly varies along the length of the material for lower muon energies, as can be seen in figure 3.5(c). To compensate the energy loss in the first part of the material, the initial muon energy is slightly increased by $\Delta E \approx 2.5\ GeV$. However, for muon energies below $E_\mu < 100\ GeV$, the neutron production yield is determined only for a thinner slab of material, as indicated in figure 3.5(d), and then extrapolated to the full block of material.

In the simulation code *Geant4*, one has to avoid double counting of inelastically scattered neutrons, because unlike the common interpretation of a scattering neutron, the final state neutrons from inelastic processes have no memory to the

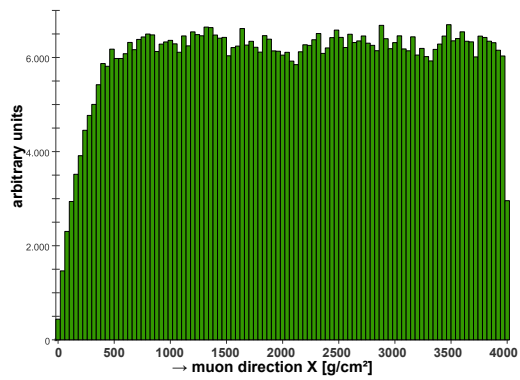


(a) $E_\mu = 280\ GeV$

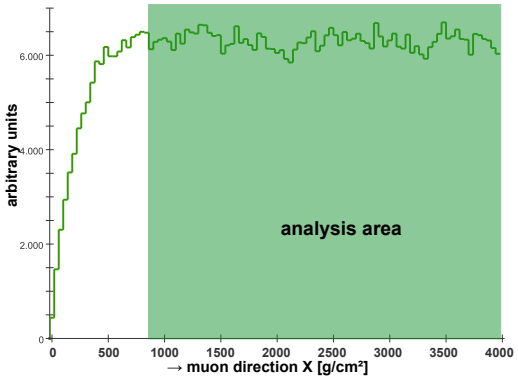


(b) Analysis area for $E_\mu = 280\ GeV$

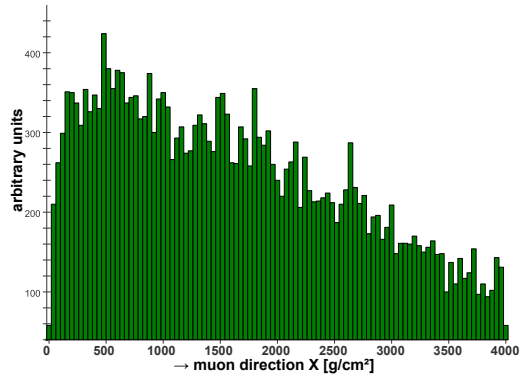


(c) $E_\mu = 10\ GeV$

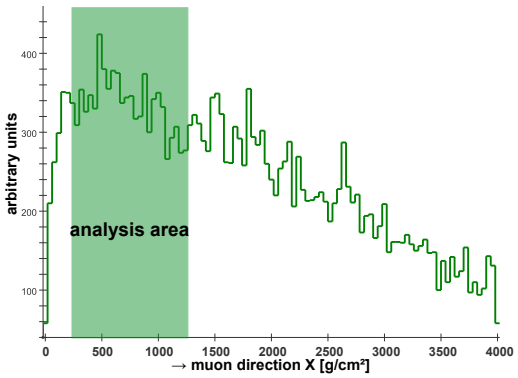


(d) Analysis area for $E_\mu = 10\ GeV$

**Figure 3.5:** The neutron production along the muon shower axis in $g/cm^2$ exemplary for muon energy $E_\mu = 280\ GeV$ ((a))and $E_\mu = 10\ GeV$ ((c)), respectively. The shaded areas in (b) and (d) represent the analysis area to determine the neutron production yield per muon and unit track length shown in figure 3.4. See text for details.

incident one. Therefore one has to assign one of the secondary neutrons produced in the process as the initial particle causing the reaction. In this work generally the highest energy secondary neutron is considered as the incident one and therefore not counted. This assertion does not always hold, since the scattered incident neutron may have less energy than any secondary neutron produced by the interaction. However this will only effect the neutron production spectrum discussed in section 3.5 and not the neutron multiplicity and hence the total yield [Ara05].

As expected and shown in figure 3.4, the number of neutrons produced by muons increases with muon energy. This can be explained by the increasing cross section for nuclear reactions with muon energies, as well as by the increasing energy transfer in these reactions. The neutron production of *Geant4* version `8.2.p01` can be approximated by the simple power law:

$$N_n(E_\mu) \propto (E_\mu)^\gamma \tag{3.4}$$

with a power index of $\gamma = 0.70 \pm 0.01$. Also represented in figure 3.4 are the results by a precedent *Geant4* version `6.2` with a power law approximation with $\gamma = 0.62 \pm 0.02$. Similar results on the power index ($\gamma \approx 0.75 - 0.79$) can be achieved using different versions of the simulation code `FLUKA` as reported in [Ara05; Kud03]. The experimental data in figure 3.4 corresponds to the mean muon energy at the respective experiment's depth: 20 *mwe* [Her95], 25 *mwe* [Bez73], 32 *mwe* by the Palo Verde experiment [Boe00], 316 *mwe* [Bez73], 570 *mwe* [Eni87], 3000 *mwe* by the LVD experiment in the Gran Sasso laboratory [Agl99] and 5200 *mwe* by the LSD experiment at Mont Blanc underground laboratory [Agl89]. The absolute values of the neutron yield per unit muon track is not perfectly reproduced by the two simulation codes `FLUKA` and *Geant4*. This could be due to a difference in the total interaction cross sections, in the neutron production cross sections or in the final-state multiplicity of secondary particles. However, given the spread of the shown experimental data, the results by the different simulation approaches are consistent with the experiments. Hereby one also has to consider the problem of assigning the mean muon energy to an underground laboratory as discussed in chapter 4 and the general limitation of comparability of the data with these benchmark simulations. The generally lower neutron yields by $\sim$ 20% for *Geant4* version `8.2.p01` are neither of statistical nature nor due to geometry effects. They can be accounted on the one hand to the release dependent modifications in the electromagnetic and hadronic shower development and the accompanying extensions in the nuclear cross section database. On the other hand slight deviations in the *Geant4* physics lists and the use of the 'low energy' package in this work could also contribute to the observed discrepancies.

As a summary, the rates of neutrons induced by muons can be assessed by simulations within a precision of a factor 2, which is reasonably accurate to deduce estimates of neutron rates in a specific underground geometry configuration.

### 3.3.1 Neutron yield by individual physics processes

Despite the importance of the muon inelastic scattering process for the neutron production, neutrons are also produced in secondary reactions in the electromagnetic and hadronic cascade induced by the muon. Moreover, it can be shown that secondary neutrons produced in the cascade outnumber the ones from muon nuclear reactions. The most important secondary reaction is the real photo nuclear interaction, followed by the neutron inelastic scattering process and inelastic processes of pions. Very few neutrons are produced in electron nuclear reactions or proton and light ion inelastic scatterings. The relative contributions of the most important mechanisms to the total neutron production for different muon energies are shown in figure 3.6. It is clearly seen that the neutron production for all muon energies is dominated by photo nuclear interactions in the electromagnetic cascade ($\sim 40 - 50\%$). The relative contribution by direct muon interactions decreases with

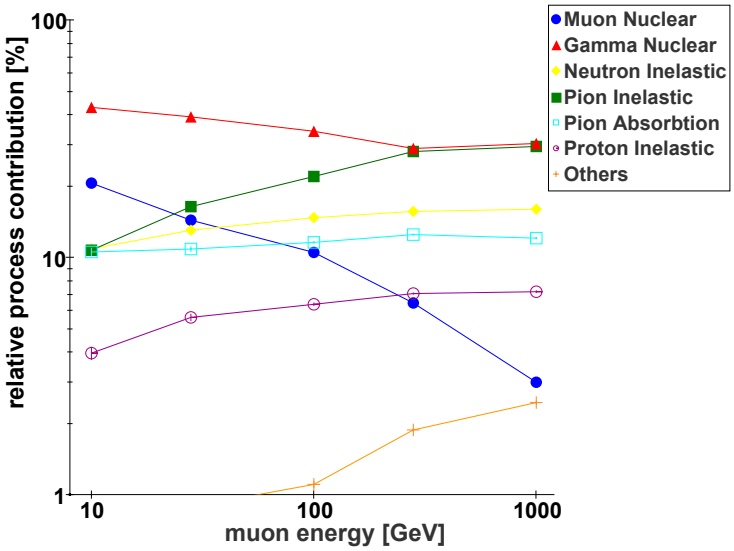


**Figure 3.6:** Relative contribution of individual processes to the total neutron production yield as a function on the muon energy in $C_nH_{2n}$.

higher muon energies since more and more energy of the shower is transferred to the electromagnetic and hadronic cascade. In consequence, all other process contributions are increasing relative to the total neutron production per muon, as can be seen in figure 3.6. These processes are namely the neutron inelastic scattering $(n - N)$, pion absorption at rest $(\pi^+ - abs)$, pion and proton inelastic scattering $(\pi - N,\ p - N)$ and very rare processes like electron nuclear scattering, kaon interactions and processes involving light fragments, e.g. $^2H$,$^3H$,$^3He$, summed up in figure 3.6 and not exceeding 3% relative contribution to the total neutron yield.
In summary it can be said, that the contribution to the total neutron production yield by muon nuclear reactions for all muon energies in the range of $10 - 1000\ GeV$ is less than 20%. With increasing muon energy, thus with increasing depth of the underground laboratories, neutrons are dominantly produced in the electromagnetic and hadronic cascade. This has to be considered in studying the total neutron production in an underground laboratory, since in the simulation the immediate rock overburden has to be sufficient for the cascade to develop, see chapter 5.

## 3.4 Neutron yield in various materials

As shown in the previous section, the neutron production induced by muons is dependent on the muon energy in a generic hydrocarbon material. In the experiment EDELWEISS-II the shielding material is not only made of polyethylene or plastic scintillator. Therefore the neutron production is also studied in other materials.
In these simulations the same geometrical situation, as described in section 3.3, is used, but with a fixed muon energy of $E_\mu = 280\ GeV$. The materials, sorted by atomic weight, are: the already discussed generic hydrocarbon $(C_nH_{2n})$, water for

| material | density $[g/cm^3]$ | components | atomic weight |
|---|---|---|---|
| hydrocarbon | 0.8 | 2 | 10.4 |
| water | 1.0 | 2 | 14.3 |
| rock | 2.74 | 10 | 24.4 |
| | 2.74 | 10 | 25.2 |
| | 2.65 | 13 | 31.4 |
| concrete | 2.4 | 7 | 30.6 |
| iron | 7.87 | - | 55.9 |
| copper | 8.96 | - | 63.6 |
| Germanium | 5.31 | - | 72.6 |
| lead | 11.36 | - | 207.2 |

**Table 3.3:** Materials used in *Geant4* simulations with density, number of components in composite materials and their mean atomic weight.

comparison reasons only, different compositions of rock, the concrete covering the laboratory walls, Iron from parts of the mechanical construction, Copper used for the cryostat, Germanium for the bolometers and finally Lead. The implemented physical properties of these materials are summarised in table 3.3 and the detailed composition of the materials, as implemented and used in all *Geant4* simulations of this work, are given in Appendix B.
The results for the various materials, together with results from *Geant4* simulations published in [Ara05] and results from similar `FLUKA` simulations [Wul03; Kud03], are shown in figure 3.7. The statistical uncertainties for all data points are comparable to the size of the data markers and are much smaller than the discrepancies between corresponding data points of different simulation codes. As can be seen, the neutron production generally increases with the average atomic weight of the material. Without any precise theoretical parametrisation, the dependence can be fitted with a simple power law:

$$N_n(A) \propto A^{\gamma} \tag{3.5}$$

where $A$ is the mean atomic weight and the power index is given by $\gamma = 0.99 \pm 0.01$ for the *Geant4* version `8.1.p01`. *Geant4* version `6.2` and `FLUKA` simulations yield to corresponding values for the power index between $\gamma = 0.76 - 1.01$.
All simulation codes predict neutron yields with no greater difference than a factor 2 for most of the materials, e.g. the generic hydrocarbon ($C_nH_{2n}$), copper or lead with `FLUKA` generally predicting higher values. Larger discrepancies are obtained for neutron production in composite materials, e.g. the different rock compositions or the particular concrete in the underground laboratories. Given the multitude of elements rock and concrete are composed of, deviations smaller than a factor of 3 are still acceptable.

The results of neutron production per muon for different materials can also be compared with experimental data, as done in [Kud03]. However, comparing

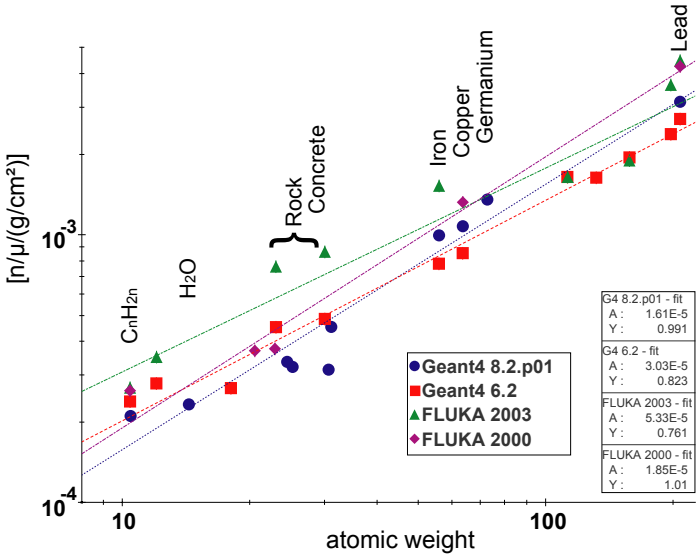


**Figure 3.7:** Neutron production yield depending on the mean atomic weight of the material. The compositions of the materials and their physical properties are given in table 3.3 and in Appendix B. Results for `FLUKA` and *Geant4* `6.2` simulations are taken from [Ara05; Wul03; Kud03].

simulations to experimental results is rather difficult. Without modeling the complex set-ups and having knowledge about the neutron detection efficiencies, a comparison can not be done straightforwardly. Most of the experimental data available is measured using thin targets, where no hadronic cascade can develop and the neutron production is measured for the first muon interaction only. Neutrons are furthermore measured under certain scattering angles only, thus a normalisation is required before comparison.

In conclusion, the differences between experimental data and the simulation codes `FLUKA` and *Geant4* are typically smaller than a factor of 2. Given the problems in comparing to experimental data and the uncertainties in the simulation code, this is an acceptable agreement. The differences between *Geant4* versions `6.2` and `8.2.p01`, respectively, can be attributed again to variations in the *Geant4* physics lists or version depending computation code. The deviations are however well below the model uncertainties. Despite improving physical models and computational code further efforts are obviously necessary to measure the neutron production of muons in underground laboratories. For example, a dedicated neutron detector is currently developed at University Karlsruhe (TH) and Forschungszentrum Karlsruhe to measure the neutron flux in coincidence with the muon veto detector system of the EDELWEISS-II experiment [Kluon].

## 3.5 Kinetic energy spectrum of $\mu$-induced neutrons

With the goal of tracking neutrons within the complete EDELWEISS-II geometrical setup, not only the total number of neutrons is important but also the kinetic energy distribution. Low energy neutrons, typically produced in electromagnetic interactions, quickly lose energy in elastic scattering reactions in hydrogen-rich material. Therefore the majority of neutrons produced in the surrounding rock or the shielding material are absorbed before entering the Germanium bolometers. However, especially in high energy muon nuclear reactions with a large energy transfer, neutrons with energies up to several $GeV$ can be produced. These neutrons can penetrate the shielding material, interact with the Germanium nuclei of the EDELWEISS-II detectors and transfer energy to the recoiling nucleus above threshold. Hence the kinetic energy spectrum of the neutrons produced in muon-induced showers is of great importance to the simulations. Figure 3.8 shows the kinetic energy spectrum of neutrons at the production vertices in $C_nH_{2n}$. In general, studying the neutron energy spectra for different muon energies, one can conclude that despite the total muon yield, see section 3.3, the shape and slope of the neutron spectra are independent of the incident muon energy. As a result, the mean neutron energies increase only slightly with increasing muon energies. The incident muons in figure 3.8 have an energy of $E_\mu = 280\ GeV$ and the block geometry and the neutron selection rules as described in section 3.3 are used.

The experimental data in figure 3.8 shows the average neutron spectrum measured by the LVD experiment in the Gran Sasso underground laboratory [Agl99]. The mean muon energy, as reported, is $\left\langle E_\mu^{GS} \right\rangle = 270 \pm 18\ GeV$ [Amb03] and thus suitable to be compared with the simulated data for $E_\mu = 280\ GeV$. However, the LVD dataset are normalised to the *Geant4* simulation data, since the experimental data does not represent the neutron energy spectrum at the production vertices, but a volume-averaged spectrum instead.

Also shown in figure 3.8 are the neutron kinetic energy spectra for the different production processes, e.g. neutrons produced by muon nuclear (green) or photo nuclear interactions (red), by neutron (yellow), pion (blue) or proton inelastic scatterings (purple) or by other interactions (orange) involving amongst other light fragments or ions. The energy spectrum of neutrons produced by pion absorption at rest (cyan) shows a distinct feature around kinetic energies of neutrons around $E_n \approx 80\ MeV$ with an, as expected, steep cut-off just below the pion rest mass subtracted by the nucleon binding energy.

In the parametrised hadronic models of *Geant4*, the final state hadronic vertex of nuclear reactions, e.g. muon nuclear or photo nuclear interactions, in terms of secondary particle production is subject to Monte Carlo methods. At this, it can occasionally occur that a fraction of the secondary particles deplete the available energy and momentum of the interaction. However, to account for the total neutron production yield, given by [Bor75], the simulation models insert further secondary particles with kinetic energy $E = 1\ keV$. This energy is in general well below the average kinetic energy of the secondaries to allow the user to identify these particles

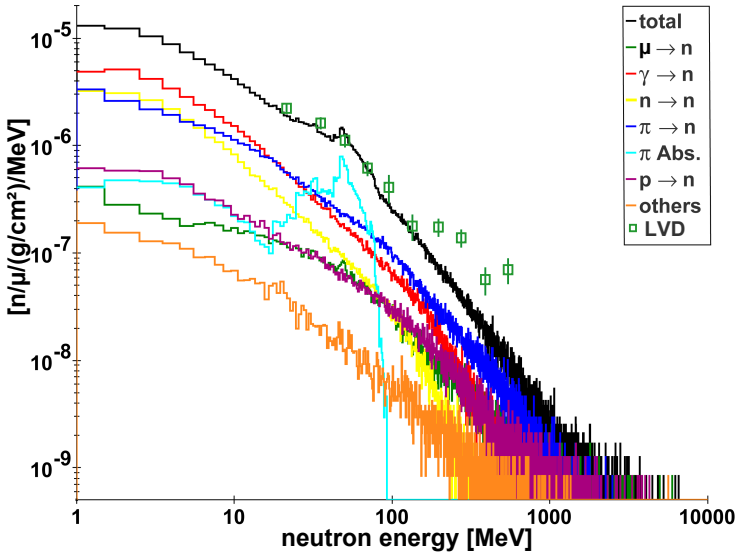


**Figure 3.8:** Kinetic energy distribution of neutrons at the production vertices (black). The muon energy is $E_\mu = 280\ GeV$, the material is $C_nH_{2n}$. Also shown are the contribution by individual neutron production processes, see also 3.3.1.

as simulation artefacts and to identify any unfeasible model selection [Wel06]. In the above described simulations, the percentage of neutrons in muon nuclear interactions with $E_n = 1\ keV$ does not exceed 10% for any muon energy or any material. Together with the results of section 3.3.1 this results in less than 1% of neutrons with this energy in muon-induced showers (with comparible values for other secondary particles). Thus one can conclude that the occurrence of these simulation artifacts does not disqualify the selected choice of physics models for the investigated use-case.

## 3.6 Angular distribution of $\mu$-induced neutrons

Another key issue for studying the correlation of muon showers and neutron background in the EDELWEISS-II bolometers is the angular, and thus lateral distribution of neutrons produced by muon interactions.
In *Geant4* the muon nuclear interaction, as discussed in section 3.2.2 and Appendix A, is described by using the total cross section formulae of [Bor75] on basis of the real photo nuclear reaction. The latter is described by an energy transfer to the nucleus and a de-excitation of the nucleus. The final state hadronic vertex is determined by the use of parametrised hadronic models, see section 3.2.3 for details on the models used. Taking into account this connexion, the results obtained by studying the angular distribution of secondary particles in muon nuclear interactions can be transferred without loss of generality to other nuclear reactions as well.

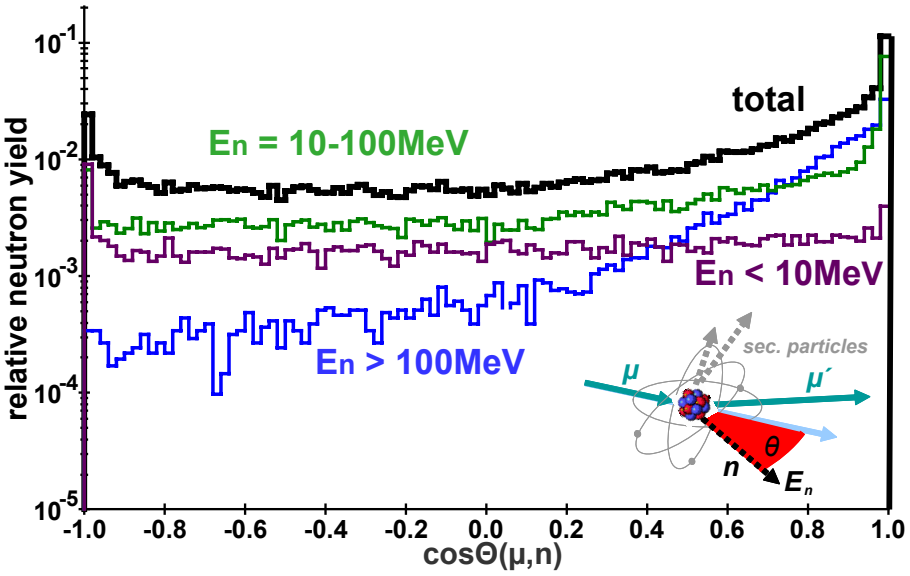


**Figure 3.9:** Angular distribution relative to the total neutron yield of neutrons produced in muon nuclear reactions with *Geant4* `8.2.p01`. For all neutron kinetic energies (black) or the respective kinetic energy ranges, $E_n > 100\ MeV$ (blue), $10\ MeV < E_n < 100\ MeV$ (green) and $E_n < 10\ MeV$ (purple). The inlet shows the definition of the angle $\theta$ with respect to the incident muon. See text for details.

The results for the angular distribution for neutrons in muon nuclear interactions is shown in 3.9. As can be seen, the total angular distribution of neutrons (black line) is rather forward directed. The flat distribution for larger angles can be assigned to low energetic neutrons (green and purple line) evaporating isotropically from the nuclei as a result of Giant Dipole- or Δ- resonances (see section 3.2.2). However, neutrons with kinetic energies at the production vertex of more than $E_n > 100\ MeV$, considered as neutrons able to penetrate the polyethylene and lead shielding and thus a possible background source for the EDELWEISS-II experiment, are strongly correlated with the incident muon. For instance, high energetic neutrons with scattering angles $\theta > 45°(\sin\theta < 0.7)$ are already suppressed by an order of magnitude. To a smaller extent this can be seen for intermediate neutron kinetic energies as well. This issue is of great relevance while studying the veto capabilities of muon-induced neutron events in the bolometers, see chapter 6. The observed neutron flux in backward direction in figure 3.9 can be attributed to the neutrons with kinetic energies of $E_n = 1\ keV$ which are considered as a simulation artefact as discussed in the previous section.

Simulations of similar type as in sections 3.3 and 3.4, i.e. monoenergetic muons with $E_\mu = 280\ GeV$ on a block of generic hydrocarbon $C_nH_{2n}$ of $X = 4000\ g/cm^2$ thickness and similar lateral dimensions, are performed using *Geant4* `8.2.p01` and the physics list described in section 3.2. The resulting distribution of neutron production

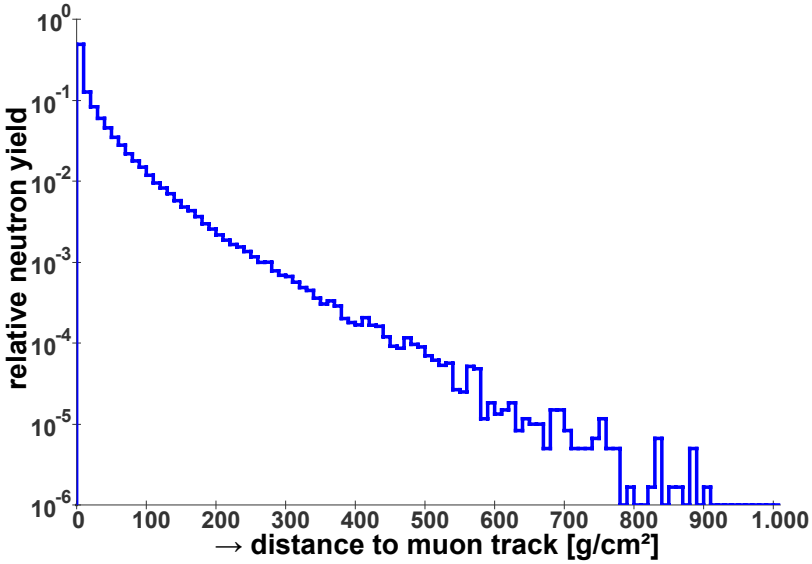


**Figure 3.10:** The lateral neutron production as distance to the muon track in $g/cm^2$ for $E_\mu = 280\ GeV$ in a block of $C_nH_{2n}$ with thickness $X = 4000\ g/cm^2$.

vertices for all neutron production processes is shown in figure 3.10.
Recapitulatory, neutrons produced in muon-induced showers, especially with kinetic energies above $E_n = 100\ MeV$ are strongly correlated with the incident muon and in general are not produced far from the muon track. Conclusions drawn on this subject to the muon-induced background rate are discussed in more detail in chapter 6.

# 4 The muon flux at the LSM

The EDELWEISS experiment is placed in the underground laboratory of Modane, the Laboratoire Souterrain de Modane (LSM), in the French-Italian alps. The rock overburden of this laboratory is a mountain range stretching along the geographical east-west axis with a vertical extent of at most 1740 $m$. Due to the rock shielding, the muon flux in the underground laboratory is significantly different to the one on sea level. The effect of the rock overburden on the mean energy of the muon flux in the underground laboratory, its differential energy distribution and the angular distribution are the subject of this chapter.

## 4.1 The muon flux underground

Primary cosmic ray particles interact with the atoms of the Earth's atmosphere and produce secondary particles. These particles together form a cascade, or air shower. Measurements of these secondary particles on ground can be interpreted in terms of the energies and the composition of the primary cosmic ray particle. The air shower development can be modelled analytically by solving the transport equations of the particles through the Earths's atmosphere. Following the approach by Th. Gaisser [Gai90], the fluxes of secondary particles are determined by systems of coupled cascade equations. There, the abundance of each particle class can be described by the appropriate production mechanisms and by taking into account the reduction by interaction and decay. The cosmic ray muon flux is dominated by the decay of mesons, mainly charged pion decay, e.g. $\pi^+ \rightarrow \mu^+ + \nu_\mu$ and $\pi^- \rightarrow \mu^- + \bar{\nu_\mu}$, and charged kaon decays, e.g. $K^+ \rightarrow \mu^+ + \nu_\mu$ and $K^- \rightarrow \mu^- + \bar{\nu_\mu}$. Muons are heavy elementary particles with a mass of $m_\mu = 105.7\ MeV$ and a lifetime of $\tau_\mu = 2.197\ \mu s$ [Yao06]. Produced by very high energetic cosmic ray particles, muons are generally continuing in the same direction as the primary with very high velocities $v_\mu \approx c$. Despite their lifetime, muons can reach the Earth's surface due to the time dilation attributed to their high velocities. Furthermore, since muons do not emit as much bremsstrahlung radiation as electrons due to their greater mass and together with their relatively small cross sections for interactions with matter, they are called the 'penetrating component' of the cosmic ray air showers. In effect, muons are the most numerous charged particles at sea level with an intensity of $I \approx 1\ cm^{-2}min^{-1}$ on vertical detectors and an average muon energy of $E_\mu \approx 4\ GeV$ [Yao06].

An approximation of the muon energy and angular distribution can be determined by taking into account the production spectrum, the energy loss in the atmosphere

and the decay. In general, the energy spectrum of cosmic ray particles at the top of the atmosphere is given by the segmented power-law formula:

$$\frac{dN}{dE} \propto E^{-\gamma} \tag{4.1}$$

with the spectral index $\gamma = 2.7$ for $E < 10^7\ GeV$ and $\gamma = 3.0$ for $10^7 < E < 10^9\ GeV$. Starting from the primary particle spectrum, the production spectra of mesons in nuclear reactions in the atmosphere can be calculated using experimentally measured cross sections. It can be shown, that the energy spectrum of mesons approximately has the same spectral index as the one of the primary particles (in the energy range relevant to producing muons reaching down to underground laboratories, i.e. $E_\mu \gtrsim 3\ GeV$). Also the angular distribution of high energetic mesons corresponds to the angular distribution of the primary particles ($\propto 1/cos\theta$) due to the small transverse momentum transfer. Gaisser then proceeds to calculate the muon flux by meson decay. Accounting for the two-body decays of pions and kaons, the energy and angular distribution of muons at sea level can be obtained after integration over the production spectrum in the whole atmosphere. With numerical values for the various quantities, the muon spectrum for high energies, where muon decay is negligible, i.e. $E_\mu > 10\ GeV$, is given by [Gai90]:

$$\frac{dN_\mu}{dE_\mu} = \frac{0.14\ E_\mu^{-\gamma}}{cm^2\ s\ sr\ GeV} \left\{ \frac{1}{1 + \frac{1.1 E_\mu cos\theta}{115\ GeV}} + \frac{0.054}{1 + \frac{1.1 E_\mu cos\theta}{850\ GeV}} \right\}, \tag{4.2}$$

with the cosmic ray exponent $\gamma = 2.7$ and the zenith angle $\theta$, with a correction accounting for the Earth's curvature[1]. The two terms in the brackets in this equation represent the muons from the two main production mechanisms: the pion and kaon decay, respectively.
As aforementioned, the equation does not account for the energy loss of muons and is therefore only correct at relatively high energies, when the energy loss is only a small fraction of the muon energy. However, for relatively large zenith angles and low muon energies, e.g. for $E_\mu < 100\ GeV/cos\theta$ and $\theta > 70°$, the muon decay cannot be neglected and equation (4.2) overestimates the measured muon flux. The muon spectrum has two important features according to equation (4.2). First, at low energies ($E_\mu \ll 100\ GeV$), the muon spectrum has the shape of the primary cosmic ray spectrum, whereas at higher energies it steepens by one power of $E_\mu$ as the thickness of the atmosphere is too little for pions to decay. Secondly, because of the $cos\theta$ factor, the pion decays more easily in non vertical showers and the muon energy spectrum is flatter for large zenith angles.

For muons in cosmic ray showers the only essential energy loss process is ionisation since the vertical atmospheric depth, in terms of column density, is around $X =$

[1] The zenith angle $\theta^*$ of primary particles on the top of the atmosphere transfers to a zenith angle $\theta$ on Earth by taking into account the curvature of the Earth and is given by: $sin\theta = sin\theta^* \frac{R_E + H_{\text{int}}}{R_E}$, where $R_E = 6600\ km$ is the Earth's radius and $H_{\text{int}} = 18.6\ km$ is the mean interaction height for primary particles in the atmosphere [Rho93].

$\rho_{\text{atm}}\ h \approx 1000\ g/cm^2$. Introducing the unit of a meter water equivalent $1\ mwe = 100\ g/cm^2$ and assuming an average density of rock between $2.6 < \rho_{\text{rock}} < 2.8\ g/cm^3$, the column depth of the entire atmosphere corresponds only to a few meters of the Earth's upper crust. To derive the muon spectrum at typical underground laboratories with depths of a few thousand $mwe$, also other processes of muon energy loss become increasingly important. As shown in Appendix A, ionisation energy loss depends only weakly on the muon energy and in first approximation can be considered constant at about $dE_{\text{ion}}/dX \equiv a \approx 2\ MeV/(g/cm^2)$. The energy loss of bremsstrahlung, $e^+e^-$-pair production and muon nuclear interaction (often denoted as deep inelastic scattering, DIS) on the other hand is approximately proportional to the muon energy. It is convenient to approximate the total energy loss for muons as a function of the amount of matter traversed as [Yao06]:

$$\frac{dE_\mu}{dX} = a \ + \ b\ E_\mu \tag{4.3}$$

where $b = b_{\text{brems}} + b_{\text{pair}} + b_{\text{DIS}}$ is the sum of the fractional energy loss of bremsstrahlung radiation, $e^+e^-$ pair production and nuclear scattering processes, respectively. In this connexion, $a$ and $b$ are considered as energy independent values. From equation (4.3), the critical muon energy at which ionisation loss equals radiation loss is determined to $\epsilon = a/b$, i.e. the energy loss is dominated by radiation for muon energies $E_\mu \gg \epsilon$ and by ionisation for $E_\mu \ll \epsilon$. Assuming a continuous energy loss for muons propagating through rock and neglecting fluctuations due to individual radiation processes, the initial energy of a muon at sea level $E_\mu(X = 0) \equiv E_0$ and the final energy $E_\mu(X) \equiv E_{\text{Lab}}$ in an underground laboratory at depth $X = t$ can be calculated by:

$$t \ = \ \int_{E_{\text{Lab}}}^{E_0} \frac{dE_\mu}{dE_\mu/dX} \tag{4.4}$$

Together with equation (4.3) the quantities can be written as:

$$E_{\text{Lab}} = (E_0 + \epsilon)\ e^{-bt} - \epsilon \tag{4.5}$$

$$E_0 = (E_{\text{Lab}} + \epsilon)\ e^{+bt} - \epsilon \tag{4.6}$$

$$t = \frac{1}{b}\ ln\left(\frac{E_0 + \epsilon}{E_{\text{Lab}} + \epsilon}\right). \tag{4.7}$$

where the minimum muon energy needed by a muon to penetrate to a depth $t$ can be obtained by (4.6) and $E_{\text{Lab}} = 0$:

$$E_{\text{min}} = \epsilon\ (e^{-bt} - 1) \tag{4.8}$$

The assumption of continuous energy loss is reasonable for the muon energy range where most of the energy loss is due to ionisation. At higher muon energies the energy loss by radiation processes dominates and muons interact occasionally and lose a relatively large fraction of their energy in single processes. Due to these fluctuations the muon energy at a given underground depth is replaced by a distribution of

energies. Muons that do not radiate have a higher energy $E_{\mathrm{Lab}}$. Most of the muons however lose energy in radiation processes and will have a lower energy or potentially do not reach the underground lab at all. This can be accounted for by introducing a survival probability to the intensity of muons in an underground laboratory:

$$I(t) = \int \frac{dN_\mu}{dE_\mu}\, P_{\mathrm{surv}}(E_\mu, t)\, dE_\mu \tag{4.9}$$

where $I$ is the muon intensity, $P_{\mathrm{surv}}$ is the muon survival probability at depth $t$ and $dN_\mu/dE_\mu$ is the initial differential muon energy spectrum.

With the goal to study qualitatively the muon energy spectrum in an underground laboratory, one can assume a power law energy spectrum for vertical muons at sea level according to equation (4.1) and (4.2):

$$\frac{dN}{dE_0} = A \cdot E_0^{-\gamma_\mu} \tag{4.10}$$

where $A$ is a normalisation constant and $\gamma_\mu = 3.7$ the spectral index of the muon beam. Within the approximation of continuous energy loss and the validity of equation (4.6), the muon spectrum at a depth $t$ is then:

$$\frac{dN}{dE_{\mathrm{Lab}}} = \left.\frac{dN}{dE_0}\right|_{E=E_{\mathrm{Lab}}} \times \frac{dE_0}{dE_{\mathrm{Lab}}} = Ae^{-bt(\gamma_\mu - 1)} \cdot (E_{\mathrm{Lab}} + \epsilon(1 - e^{-bt}))^{-\gamma_\mu}, \tag{4.11}$$

At very large depths underground, i.e. $t \gg 1/b$, the differential spectrum is almost constant at lower energies up to $E_\mu \simeq \epsilon$ and steepens above to reflect the muon spectrum above ground with the spectral index $\gamma_\mu$.
With equation (4.11), one can calculate the mean muon energy $\langle E_{\mathrm{Lab}}(t)\rangle$ at an underground laboratory of depth $t$ as:

$$\langle E_{\mathrm{Lab}}\rangle = \frac{\int E_{\mathrm{Lab}} \frac{dN}{dE_{\mathrm{Lab}}} dE_{\mathrm{Lab}}}{\int \frac{dN}{dE_{\mathrm{Lab}}} dE_{\mathrm{Lab}}} = \frac{\epsilon(1 - e^{-bt})}{\gamma_\mu - 2} \overset{t \gg 1/b}{\longrightarrow} \frac{\epsilon}{\gamma_\mu - 2} \tag{4.12}$$

For the LSM underground laboratory and the Fréjus mountain overburden, the mean muon energy can be determined by specific values for $a$ and $b$ according to the properties of the rock overburden. With the values taken from [Rho93], see also table 4.1, the mean muon energy can be approximated to $\langle E_{\mathrm{LSM}}\rangle \approx 290\, GeV$. As discussed in [Rho93], the value $a$ representing the energy loss by ionisation is neither dependent on the detailed rock composition nor strongly model dependent. On contrary, the value $b$ as the sum of the contribution of the radiation and scattering processes, for example, varies with the model of the rock overburden and also, calculations of the cross section for muon bremsstrahlung yield to deviations of the value $b$ within 5%. Further uncertainty on the mean muon energy, as approximated by equation (4.12), arise from the uncertainty of the muon spectrum in the atmosphere, i.e. the value of $\gamma_\mu$, which may vary also within a few per cent.
In the approximation of equation (4.12), besides the critical energy $\epsilon$ and the initial muon spectral index $\gamma_\mu$, no further information is necessary. However, taking into

| parameter | value | | |
|---|---|---|---|
| energy loss | $a$ | = | $0.217\ GeV/mwe$ |
| | $b$ | = | $4.38 \cdot 10^{-4}\ 1/mwe$ |
| | $\epsilon$ | = | $495\ GeV$ |
| rock density | $\rho$ | = | $2.74\ g/cm^3$ |
| average rock overburden | $\langle t \rangle$ | = | $4600\ mwe$ |
| mean muon energy | $\langle E_\mu \rangle$ | $\approx$ | $260 - 290\ GeV$ |
| total muon intensity | $\Gamma_{\text{tot}}$ | = | $4.73 \pm 0.09\ m^{-2}d^{-1}$ |

**Table 4.1:** Properties of the LSM underground laboratory concerning the muon spectrum calculations [Ber89; Rho93; Mei06]. See text for details.

account additional information regarding the rock overburden and mountain shape, an average depth of the underground laboratory can be deduced by integration of the depth profile [Mei06]:

$$\langle h \rangle = \int sin\theta \; d\theta \int d\varphi \; h(\theta, \varphi) \tag{4.13}$$

with the slant depths $h(\theta, \varphi)$ of the rock overburden. For the LSM underground laboratory, an $1° \times 1°$ elevation map in zenith and azimuth angles is available, see also section 4.2, and the average depth can be calculated to $\langle h_{\text{LSM}} \rangle \equiv \langle t \rangle \approx 4600\ mwe$. Together with equation (4.12), the mean muon energy at LSM is then $\langle E_{\text{LSM}} \rangle \approx 260\ GeV$. A summary of the determined values for the Fréjus underground laboratory, amongst others the mean muon energy, the average depth and the specific values for $a$ and $b$, are given in table 4.1. The particular energy and angular spectrum of the muons at LSM, as used in the simulations of this work, are discussed in more detail in the next section.

As discussed in [Mei06], the average depth $\langle t \rangle$ should not be confused with the equivalent vertical depth relative to a flat overburden $\bar{t}_{\text{eq}}$ as determined by studying Depth-Intensity-Relations (DIR) as proposed by [Gro73; Cas73]. Following the approach of DIR, an equivalent flat overburden for the LSM underground laboratory of $\bar{t}_{\text{eq}} = 4200 \pm 200\ mwe$ is determined in [Mei06]. Note that the elevation map used herein is an older $5° \times 5°$ depth profile from [Ber89]. The calculated average depth with this map, as reported in [Mei06], is $\langle t \rangle\,(5° \times 5°) = 5000\ mwe$. This value is $\sim 8\%$ higher then the one calculated using the elevation map with better resolution. To summarise the results of [Mei06], the average physical depth taking into account the distinct shape of the mountain range above an underground laboratory is in general $\sim 15\% - 20\%$ higher than the equivalent depth for a flat overburden defined by experimental measurement of the total muon flux. Moreover, the mean muon energy, as determined or approximated for vertical muons by equation (4.12), relies, besides the discussed uncertainties of the values $a$, $b$, $\epsilon$ and $\gamma_\mu$, also on the value of the underground depth. But due to very scarce data on underground muon measurements, i.e. differential and angular spectrum measurements, the comparison of the different models is difficult. The results of the MACRO experiment in the

Gran Sasso underground laboratory [Amb03], however, agree within the uncertainty of the measurement with the predicted values for a different set of parameters. These difficulties of the model and the lack of experimental data has to be considered when comparing data on the total muon intensity at various underground sites as a function of depth. Furthermore, particular attention has to be given to the comparison of muon-induced neutron fluxes, as often quoted, as a function of mean muon energy at the depths of various underground sites, see also chapter 3.3.

## 4.2 Muon distribution in the LSM underground laboratory

The equations derived in the previous section for the muon flux in an underground laboratory are valid only for vertical muons. In this approximation, the rock overburden is taken as the effective depth of the laboratory. However, muons reach the underground laboratory from all zenith and azimuth angles. Under the assumption of continuous energy loss and valid equations (4.5) - (4.7), it is straightforward to calculate the muon intensity for a specific slant depth $h$ in the direction of zenith and azimuth angle $(\theta, \varphi)$ by equation (4.9):

$$I(h(\theta,\varphi)) = \int \frac{dN}{dE_0}(E_0,\theta)\ P_{\mathrm{surv}}(E_0, h(\theta,\varphi))\ dE_0 \tag{4.14}$$

where additional information regarding the mountain shape or elevation map $h(\theta, \varphi)$ is required and the angular distribution of muons above ground $dN/dE_0(E_0, \theta)$ is given by Gaisser's approximation, equation (4.2). With the assumption that fluctuations in the energy loss are negligible, the survival probability can be written as a simple step function: $P_{\mathrm{surv}}(E_0, h) = \theta[E_0 - E_{\mathrm{min}}(h)]$.
For the LSM underground laboratory and the Fréjus mountain range, a precise cartographic map determined by data from a space shuttle mission in $1^\circ \times 1^\circ$ zenith- and azimuth angles is available [Wei93]. The total muon intensity can be calculated by integration over all solid angles:

$$I_{\mathrm{tot}} = \int sin\theta\ d\theta \int d\varphi\ I(h(\theta,\varphi)) \tag{4.15}$$

where $I(h(\theta, \varphi))$ is given by equation (4.14). Using the elevation map $h(\theta, \varphi)$ for the Fréjus mountain range and integrating over all $\theta$ and $\varphi$, the local muon flux as a function of muon energy can be calculated. The resulting muon energy spectrum at the underground laboratory LSM, shown in figure 4.1, does not differ significantly from the one expected for a flat overburden and an effective depth as modeled in [Mei06].

However, the angular distribution, calculated with the elevation map $h(\theta, \varphi)$, depends strongly on the shape and orientation of the mountain overburden. According to equation (4.2) one expects in the first approximation a distribution

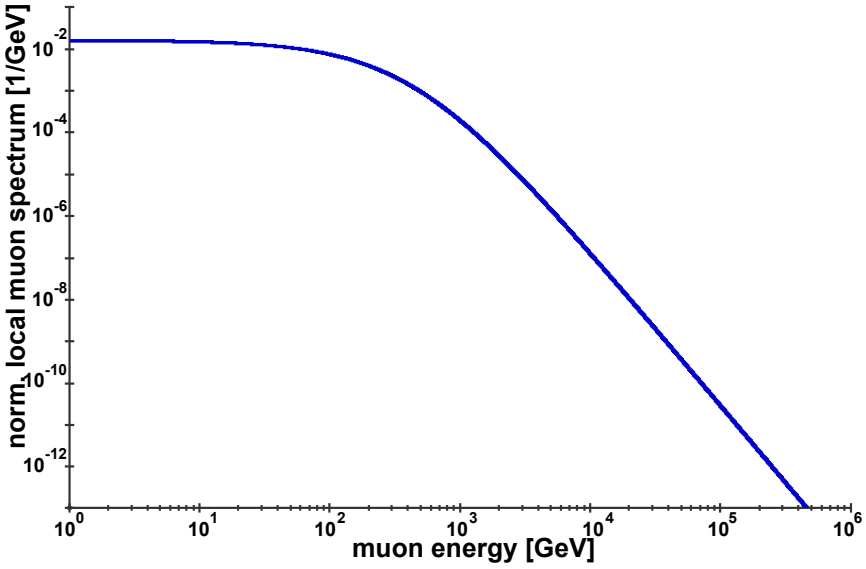


**Figure 4.1:** The local muon energy spectrum for the LSM underground laboratory, normalised to unity.

in the zenith[2] angle $I(h(\theta, \varphi)) \sim 1/cos\theta$. For large zenith angles, the effect of increasing rock overburden further lowers the muon flux. Therefore the muon flux in direction of $\theta > 70°$ is suppressed by two orders of magnitude and can be neglected. For smaller zenith angles, the difference of rock overburden in east-west and north-south direction averages by integration over all azimuth angles. The resulting local muon distribution as a function of zenith angle $\theta$, compared to the measurement of the Fréjus experiment, is shown in figure 4.2.

The muon distribution as a function of the azimuthal angle, together with the experimental data is shown in figure 4.3. Note that the coordinate system of the laboratory is not perfectly aligned with the geographical north-south axis. The geographical north direction is towards $\varphi^N = 16°$; east $\varphi^E = 106°$, south $\varphi^S = 196°$ and west $\varphi^W = 286°$, respectively. As can be seen, significantly more muons arrive from the north-south direction, i.e. from the valleys, since the mountain range above the LSM underground laboratory is stretched dominantly along the geographical east-west axis. Also, the rock overburden strongly increases with increasing zenith angles in the east-west direction due to adjacent mountains. This results in differences up to a factor $\sim 5$ for the differential muon flux, e.g. between $\varphi \approx 25°$ with the least rock overburden and $\varphi \approx 275°$ pointing into the western direction of the laboratory along the mountain range.

For the *Geant4* simulations of this work, the relative probability $P$ for muons entering the underground laboratory under the solid angle $(\theta, \varphi)$ and with the energy

[2]In fact, the zenith angle $\theta$ is replaced by the corrected zenith angle $\theta^*$, taking into account the Earth's curvature, see also footnote 1.

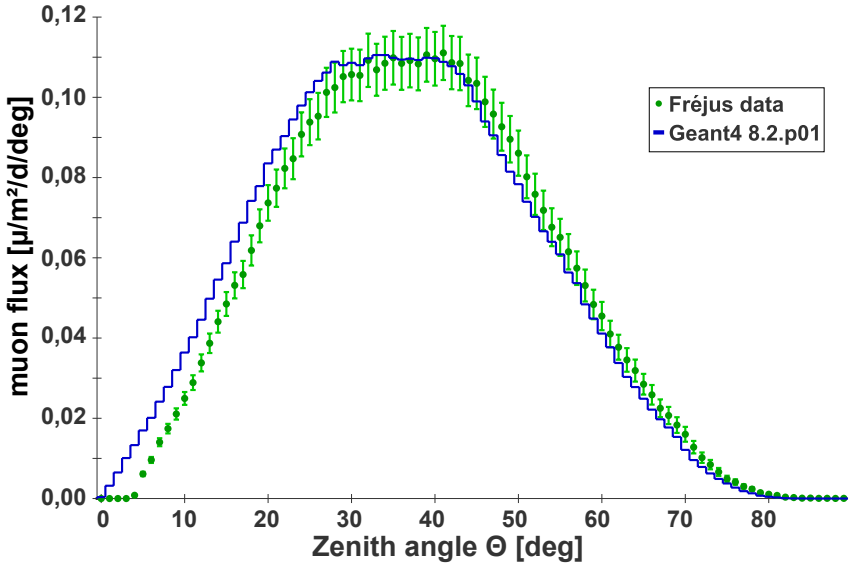


**Figure 4.2:** The local muon spectrum as a function of zenith angle $\theta$ for the LSM underground laboratory compared with experimental data obtained by the Fréjus experiment. The simulations are not corrected to the detector efficiency. See text for details.

$E_\mu = E_{\text{Lab}}$ are calculated combining equation (4.2), (4.11) and the elevation map $h(\theta, \varphi)$:

$$P(E_\mu, \theta, \varphi) = \frac{\Gamma_\mu(E_{\text{Lab}}, \theta, \varphi)}{\Gamma_{\text{total}}} \tag{4.16}$$

where $\Gamma_\mu$ is the differential muon flux calculated for muon energies in the range of $E_{\text{Lab}} = 2 - 2000\ GeV$ in logarithmic bins of size $\Delta E_\mu$ for all solid angles $(\theta, \varphi)$ as:

$$\Gamma_\mu = \frac{dN_\mu}{dE_\mu}(E_\mu, \theta, \varphi)\ \Delta E_\mu\ \sin\theta\ \Delta\theta\ \Delta\varphi \tag{4.17}$$

where $\Delta\theta = \Delta\varphi = 1$ for a $1^\circ \times 1^\circ$ elevation map $h(\theta, \varphi)$. The total muon flux $\Gamma_{\text{total}}$ is normalised to the experimentally measured muon intensity for a flat, horizontal area at the underground laboratory LSM by the Fréjus experiment [Ber89]:

$$I_{\text{tot}}(\text{Fréjus}) \equiv \Gamma_{\text{tot}} = (5.47 \pm 0.10) \times 10^{-9} cm^{-2} s^{-1} \tag{4.18}$$

$$= (4.73 \pm 0.09) \times m^{-2} d^{-1} \tag{4.19}$$

In both figures 4.2 and 4.3, the muon flux obtained by the discussed analytical approach is compared to the measurement of the local muon flux in the LSM underground laboratory by the Fréjus experiment. A detailed description of the experimental setup and the physical outcome relevant for this work can be found in [Ber87; Ber89; Sch90; Rho93; Wei93; Rho96]. The Fréjus experiment was dedicated

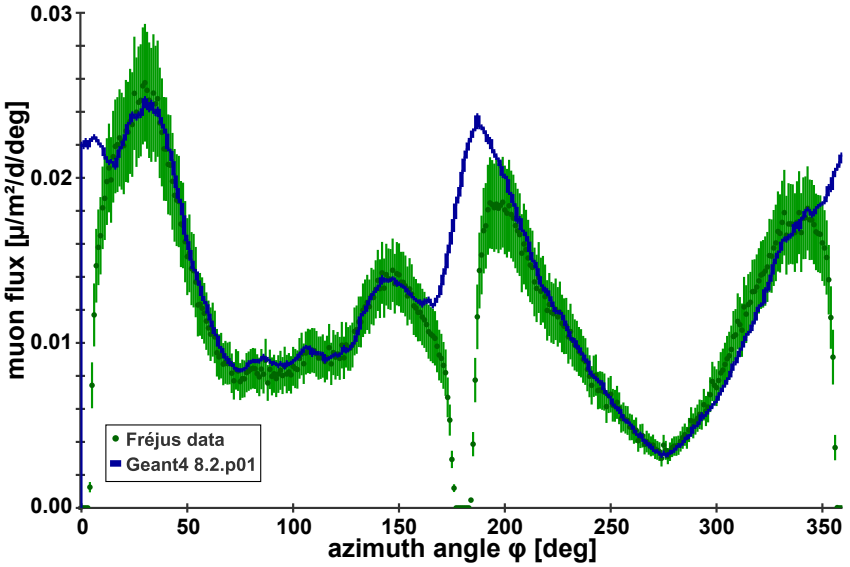


**Figure 4.3:** The local muon spectrum as a function of azimuth angle $\varphi$ for the LSM underground laboratory integrated over all zenith angles. The experimental data is obtained by the Fréjus experiment. A $\varphi$ of 16° in this coordinate system of the laboratory is the geographical north direction. See text for details.

to study the possibly finite lifetime of protons. The detector was made of vertical detector layers with interjacent iron plates. One of the main properties of the detector was the good spatial and angular resolution in track reconstruction of non-showering charged particles, as for example of cosmic ray muons. Thereby, for an average spatial resolution of 0.7 $m$ an angular resolution of 0.4° was achieved. The muon data, as plotted in figure 4.2 and 4.3, was determined by a total of around half a million muon events accumulated over a period of around 1200 days. Muon tracks in the experiment could only be reconstructed by hits in multiple detector layers. Due to the vertical arrangement of these layers, parallel to the laboratory hall, the detector acceptance was limited to $\theta > 4°$ with two blind angles in azimuthal direction, namely $\varphi = 0°$ and $\varphi = 180°$ (in the coordinate system of LSM, not representing geographical directions). Besides the differences due to the limited acceptance of the Fréjus experiment a good agreement is found between the analytical approach and the experimental data. In the figures 4.2 and 4.3, no corrections to the simulation results are made according to the acceptance and efficiency of the experimental data and thus the comparison is mainly for illustration purposes.

## 4.3 First measurements with the EDELWEISS-II muon veto system

The muon veto system of the EDELWEISS-II experiment, as described in chapter 2.2.2, is completely installed and in operation in the LSM underground laboratory since July 2006. The electronics of the muon veto system and the data read-out are fully independent of the bolometer system, as described in chapter 2.2.2 and in [Hab04].

Data is read out from each end of the 42 scintillator module with a rate of $\Gamma \sim 8\ kHz$ for the overall system, composed mainly of background. This rate of stored raw data events is much higher than the expected muon hit rate of around a few $\mu Hz$ for the full muon veto system due to deliberately low thresholds with the goal not to miss any muons [Cha07b]. Between July 2006 and September 2007, data was taken over long periods with almost continuous data acquisition. Interruptions were made mainly during extensive work periods in the clean room, e.g. bolometer extensions, when the high voltage of the veto system was switched off for safety reasons. The effective measuring time accumulates to $t \approx 243$ live-days [Cha07a]. In an off-line analysis, throughgoing muon candidate events are determined by simply requiring coincidences of one module on one side of the muon veto system, e.g. the top side (Top), and any module of another side, e.g. the bottom side (Sol), see chapter 5.1 for details on denotation of the sides of the muon veto system. In a preliminary analysis, a total of 8475 muon candidates could be identified corresponding to a total muon rate of the muon veto system $\Gamma_{\mathrm{tot}} = 34.8 \pm 0.4\ d^{-1}$. An in-depth comparison of the muon rates for different geometrical coincidence conditions with *Geant4* simulations of this work is done in chapter 5. Further investigations on the muon flux with the EDELWEISS-II muon veto system and the correlation with bolometer events is done in [Chaon].

# 5 EDELWEISS-II simulations with Geant4

The simulation code *Geant4* provides the ability to describe complex geometrical structures and to propagate particles efficiently through them. Given the design of the muon detector in the EDELWEISS-II experiment as described in chapter 2.2 and measurements of sizes, distances and offsets to technical drawings on site in the underground laboratory, a full $3D$-implementation of the experiment is achieved. Together with the underground muon flux, as discussed in chapter 4, the performance of the veto system is simulated, and the expected mean energy deposit for the various orientations of scintillator modules of the veto system is studied. Then, the total geometrical muon detection efficiency is determined. After introducing the implementation of the complete experimental setup of the EDELWEISS-II experiment, including rock overburden, shielding and Germanium detectors, comparisons with first preliminary experimental data measured with the EDELWEISS-II muon veto system in the underground laboratory of Modane are made.

## 5.1 The EDELWEISS-II muon veto system

The muon veto system of the EDELWEISS-II experiment must provide an excellent muon detection efficiency to set the rate of undetected muons to a minimum. There is a multitude of organic or inorganic, liquid or solid scintillator materials potentially suited for a veto system. However, to meet the high demands on the veto system, in terms of muon detection efficiency within the experimental design and the limited space available, the use of solid organic scintillator materials is preferred. First, due to their high light emitting efficiency and very good transparency, large contiguous areas can be realised while having a reasonable good energy resolution. Furthermore, the handling and operation of solid scintillator modules in an underground laboratory is less complicated than for example of liquid scintillator detectors. In the EDELWEISS-II setup, the veto system consists of 42 plastic scintillator modules of type BICRON BC-412. They are arranged almost hermetically around the cryostat, housing the Germanium detectors, the 20 $cm$ of lead and the 50 $cm$ of polyethylene shielding to ensure a very high geometrical detection efficiency. See also chapter 2.2 for more details on the complete experimental setup of EDELWEISS-II.
A requirement for the veto detector system is to separate background events, i.e. low energy electron and photon interactions, from muon events. The data signals of the EDELWEISS-II veto system are read out on both ends of the modules and coincident triggers above a discriminator threshold define a module hit. On the one hand, low

thresholds are needed to ensure the detection of all muons. On the other hand, the veto system should not be overwhelmed by low energy gamma background, which would, applying a certain deadtime after each veto hit, e.g. $t \approx 100\ \mu s$, decrease the effective measuring time for the Dark Matter search. In consequence, to determine the muon detection efficiency of the veto system, the energy deposit of muons in the modules is studied beforehand.

### 5.1.1 Mean muon energy deposit per module

Underground cosmic ray muons, as high energy charged particles, lose energy in matter according to Bethe-Bloch's formula, see Appendix A. In first approximation, the energy loss for muons with high kinetic energies of $\langle E_\mu \rangle_{\mathrm{LSM}} \approx 300\ GeV$ in a thin layer of matter, e.g. horizontal plastic scintillator modules with a material density of $\rho_{\mathrm{PVT}} \approx 1\ g/cm^3$, is $\frac{dE_\mu}{dX} \approx 2\ MeV/cm$. As a result, the mean muon energy deposit for vertical muons in a module of thickness of $d = 5\ cm$ is approximately $\langle E_{\mathrm{dep}} \rangle \approx 10\ MeV$. The fluctuations in energy loss can be described by a Landau-distribution. For example, figure 5.1 shows the measured energy deposit distribution for muons in a horizontal plastic scintillator module. The measurement was made in Karlsruhe, with a module of the EDELWEISS-II muon veto system before installation in the underground laboratory LSM [Hab04]. The module has a thickness of 5 $cm$; the length of the particular module is 4 $m$, but results do not change significantly for the various lengths of 3.75, 3.15 or 2 $m$, respectively. The recorded events are coincidences of the module with two small plastic scintillator paddles, one above and one underneath the module, of $\approx 50\ cm^2$ surface area each. Within this setup, the mean track length of cosmic ray muons in the veto module is well defined and low energy background events, i.e. electron and photon interactions, are rejected. In addition, a linear relation between the energy emitted by fluorescence and detected with the photomultipliers at each end of the module, i.e. the entries in ADC-channels, and the dissipated energy in the scintillator, i.e. the energy deposit $E_{\mathrm{dep}}$, can be established using Monte Carlo simulations. The fitted Landau distribution in figure 5.1 has a maximum at $E_{\mathrm{MPV}}$ (*most probable value*) and a mean value $\langle E_{\mathrm{dep}} \rangle$ characteristically at a higher energy. The comparison with *Geant3* simulations yield a value for the Landau maximum of $E_{\mathrm{MPV}} = 10.5\ MeV$ for horizontal modules at sea level. The principle of this shortly outlined method and the results of the detailed simulations are described in [Rei98].

In the EDELWEISS-II setup not all modules are laid out horizontally. Since the modules are placed in a cubic geometry around the cryostat and the shielding material, most of the modules are in fact placed vertically. Moreover, the muon flux in the underground laboratory LSM, see chapter 4.2, is significantly different from the one at sea level in terms of angular distribution. The direction of the muons, thus the average muon track length in the modules and hence the muon energy deposit, differs considerably for the different sides of the veto system. To determine the mean muon energy deposit for the individual modules a precise $3D$-geometry of the EDELWEISS-II veto system at the LSM is implemented in *Geant4* simulations.

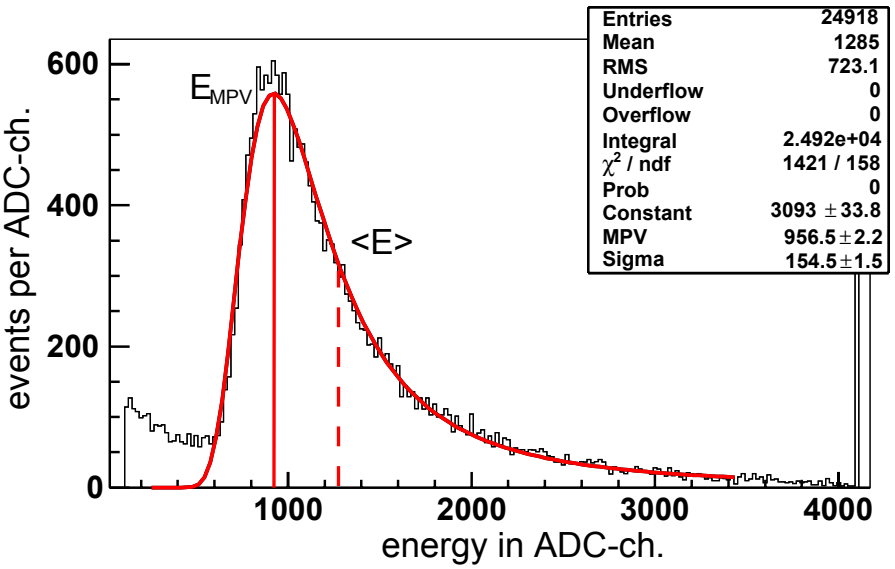


**Figure 5.1:** Muon energy deposit measured in a horizontal veto module of length $4m$ and $5cm$ thickness at sea level. The solid (red) line represents the Landau fit with the maximum $E_{\mathrm{MPV}}$ and the mean value $\langle E_{\mathrm{dep}} \rangle$ [Hab04]. See text for details.

Figure 5.2 is a schematic overview of the muon veto system as implemented in the simulations. The light guides at each end of a module, as indicated in figure 2.8, are also included to account for higher energy deposits as a result of the increased thickness at the end of each module. The distance between two adjacent modules is generally taken to $d = 7.5\ mm$, which is a reasonable assumption taking into account limiting closeness due to the mechanical construction, the packaging and irregularities in width of the plastic scintillator modules. Furthermore, on site measuring of various distances in the underground laboratory after installation of the veto systems are implemented in the geometry of the *Geant4* simulations, e.g. total measures of the system in east-west or north-south direction, total height, interspaces, offsets, etc.

The experimental setup of EDELWEISS-II can be divided into two levels according to the descriptions in chapter 2.2, namely *Niveau 0* for the lower and *Niveau 1* for the upper part. Each module is appointed a number, starting from 1 for the most eastern module on the top of the upper level to 48 for the one to the south on the ground floor. Each wall of the muon veto system is labelled according to the orientation in the underground laboratory. At this, the laboratory notation in French became accepted, where the west direction is replaced by 'Nemo', a neighboring experiment in the experimental hall of the LSM, to avoid confusion between 'Est' and 'Ouest'. As a result, the EDELWEISS-II muon veto system can be divided into ten different walls and named accordingly. For instance, the top side and the floor of the system are labelled N1-Top and N0-Sol, respectively. The side walls of Niveau 1 and Niveau 0 are labelled according to the corresponding

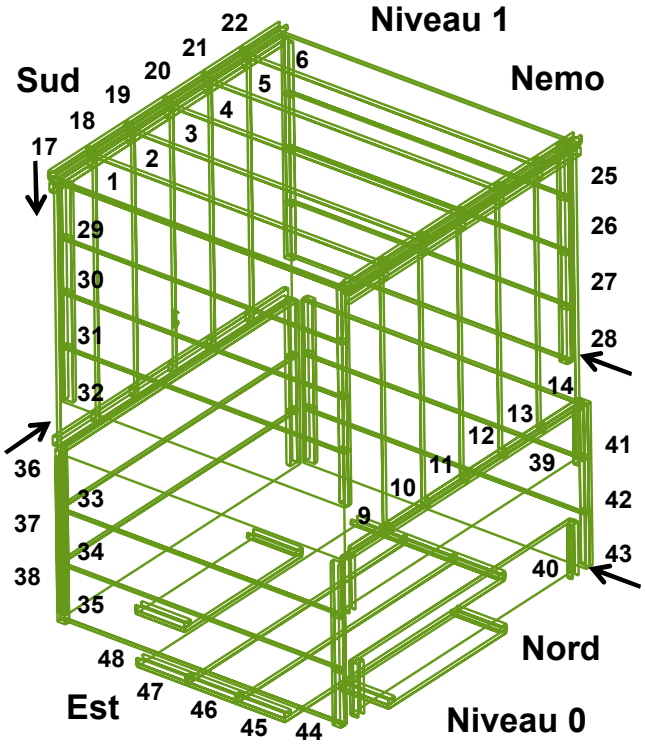


**Figure 5.2:** Scheme of the muon veto system of EDELWEISS-II as implemented in the *Geant4* simulations.

geographical direction, e.g. N1-Nord, N0-Nemo, etc.

In the *Geant4* simulations several millions of muons are simulated following the discussed underground muon spectrum as a consequence of the mountain overburden, see chapter 4.2. The results are analysed to determine the mean energy deposit for all scintillator modules. Since most muons are entering the underground laboratory with small zenith angles, note that the rock overburden is increasing with zenith angle, the average track length of muons in the top modules of Niveau 1 (No. $1-6$ or N1-Top) is approximately the thickness of the modules. Thus, the mean energy deposit for these modules is $\langle E_{\mathrm{dep}}\rangle^{\mathrm{N1\text{-}Top}} = 11.8\ MeV$. A similar result, i.e. $\langle E_{\mathrm{dep}}\rangle^{\mathrm{N0\text{-}Sol}} = 12.2\ MeV$, is obtained for the horizontal modules on the ground floor of Niveau 0 (No. $44-48$ or N0-Sol). As a consequence of the zenith dependence of the muon flux underground, muons going through vertical modules, e.g. No. $9-14$ or $17-22$, typically have longer track lengths and therefore the mean muon energy loss increases to $\langle E_{\mathrm{dep}}\rangle^{\mathrm{N1\text{-}Nord}} = 20.7$ or $\langle E_{\mathrm{dep}}\rangle^{\mathrm{N1\text{-}Sud}} = 20.8\ MeV$, respectively. In addition, more muons with larger zenith angle are entering the underground laboratory from the north and south than from the east and west due to the azimuthal dependence of the muon flux at the LSM. This directional difference can be held responsible for a higher mean muon energy deposit in the vertical veto modules on the east and west side of the experiment, i.e. No. $25-35$ and $41-43$. On these sides, less muons traverse the modules with high zenith angles and thus a shorter

| module No. | wall | orientation | $\langle E_{\mathrm{dep}} \rangle$ $[MeV]$ |
|---|---|---|---|
| $1-6$ | N1 Top | horizontal | 11.8 |
| $9-14$ | Nord | vertical (ss) | 20.8 |
| $17-22$ | Sud | vertical (ss) | 20.7 |
| $25-28$ | Nemo | vertical (ls) | 23.7 |
| $29-32$ | Est | vertical (ls) | 24.0 |
| $33-35$ | N0 Est | vertical (ls) | 23.8 |
| $36-38$ | Sud | vertical (ls) | 19.6 |
| $39-40$ | Nord | vertical (ls) | 19.9 |
| $41-43$ | Nemo | vertical (ls) | 23.9 |
| $44-48$ | Sol | horizontal | 12.2 |

**Table 5.1:** Mean muon energy deposit in plastic scintillator modules for different orientation in the EDELWEISS-II setup. *N1* and *N0* indicate modules on Niveau 1 and 0, respectively. The walls of the veto system are named according to the laboratory convention, where *Nemo* indicates the neighboring experiment in western direction and *Sol* is the ground floor. Vertical modules are laid out either on the short side (ss) or on the long side (ls). Muons are generated according to the muon flux considerations for the LSM in chapter 4.2.

mean muon track length. This results in an even higher mean energy deposit by muons of $\langle E_{\mathrm{dep}} \rangle^{\text{N1-Nemo}} = 23.7\ MeV$ and $\langle E_{\mathrm{dep}} \rangle^{\text{N0-Nemo}} = 23.9\ MeV$ for the western walls with compatible values for the eastern walls. Besides, a slight difference can be determined for modules of the north and south walls of Niveau 0 (No. $36-40$) to the ones from Niveau 1, e.g. $\langle E_{\mathrm{dep}} \rangle^{\text{N1-Nord}} = 20.8\ MeV$ to $\langle E_{\mathrm{dep}} \rangle^{\text{N0-Nord}} = 19.9\ MeV$. The modules on the lower floor are laid out on the long sides and the maximal track length for vertical muons is limited to the width of the modules. Therefore, very high energy deposits by muons traversing the full length of the module are not possible and the mean value is slightly lower than for modules laid out on the short sides, as on the upper floor or Niveau 1. A summary of the geometrical orientation of the modules and the simulated mean energy deposit $\langle E_{\mathrm{dep}} \rangle$ for all walls of the EDELWEISS-II veto system is given in table 5.1. The statistical errors on the determined values are negligible. A systematical error of $\sigma_E \approx 0.2\ MeV$ can be accounted to the muon generator of the Monte Carlo simulations.

### 5.1.2 Geometrical efficiency of the muon veto system

Despite the effort to hermetically enclose the EDELWEISS-II experiment with the muon veto system, the service pipes of the cryostat and the mechanical construction limit the geometrical efficiency of the veto system. As shown in figure 5.2, one module on the lower level of the north side (i.e. N0-Nord, between module No. 39 and 40) is lacking because of the presence of multiple supply pipes necessary for the operation of the cryogenic system. On the upper floor, i.e. N1-Sud, in module 20 a small trapezoidal hole of 75 $cm^2$ enables the pass of another cryogenic tube.

In addition, the area in between the rails, on which the upper shielding can be opened and closed, is left open without an additional veto module, i.e. on N1-Nemo below module No. 28 and on N1-Est below module No. 32. The area underneath the experiment is covered only by $\sim 70\%$ with scintillator modules by the apparent presence of the mechanical rack supporting the complete structure of the experiment. It should be noted that in close position of the two waggons a displacement towards the central detectors of $\Delta d \sim 6\ cm$ on the east- and westward sides between the upper and the lower level remains. This displacement is even more prominent for the polyethylene shielding, see section 5.2 for more details on that issue. To determine the geometrical efficiencies of the muon veto system, again several millions of muons are simulated according to the underground muon flux in the described geometry of the veto system. It is necessary for the calculation of the efficiency of the system to define a volume to attribute the effective muon flux entering the detector system. For this purpose, each wall on the lower and upper floor is underlaid with an imaginary area enclosing the complete volume of the EDELWEISS-II experimental setup. The geometrical efficiency for each side of the veto system is defined as:

$$\epsilon = \frac{N_\mu^{\text{veto-wall}}(E_{\text{dep}} > 2MeV)}{N_\mu^{\text{area veto-wall}}} \tag{5.1}$$

where the numerator represents the number of muon events with an energy deposit in the scintillator modules greater than a threshold of 2 $MeV$. The denominator represents the total number of muons passing through the according imaginary area underneath the modules. Furthermore the total efficiency is defined as:

$$\epsilon_{\text{total}} = \frac{N_\mu^{\text{veto}}(E_{\text{dep}} > 2MeV)}{N_\mu^{\text{volume veto}}} \tag{5.2}$$

where the denominator represents the number of muons entering the complete volume enclosed by the respective areas, taking into account the offset between the lower and upper floor and potential gaps and overlaps at the corners of the veto system. In table 5.2 the efficiencies for the individual walls together with the total efficiency are listed. Despite efficiencies for individual walls of the veto system of $\epsilon \lesssim 80\%$ a total geometrical efficiency of $\epsilon_{\text{total}} = 98.2\%$ is achieved. This can be ascribed to the strong zenith angle dependence of the muon flux together with the asymmetric angular distribution underground due to the rock overburden. For instance, on the top side as well as on N1-Nord and on N1-Sud, efficiencies of $\epsilon \gtrsim 98\%$ are achieved. As discussed in chapter 4.2, muons arrive in the underground laboratory LSM mainly towards these sides. Thus, the layout of the veto system is chosen to achieve the best possible geometrical muon detection efficiency. The result obtained is compatible with previous simulations using *Geant3* and a more simplified geometry [Cha04]. At this, a total geometrical efficiency of $\epsilon_{\text{tot}}^{\text{G3}} = 98.4\%$ is achieved. By studying only muons hitting the inner lead shielding, the geometrical efficiency increases to $\epsilon_{\text{Pb}}^{\text{G3}} = 99.7\%$.

| wall | | efficiency $\epsilon$ |
|---|---|---|
| N1 | Top | 99.7% |
| | Nord | 98.5% |
| | Sud | 98.4% |
| | Nemo | 79.7% |
| | Est | 78.3% |
| N0 | Est | 89.5% |
| | Sud | 91.2% |
| | Nord | 65.7% |
| | Nemo | 87.4% |
| | Sol | 67.4% |
| Total | | 98.2% |

**Table 5.2:** Geometrical efficiencies $\epsilon_{\text{side}}$ of all sides of the muon veto system together with the overall efficiency $\epsilon_{\text{total}}$. The energy deposit threshold for all modules is set to $E_{th} = 2\ MeV$.

## 5.2 The EDELWEISS-II simulation setup

With the goal to study the shower development of muons in the vicinity of the EDELWEISS-II Germanium detectors, a full $3D$-simulation of the experiment is mandatory. Therefore not only the EDELWEISS-II experimental setup, composed of the muon veto system, the shielding and the Germanium bolometers, is implemented in the *Geant4* simulations of this work, but also to a lower extent the close vicinity of the experiment and the underground laboratory.

### 5.2.1 LSM experimental hall and muon generator

The cavity of LSM in the simulations is a $10.8 \times 20.0 \times 11.0\ m^3$ volume. Though the orientation of the LSM is based on compass directions, an offset of $\phi = 16°$ towards the east between the laboratory north wall and the geographical north axis is implemented as described in chapter 4.2.
The muon-induced neutron production for high energy muons increases along the shower axis and reaches equilibrium at a column depth $X = \rho \cdot x \gtrsim 800 g/cm^2$. This is discussed in chapter 3.3. For the rock surrounding the Fréjus underground laboratory, as used in the *Geant4* simulations, see table B.3 for the material details, this condition is already fulfilled by $x \approx 3\ m$. Nevertheless, in the simulations of this work, the laboratory cavity is surrounded by $d = 5\ m$ of rock above and on the sides and $d = 2\ m$ below the experiment. This specification ensures to include into the simulations all neutrons from muon-induced reactions in the rock potentially entering the laboratory cavity within a reasonable computation time. Note that high energy neutrons, capable to pass the polyethylene and lead shielding, are strongly correlated with the direction of the initial muon, see chapter 3.6 for details. On this account, less rock is implemented in the simulation setup below the experimental hall. In addition to the surrounding rock, a $d = 5\ cm$

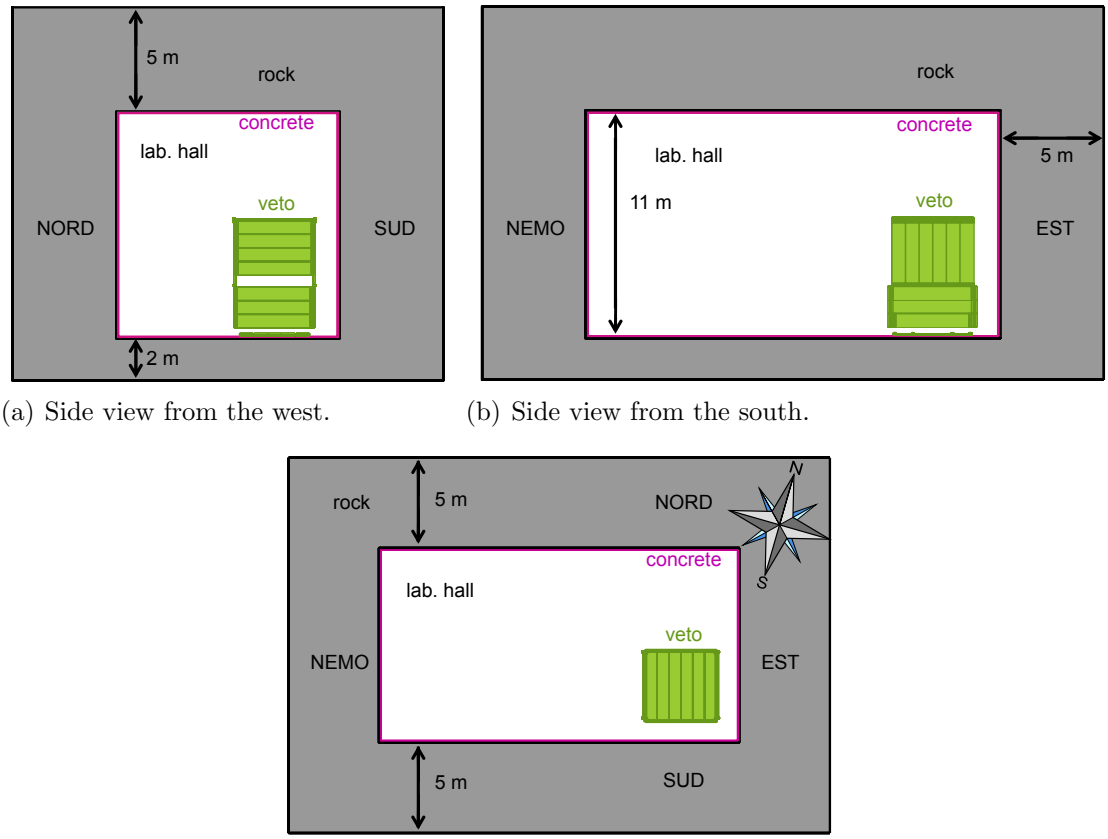


(a) Side view from the west.

(b) Side view from the south.

(c) View from the top, compass indicating geographical directions

**Figure 5.3:** Underground laboratory LSM as implemented in *Geant4* simulations. Side view from the west, i.e. Nemo (a), and from the south, i.e. Sud (b). The experimental setup of EDELWEISS-II is placed in the south-east corner of the laboratory hall of the LSM, as shown in figure (c). The compass indicates the $\varphi = 16°$ offset to the east between the laboratory 'Nord'-wall and the geographical north axis.

thin layer of concrete, see table B.6 for the material details, is covering the walls of the underground cavity in the simulation setup. A graphical overview of the underground laboratory LSM, as implemented in the *Geant4* simulations, is given in figure 5.3. Also shown is the location of the EDELWEISS-II experiment in the experimental hall and the compass directions.

The muons in the *Geant4* simulations are generated according to the energy and angular distribution as discussed in chapter 4.2. The muon energy and the muon momentum direction are chosen by Monte Carlo methods. A reference point is chosen on a hemisphere with radius $r = 30\ m$ around the centre of the EDELWEISS-II experimental setup; note that this is not the centre of the laboratory hall. The radius vector of the reference point is parallel to the chosen

muon momentum direction. A muon starting point is determined by randomisation on the hemisphere until the distance $\delta$ to the reference point is $\delta \leq 5\ m$. With the dimensions of the EDELWEISS-II muon veto system of approximately $4 \times 4 \times 6\ m^3$, i.e. a maximal diameter of $d \approx 8\ m$, a homogeneous exposure of the complete experimental setup is ensured. On the other hand, the number of simulated muons without any direct or indirect interaction, i.e. primary or secondary particle interactions of the muon-induced shower, in the vicinity of the experiment is kept to a minimum. This optimises the computation time of the simulations.

For illustration purposes only, figures 5.4(a) and (b), show the muon-induced neutron production as side projections equivalent to figure 5.3(a) and (c), respectively. The colour scheme correlates to the number of muon-induced neutrons integrated along the projection line, where blue denotes less neutron production vertices per bin, while yellow and red correspond to higher values per bin. The data plotted reflects only a fraction of the total simulated data available ($\approx 3\%$). As can be seen, the neutron production is not equally simulated in the complete experimental hall as implemented in the *Geant4* simulations. To be more specific, figure 5.4(a) shows that more neutrons are created below the experiment than above: The muon flux as previously discussed is focussed to the centre of the experimental setup, i.e. the chosen origin of the coordinate system. Together with the zenith dependence of the muon flux underground, the distribution of neutron production vertices in three dimensions has in principle a conical structure. The conical structure is broadened due to the randomisation of the starting points and centred to the lead shielding and the Germanium detectors as a result of the chosen coordinate system. Assuming a homogeneous volume, e.g. a large volume of only rock, the side projection of the conical distribution would yield a decreasing amount of produced neutrons per bin with increasing distance to the point of origin of the simulation coordinate system. More strictly speaking, taking into account the muon generator, the distribution decreases with the distance to the area of homogeneous exposure around the origin. Applying this principle to the implemented geometry in the simulations of this work, the neutron production decreases with increasing distance to the experimental setup. As illustrated in the figures 5.3 and 5.4, respectively, the rock surrounding the underground laboratory in the simulations is not centred to the chosen coordinate system. As a result, the projected neutron production in figure 5.4, is higher in the rock underneath and on the eastern and southern side of the experimental setup. Despite the observed asymmetry in a side projection, the muon generator exposes the area sufficiently homogeneously around the experimental setup without fading muon fluxes at the geometrical boundaries. This can be concluded by studying the neutron production vertices along the vertical axis, as illustrated in figure 5.4(b). Here, one can clearly see that the neutron production along projection lines with constant density, e.g. the rock on the southern and eastern side of the experiment, is homogeneous in an area around the origin with radius $r = 5\ m$. This corresponds to the aforementioned randomisation $\delta$ of the muon starting points on the hemisphere.

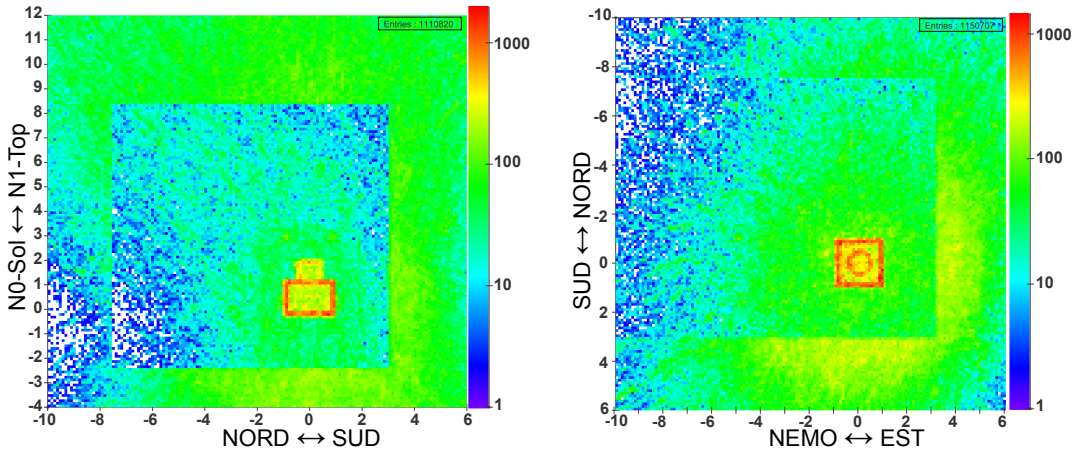


(a) Side projection (b) Vertical projection

**Figure 5.4:** Projections of the simulated muon-induced neutron production in the implemented geometry.(a) represents a side projection from the west and (b) a vertical projection from the top of the experimental hall. Visible is the homogeneous exposure of the experimental setup as a result of the muon generator choices in the simulations. The high neutron production yield in the lead shielding also stands out.

Furthermore, figures 5.4(a) and (b) illustrate the fact that the neutron production in the laboratory hall, as discussed in chapter 3.4, is surpressed by several orders of magnitude, e.g. the density of air is $\rho_{\text{air}} \approx 1.3 \times 10^{-3} g/cm^3$. As a result, the projection of the neutron production vertices at the boundary of the laboratory hall to the rock dramatically changes. Moreover, since the neutron production yield in lead is one order of magnitude higher than in rock, the lead shielding of the EDELWEISS-II setup, as implemented in *Geant4*, is protruding in the figures 5.4(a) and (b). Note that the cubic and cylindrical structure of the 20 *cm* lead shielding in the projection yields even higher neutron production per bin at the edges.

As a summary, the chosen muon generator, though focussed on the centre of the experiment, provides a sufficiently homogeneous exposure. This assumption especially holds for neutrons produced in muon-induced showers. Besides, in approximately one third of the simulated muon events no particle of the shower enters the experimental setup, i.e. the muon veto system. More information on this issue is provided in chapter 6.1.1 and table 6.2.

### 5.2.2 The EDELWEISS-II detectors and shielding

The EDELWEISS-II experimental setup is implemented into the *Geant4* simulations with considerable precision. The veto system consisting of 42 plastic scintillator modules is already described in section 5.1. Additionally, the complete mechanical construction of the veto system including the substructure of the two mobile waggons

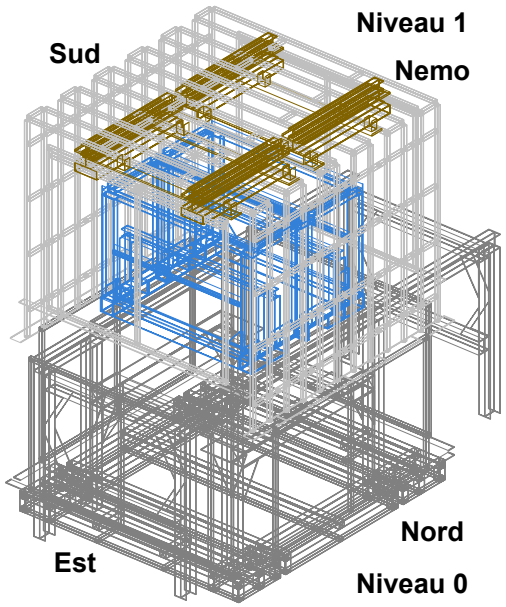


(a) Mechanical structure or 'girder'

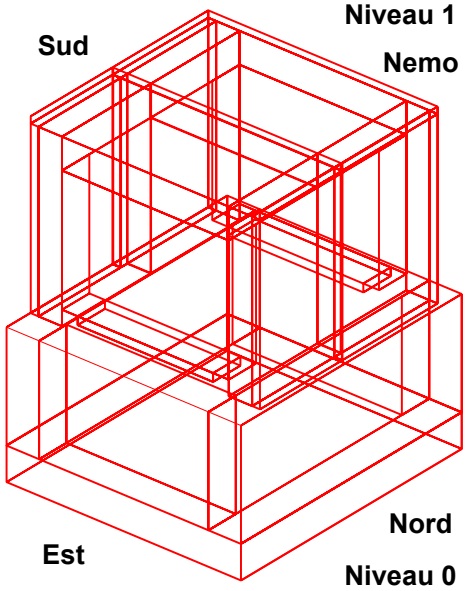


(b) Polyethylene shielding

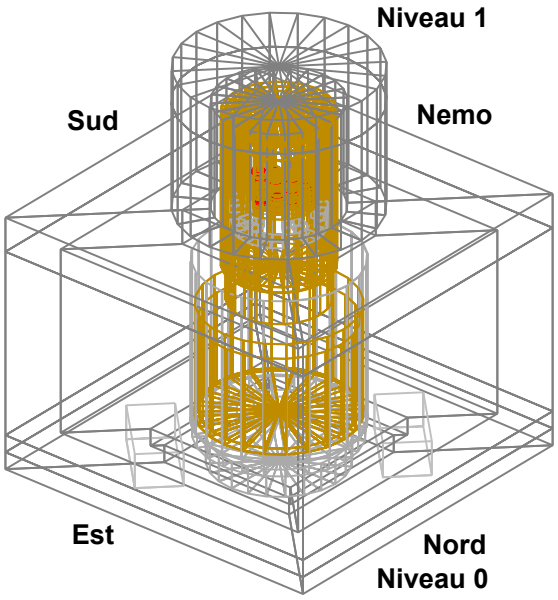


(c) Lead shielding and Copper cryostat

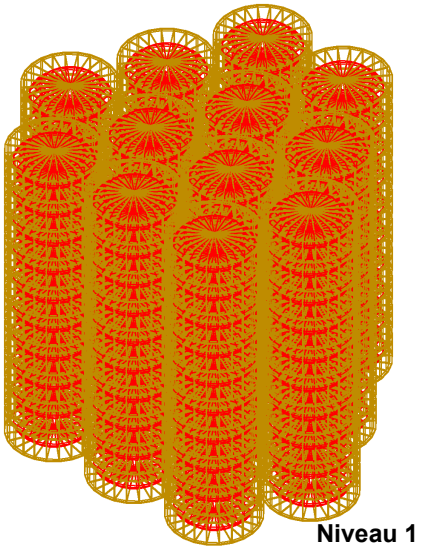


(d) Germanium crystals within cylindrical Copper holders

**Figure 5.5:** The EDELWEISS-II experimental setup as implemented in *Geant4* simulations. (a) shows the complete mechanical construction of the experiment, including the two waggons holding the polyethylene shielding (blue), the substructure of the veto system (grey) and the rails above the polyethylene shielding for the veto waggons (brown). (b) shows the polyethylene shielding only (red). In (c) the lead shielding (grey) around the cryostat (coppery) is illustrated. (d) shows the 120 Germanium crystals (red), on ten levels of twelve each, within individual cylindrical copper holders. Figures (a) - (d) are for illustration purposes and not true to scale.

on Niveau 1 and the sliding rails between the top veto modules and the polyethylene shielding is included. Since the metallic frame construction of the veto system, together with the complete construction design of the EDELWEISS-II experiment, is a non-negligible amount of high-Z material in the vicinity of the Germanium detectors, it is of importance for the investigation of muon-induced neutron production. For instance, the structure supporting the polyethylene and lead shielding on Niveau 0 and the two waggons moving independently from the veto on Niveau 1, altogether form several tons of steel above and in between the shielding material of the detector in form of rods, girders and double-T beams. Figure 5.5(a) shows the complete metallic material as implemented in the simulations.
The polyethylene shielding of the EDELWEISS-II setup is divided into three major parts, the 50 *cm* uniform layer on Niveau 0 and two movable waggons on Niveau 1. The polyethylene on Niveau 0 has the outer dimensions of 404 *cm* (Nord-Sud) × 360 *cm* (Est-Nemo) and a height of 161 *cm*. The waggons on Niveau 1 in the closed position are 353 *cm* (Nord-Sud) × 365 *cm* (Est-Nemo) wide and 279 *cm* high. Due to the mechanical structure on the east- and westward sides between the lower and the upper level polyethylene, an offset towards the center of $\Delta d \approx 25cm$ on each side remains in the closed position. Furthermore, a vertical gap of $\Delta d \approx 10$ *cm* in the polyethylene shielding between the two rails remains to avoid any blockage of the movable structure and to ensure access to the electrical motors moving the two waggons. Figure 5.5(b) shows the polyethylene shielding of the *Geant4* simulations in the closed position.
The 20 *cm* lead shielding of the EDELWEISS-II setup consists of a rectangular lower part and a cylindrical upper part housing the cryostat. The lower part has a quadratic base area with an edge length of 198 *cm* and a height of 148 *cm*. The upper cylindrical part has a diameter of 110 *cm* and a height of 82 *cm*. The implemented geometry includes holes for the cryogenic pumping system on the ground floor. Inside the cryostat the additional archaeological lead shielding is included as well. The cryostat itself consists of three cylindrical layers of copper with diameter 96.8 *cm*, 86.2 *cm* and 82.9 *cm*, respectively, as illustrated in figure 5.5(c).
The Germanium detectors are located in ten layers of twelve detectors each on copper plates with 50.5 *cm* diameter inside the cryostat. Each Germanium detector of 7 *cm* diameter with beveled corners is encased into individual copper casings as illustrated in figure 5.5(d) [Nol06].

## 5.3 Geant4 simulation results

Again, several millions of muons are simulated within the complete geometry as described in the previous section. The muons are generated in the energy range of $200 < E_\mu < 2000$ *GeV* according to the energy and angular distribution of the muon flux in the underground laboratory, see chapter 4.2. The simulated energy range represents only $\sim 35\%$ of the total muon flux; this issue is discussed in chapter 6. *Geant4* version 8.2.p01 with the physics list and the production cuts, as discussed in chapter 3.2 is used. The normalisation of the simulations

| condition | exp. data rate @ LSM $[d^{-1}]$ | *Geant4* geom. rate $[d^{-1}]$ |
|---|---|---|
| N1Top - N0 | $12.7 \pm 0.2$ | $12.0 \pm 0.3$ |
| N1Nord - N0 | $5.9 \pm 0.2$ | $7.0 \pm 0.2$ |
| N1Sud - N0 | $8.0 \pm 0.2$ | $6.2 \pm 0.2$ |
| N1Nemo - N0 | $5.1 \pm 0.1$ | $3.4 \pm 0.1$ |
| N1Est - N0 | $3.2 \pm 0.1$ | $2.4 \pm 0.1$ |

**Table 5.3:** Comparison of preliminary data of the EDELWEISS-II muon veto system with *Geant4* simulations for various geometrical coincidence conditions. The data corresponds to a total of 8475 muon candidates recorded in an effective measuring time of $t = 243$ $d$. The errors for the simulation results are dominated by the error on the measured muon flux, see (4.18).

to the measured muon flux is done by an arbitrary horizontal area. Taking into account the considerations discussed in section 5.2.1 on the muon generator in the simulations, a homogeneous exposed area has to be chosen. In fact, the dividing line between Niveau 0 and Niveau 1 of the experimental setup enclosed by the veto system denominates a horizontal normalisation area of $A \approx 15$ $m^2$. The muon flux is measured by the Fréjus experiment for a horizontal area at the LSM to $\Gamma_\mu = 4.73 \pm 0.1$ $m^{-2}d^{-1}$ [Ber89], please refer also to the discussion in chapter 4.2.

### 5.3.1 Geometrical muon rates

As already discussed in chapter 4.3, first preliminary data are available for the EDELWEISS-II muon veto system. At this, muon event candidates are defined as coincidental energy deposits in one module, or several modules respectively, of different sides of the veto system. Together with the *Geant4* simulations of the muon flux in the underground laboratory, see chapter 4.2, the geometrical fraction of muon events for the conditions applied to the experimental data can be determined.
In general, a module hit is defined as a coincidence of the signals collected by the photomultipliers at each end of the module above the discriminator threshold [Cha07b]. Further on, coincidences of module hits on different sides of the veto system are predominantly caused by muons traversing the experimental setup and thus are considered as muon candidates. Due to the expected very low muon rate and the strong zenith dependence of muons at LSM, first of all, coincidences in any module on the top of the scintillator system, i.e. in module $1 - 6$ (N1-Top), are studied. Applying this condition in an off-line analysis on data acquired over a period of 15 months, corresponding to an effective measuring time of $t = 243$ $d$ live-days, a set of 3084 muon candidates are found. The corresponding muon rate, representing only a fraction of the total muon rate, is $\Gamma_{\text{N1Top-N0}} = 12.7 \pm 0.2$ $d^{-1}$. The preliminary energy distribution in ADC-channels for this set of muon candidates together with the Landau-fit is shown in figure 5.6.

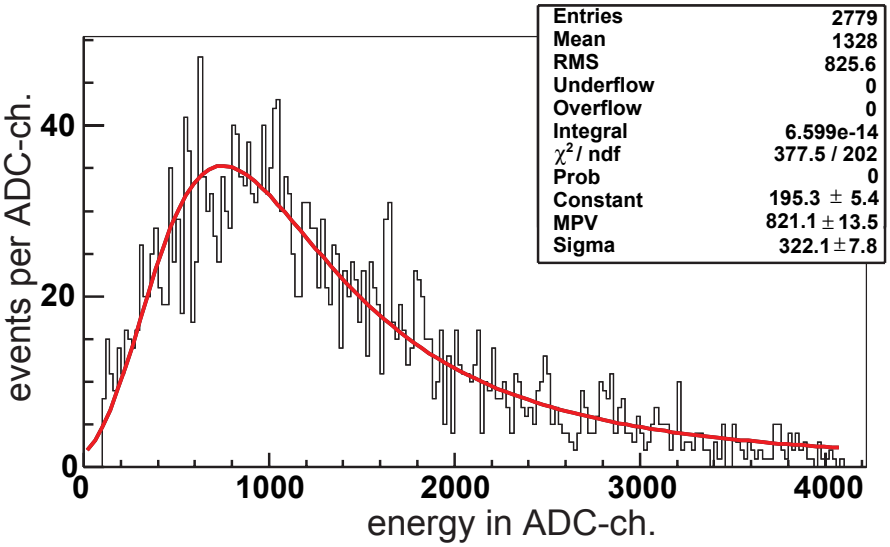


**Figure 5.6:** Preliminary experimental data of the EDELWEISS-II muon veto system showing the energy distribution of muon candidates and a Landau fit (red). The coincidence condition is N1Top-N0, see text for details. Note that 305 out of 3084 $\mu$ candidates have energy deposits higher than the ADC range (ADC overflows).

The *Geant4* simulation data is studied in a corresponding way. Thereby a module hit is defined as a total energy deposit of $E_{\text{dep}} > 2\ MeV$, according to the aimed energy threshold for the muon veto system [Hab04]. The rate determined in Monte Carlo simulations, normalised to earlier measurements, is $\Gamma^{\text{G4}}_{\text{N1Top-N0}} = 12.0 \pm 0.2\ d^{-1}$. The analysis method can be performed for various veto conditions, for example, the side walls of the upper level of the veto system in coincidence with modules on the lower level, e.g. N1Nord - N0, etc. However, the experimental measured data so far, for instance in eastern and western direction, is limited to only several hundred muon candidates. An overview of the comparison of experimental rates with *Geant4* simulations is given in table 5.3. The results at present are preliminary and possible deviations between the experimental data and the ones deduced by Monte Carlo simulations are going to be studied in more detail. Besides investigations on the performance of all modules during data acquisition, the next steps in the ongoing data analysis of the EDELWEISS-II muon veto system are to reconstruct tracks of muons using the internal veto timing and to investigate coincidences of bolometer events with the muon veto system [Chaon].

### 5.3.2 Total energy deposit per module

The total energy deposit in the plastic scintillator modules is shown in figure 5.7(a), exemplary for the top modules. Herein the discussed Landau spectrum, as a result of penetrating high energetic muons, is clearly visible. However, not only muons deposit energy in the scintillator modules. While traversing the $d = 5\ m$ of rock above the

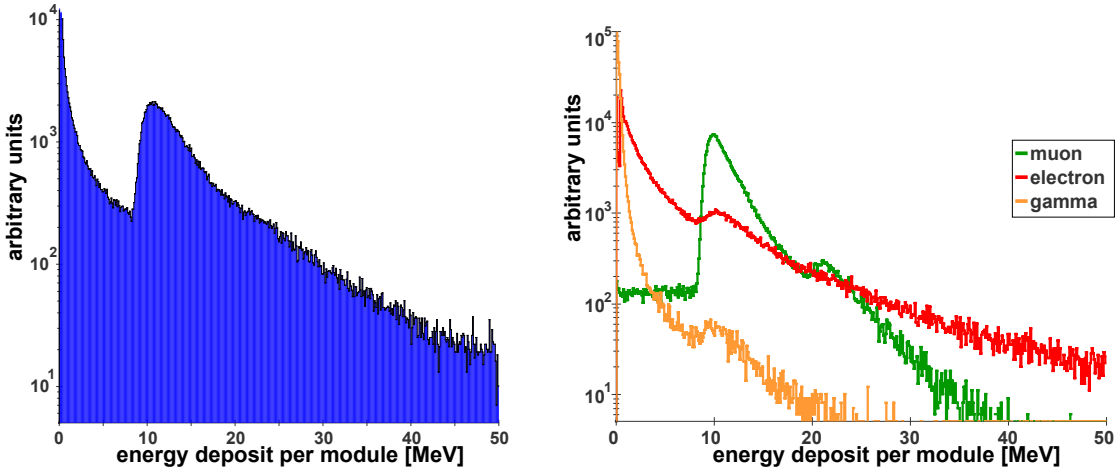


(a) Total energy deposit $E_{\text{dep}}^{\text{tot}}$

(b) $E_{\text{dep}}$ of $\mu$, $e^-$ and $\gamma$

**Figure 5.7:** (a): Simulated total energy deposit per horizontal module, i.e. N1-Top. (b): Energy deposit per module associated to muons (green), electrons (red) and photons (yellow). See text for details.

experimental hall, the muon develops an electromagnetic shower. I.e., relativistic muons lose energy in matter primarily by ionisation and atomic excitation, and thus produce electrons and photons. Photons of sufficiently high energy interact with matter mainly via pair production, i.e. they convert into electron-positron pairs. The electrons and positrons in turn emit bremsstrahlung photons. The two processes continue to take place alternately until the particle energies are below the production threshold.

The energy deposit associated to the individual particle types, namely the incident muons, the electrons and the photons of the shower, are shown in figure 5.7(b). For the muon spectrum, the energy deposits of less than $E_{\text{dep}}^{\mu} = 10\ MeV$ result from muons streaking the corners of the scintillator modules. The second peak, around $E_{\text{dep}} \approx 22\ MeV$, arises from the increased thickness of the plastic scintillator modules at the end due to the light guides. See [Rei98] for a detailed discussion of these effects. The mean value for muons on horizontal modules is $\left\langle E_{\text{dep}}^{mu} \right\rangle = 11.8\ MeV$, see section 5.1.1.

High energy vertical electrons, akin to muons, are traversing the $d = 5\ cm$ of plastic scintillator by depositing $E_{\text{dep}}^{e^-} \approx 10 - 12\ MeV$. The electrons in the electromagnetic shower induced by the muon in the rock overburden lose energy primarily via scattering processes and thus account for the exponential rise in the energy deposit spectrum.

The energy deposit associated to photons is dominated by the photo-electric effect, although Compton scattering, Raleigh scattering and photo nuclear absorption also contribute. Again, the curve shows an exponential rise towards low energy deposits in the scintillator module.

The main purpose of the EDELWEISS-II plastic scintillator system is to detect muons. However, the energy deposit of secondary particles of a muon induced electromagnetic shower well beyond the aimed threshold of $E_{\mathrm{dep}} = 2\ MeV$ offers the possibility to increase the muon detection efficiency. In principle, detecting high energetic secondary particles in the veto system can be associated with a muon passing nearby the veto system. In the next chapter, the increase in muon detection efficiency by the detection of only secondary shower particles in coincidence with bolometer events is studied.

# 6 Muon veto efficiency for coincident bolometer events

As shown in the last chapter, the geometrical efficiency of the muon veto system for the EDELWEISS-II experiment can be estimated to $\epsilon_{\text{geom}} = 98.2\%$. In this chapter, the efficiency to veto bolometer events induced by cosmic ray muons in an end-to-end Monte Carlo simulation is studied for the first time. First, the energy deposit in the Germanium bolometers by the electromagnetic and hadronic shower of the incident muon is investigated. The focus at this is set to neutrons with sufficiently high kinetic energies able to produce nuclear recoils above an energy threshold for the bolometers. Secondly, coincidences between energy deposits in the bolometer and the muon veto system are inquired and the remaining bolometer event rate determined. Finally, the efficiency of the veto system in terms of tagging muon events in coincidence with nuclear recoils is discussed. Besides, the possibility to increase the muon detection efficiency beyond the veto efficiency by an ascertained muon detection is studied. In principle, taking into account energy deposits in the veto modules above threshold by high energy secondary particles of electromagnetic showers induced by cosmic ray muons can increase the effective detection area for muons.

## 6.1 Muon-induced background in the EDELWEISS-II bolometers

High energetic muons passing through matter induce electromagnetic and hadronic showers, as described in chapter 3. In the hadronic particle cascade initialised by nuclear reactions, e.g. muon deep inelastic scattering or photo nuclear reactions, neutrons with energies of more than $E_n > 100\ MeV$ are produced. These neutrons can potentially penetrate the hydrogen-rich shielding material of the EDELWEISS-II experiment and eventually interact with the Germanium of the bolometers. The energy of the recoiling Germanium nuclei can thereby be of the same order as the recoil energy of WIMP-nucleus interactions. In this section, after a short discussion about the used muon energy range in the *Geant4* simulations, an estimated event rate in the Germanium crystals by muon induced showers is determined and the deposited energy of neutrons in the bolometers is studied.

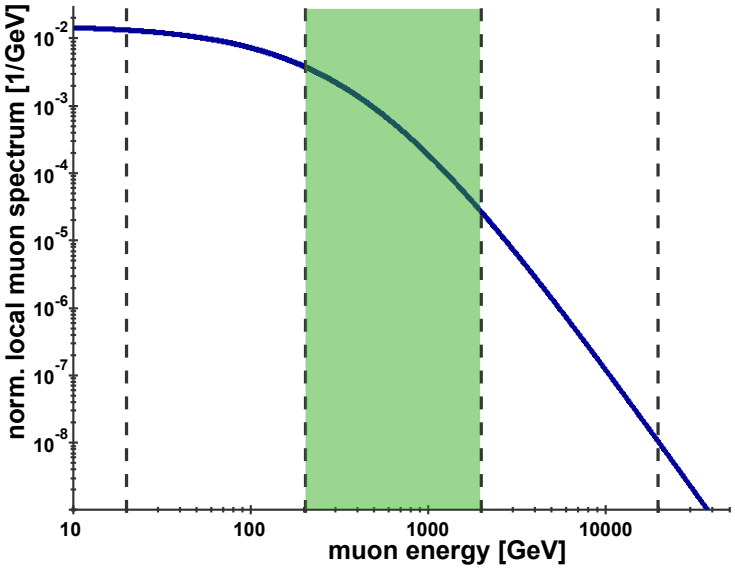


**Figure 6.1:** Muon Flux in the underground laboratory LSM as a function of muon energy normalised to unity. The muon flux in the energy range $200 - 2000\ GeV$ (shaded area) corresponds to 35% of the total muon flux. For corresponding values of other energy decades see table 6.1.

### 6.1.1 Muon energy considerations for the simulations

As mentioned previously, neutrons are produced in the surrounding rock by muon-induced particle showers. Neutrons with high kinetic energies potentially penetrate the shielding of the EDELWEISS-II experimental setup leading eventually to nuclear recoils above threshold in the Germanium crystals. The attenuation length for fast neutrons, e.g. $E_n > 100\ MeV$, in hydrogen-rich material, e.g. water, $H_2O$, or hydrocarbon, $C_nH_{2n}$, is in the order of $\lambda \approx 10 - 20\ cm$. For completeness, the diffusion length for thermal neutrons, i.e. the mean distance low energy neutrons pass before absorption, is of the order of only a few centimeters ($d \lesssim 5\ cm$). In case of elastic nuclear scattering reactions, for example between a neutron and a Germanium nucleus, the recoil energy of the nucleus can be written as:

$$E_{\mathrm{rec}} = \frac{q^2}{2M} \tag{6.1}$$

with the momentum transfer $q = 2\mu v \cos\theta$ and the reduced mass $\mu = \frac{m \cdot M}{m+M}$; $m$ and $M$ are the projectile and target nucleus mass, respectively. The maximal recoil energy for neutrons, $m_n \approx 1\ GeV$, with kinetic energy $E_n$ on Germanium nuclei, $M_{\mathrm{Ge}} \approx 73\ GeV \gg m_n$ can be approximated as:

$$E_{\mathrm{rec}}^{\mathrm{max}} \simeq E_n \times \frac{4}{M_{\mathrm{Ge}}} \simeq 0.05\ E_n \tag{6.2}$$

Hence, neutrons with kinetic energies of about $E_n \gtrsim 0.2\ MeV$ are necessary

| value | $20 < E_\mu < 200\ GeV$ | $200 < E_\mu < 2000\ GeV$ | $E_\mu > 2000\ GeV$ |
|---|---|---|---|
| $\langle E_n \rangle$ | $\approx 50\ MeV$ | $\approx 60\ MeV$ | $\gtrsim 65\ MeV$ |
| $\Phi_\mu / \Phi_{\mathrm{tot}}$ | 52% | 35% | $< 1\%$ |
| $\langle E_\mu \rangle$ | $\approx 30\ GeV$ | $\approx 300\ GeV$ | $\gtrsim 3000\ GeV$ |
| $\Upsilon(\langle E_\mu \rangle)$ | $\approx 4.5 \times 10^{-5}$ $n/\mu/(g/cm^2)$ | $\approx 22.8 \times 10^{-5}$ $n/\mu/(g/cm^2)$ | $\approx 110 \times 10^{-5}$ $n/\mu/(g/cm^2)$ |
| $\Xi / \Xi_{\mathrm{med}}$ | $\approx 0.3$ | 1 | $\lesssim 0.1$ |

**Table 6.1:** Relative contribution of different energy ranges to the overall muon flux in the underground laboratory LSM and the weighted neutron production yield with respect to the medium energy range. See text for details.

to cause nuclear recoils in the order of $E_{\mathrm{rec}} \sim 10\ keV$ in central collisions on Germanium nuclei. As discussed briefly in chapter 3.5, the kinetic energy spectrum of neutrons produced in muon-induced hadronic showers depends only weakly on the kinetic energy of the incident muon.

The muon flux in the underground laboratory LSM as a function of energy, as discussed in chapter 4.2 is shown in figure 6.1 in a smaller muon energy range than in figure 4.1. Indicated in this figure are three different decades of the muon energy, namely $20 < E_\mu < 200\ GeV$, $200 < E_\mu < 2000\ GeV$ and $2 < E_\mu < 20\ TeV$. Though the majority of the muon flux in the underground laboratory corresponds to energies below $200\ GeV$, and the spectrum also continues beyond $2\ TeV$, muon energies are simulated in this work mainly for $200 < E_\mu < 2000\ GeV$. This energy range is chosen according to the following considerations: First, the simulation results concerning the neutron production yield and kinetic energy spectrum, as discussed in chapter 3, show that the neutron yield produced in the surrounding rock is increasing exponentially with increasing $E_\mu$. Assuming a simple power law for the neutron production yield in matter as a function of mean muon energy, $N_n(\langle E_\mu \rangle) \equiv \Upsilon(\langle E_\mu \rangle) = A_n \cdot \langle E_\mu \rangle^{\gamma_n}$, see equation (3.4), and a muon energy spectrum $dN_\mu / dE_\mu \equiv \Phi = A_\mu \cdot E_\mu^{-\gamma}$ with a spectral index $\gamma = 3.7$, see equation (4.10), the neutron production yield can be weighted with the muon energy spectrum. The respective weighted neutron production yields per unit muon track length, $\overline{\Phi\Upsilon} \equiv \Xi$, normalised to the value corresponding to the medium muon energy range, i.e. $200 < E_\mu < 2000\ GeV$, can be estimated for the according energy ranges. As a result, the neutron production yield in the lower energy range, i.e. $20 < E_\mu < 200\ GeV$, represents only about $\sim 30\%$ of the one simulated in the medium energy range. The weighted neutron production yield for very high muon energies, i.e. $E_\mu > 2\ TeV$ is suppressed by one order of magnitude. The approximated values are summarised in table 6.1.
With the goal to study very rare events with very high precision Monte Carlo simulations, e.g. nuclear recoils of muon-induced neutrons, certain limitations on the computation time have to be made. Since the muon energy spectrum follows a very steep power law with a spectral index of $\gamma \sim 2.7 - 3.7$, obtaining

| | | $20 < E_\mu < 200 GeV$ | $200 < E_\mu < 2000 GeV$ |
|---|---|---|---|
| $\mu$ events | $N$ | $4.2 \times 10^6$ | $\sim 2.8 \times 10^7$ |
| eff. exposure | $E$ (norm. to [Ber89]) | $\sim 70\ y$ | $\sim 430\ y$ |
| CPU time | $t$ (AMD$^{\text{TM}}$2.4$GHz$) | $\sim 65\ d$ | $\sim 700\ d$ |
| evts in veto | $N^{\text{veto}}(E^{\text{veto}}_{\text{dep}} > 0)$ | $\sim 2.2 \times 10^6$ (53%) | $\sim 1.7 \times 10^7$ (60%) |
| $\mu$ in veto vol. | $N^{\text{veto}}_{\mu}(\mu \text{ in } V^{\text{veto}})$ | $\sim 1.5 \times 10^6$ (35%) | $\sim 9.8 \times 10^6$ (35%) |
| hits in Ge | $N^{\text{Ge}}(E^{\text{Ge}}_{\text{dep}} > 1keV)$ | $\sim 4.9 \times 10^4$ (1%) | $\sim 8.7 \times 10^5$ (3%) |
| nucl.rec. hits | $N^{\text{Ge}}_{\text{rec}}$(RoI) | $\sim 4.1 \times 10^3$ (0.1%) | $\sim 1.7 \times 10^5$ (0.6%) |
| background | $N_{\text{bg}}(E^{\text{veto}}_{\text{dep}} > 2MeV)$ | $= 16$ ($\sim 4 \times 10^{-6}$) | $= 87$ ($\sim 3 \times 10^{-6}$) |

**Table 6.2:** Overview of the *Geant4* simulations of this work in the complete $3D$ EDELWEISS-II geometry.

commensurate statistics for all energies can only be achieved by biasing the simulated muon flux. Hence, the simulations have been performed separately in two muon energy ranges: The majority of the simulation data corresponds to muon energies between $200 < E_\mu < 2000\ GeV$; data with less statistics is also available in the lower energy range, i.e. $20 < E_\mu < 200\ GeV$. However, no considerable amount of simulation data has been collected for muon energies $E_\mu > 2\ TeV$ due to the previously discussed weighted neutron production yield and the extremely long computation time of high energy muon transport through the complex $3D$ geometry implemented in *Geant4*. An overview of the simulation data is given in table 6.2. Note that predictions on the neutron yield obtained by simulations over a fraction of the muon energy range, e.g. the medium energy range, and normalised to the total muon flux, with the appropriate scaling, in principle conservatively overestimates the neutron yield and thus the expected background rate in the other energy ranges. The results of the simulations, as discussed in the following sections are based on the simulations performed in the muon energy range of $200 < E_\mu < 2000\ GeV$ with appropriate annotations on the lower muon energy range.

### 6.1.2 Muon-induced bolometer events

In the simulation setup, as discussed in chapter 5.2, 120 identical Germanium bolometers are implemented. The simulations are performed with *Geant4* `8.2.p01`. In total more than 32 million muons are simulated; about four million muons are simulated with muon energies in a lower muon energy range between $20 < E_\mu < 200\ GeV$ and about 28 million muons in the muon energy range between $200 < E_\mu < 2000\ GeV$. The total energy deposit in the bolometers is shown on a logarithmic scale in figure 6.2. In this figure, the logarithmic scale on the x-axis and the consequently logarithmic bin sizes can be confusing, but serves the illustration purposes. For instance, muons passing eventually through the bolometers deposit energy according to the approximation given by equation (A.4) of Appendix A.

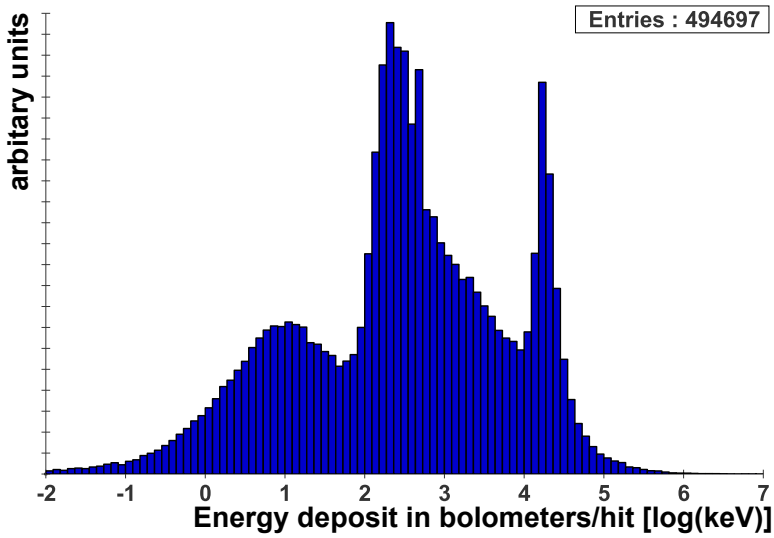


**Figure 6.2:** The simulated total energy deposit in Germanium bolometers of the EDELWEISS-II experimental setup.

Together with the density of Germanium $\rho_{\mathrm{Ge}} = 5.31\ g/cm^3$, the energy deposit of vertical muons is about $E_{\mathrm{dep}} \approx 20\ MeV = 2 \times 10^4\ keV$. This results in a clearly visible peak in figure 6.2. Energy deposits in the range of $10^2 < E_{\mathrm{dep}} < 10^4\ keV$ are dominantly caused by photon or electron interactions. At this, the most prominent feature, besides the $E = 511\ keV$-line from $e^+e^-$-annihilation inside or in the close vicinity of the bolometers, is the so-called 'Compton backscattering-bump' around $E_{\mathrm{dep}} \approx 200\ keV$. This experimentally proven feature can be attributed to photons of energy $E_\gamma = 511\ keV$, as produced in electron-positron annihilations, losing approximately 2/3 of their energy in Compton scattering processes[1] in the Copper holders surrounding the bolometers and scatter back into the bolometers [Fio07]. Energy deposits below $E_{\mathrm{dep}} < 50\ keV$ are predominantly produced by nuclear interactions. According to equation (6.1) defining the energy transfer to the bolometers, energy deposits can in principle be as low as a few tens of $eV$. Figure 6.3 shows the same simulated energy deposit on a linear scale in the range of $1 < E_{\mathrm{dep}} < 1000\ keV$. The data is shown in units normalised to the measured total muon flux in the underground laboratory LSM, i.e. hits per crystal in $[keV^{-1}d^{-1}]$; please refer to chapter 4.2 for a discussion of the muon flux at the LSM. Clearly visible in this representation is the aforementioned Compton backscattering bump around $E_{\mathrm{dep}} \approx 200\ keV$ and the $E = 511\ keV$ line.

The energy deposit in the bolometers, determined by the particle interaction can be assigned in the analysis of the simulation data to either electron recoils, e.g.

[1] The amount of energy transferred of an incident photon to the electron varies with the angle $\theta$ of deflection. The maximum amount of energy is transferred for $\theta = 180°$ and is determined as $E_{\mathrm{Compton}} = E\frac{2E}{m_e c^2 + 2E}$.

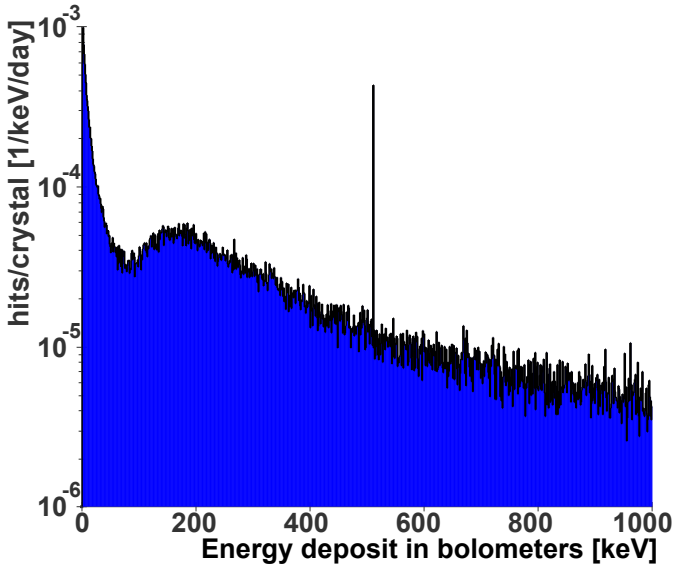


**Figure 6.3:** The simulated total energy deposit in Germanium bolometers of the EDELWEISS-II experimental setup normalised to the measured total muon flux at the LSM.

induced by electron and photon interactions, or nuclear recoils, e.g. induced mainly by neutrons but also light hadrons or heavier ions, see figure 6.4(a). The fraction of nuclear recoils to the total energy deposit, falls exponentially towards higher energy deposits. This is anticipated by the steep differential kinetic energy spectrum of neutrons, see also chapter 3.5, together with equation (6.1).

The energy deposit spectrum of electron recoils shows the previously discussed Compton backscattering bump. Though, the spectrum for decreasing energy deposits is expected to increase, the simulated energy deposits in the bolometers by electron recoils levels off below energies of around $E_{\mathrm{dep}} \lesssim 50\ keV$. This is a consequence of the production thresholds implemented in the *Geant4* simulations, as discussed in chapter 3.2.4. Electrons and photons are only produced above a given energy threshold. In *Geant4* this value of cut is given as a cut in range. The corresponding values for the materials used in the simulations are given in table 3.2. As a result of these simulation cuts, very low energy secondaries, potentially leading to additional low energy deposits, are not produced in the simulations. These particles, in principle produced in the close vicinity of the crystals, are hence not tracked and the associated energy is not assigned to the bolometer volume. Note that contrary to electrons and photons, no production thresholds are applied to hadronic particles.

The simulated energy deposit in the Germanium crystals is related to the corresponding heat and ionisation signal of the EDELWEISS bolometers. Following [Mar04b], the relation between the values of $E_I$, $E_H$ and $E_R \equiv E_{\mathrm{dep}}^{\mathrm{sim}}$ is given by equation (2.5), as discussed in chapter 2.1.1. In the analysis of the simulation data, one can at first assume a quenching factor $Q = 1$ for electron recoils and an appropriate

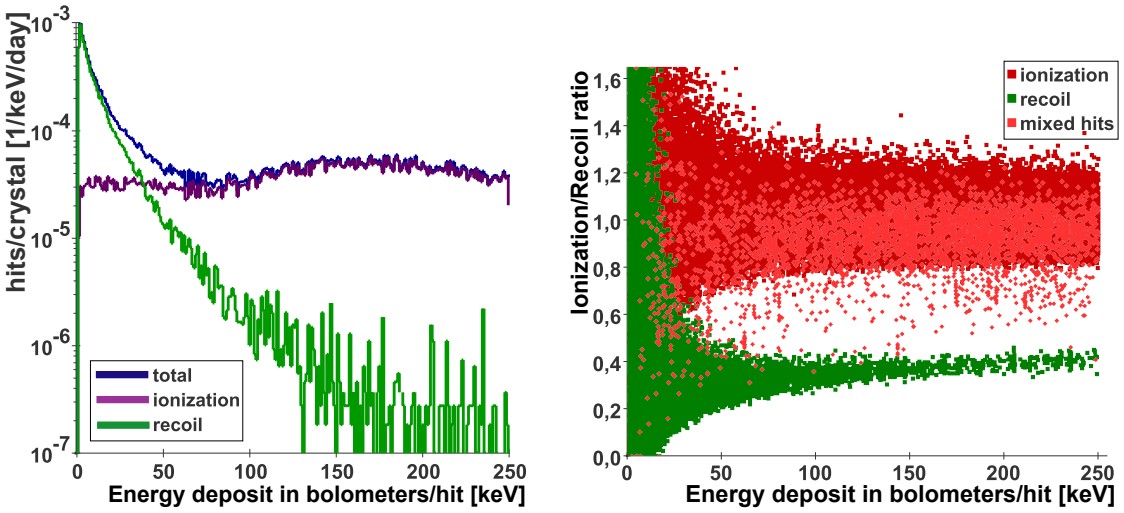


(a) Hits per crystal (b) $Q$-plot

**Figure 6.4:** Simulated energy deposit spectrum in Germanium bolometers as a result of muon-induced electromagnetic and hadronic showers. (a): The total energy deposit (blue) can be assigned to electron recoils by electrons and photons (green) and nuclear recoils mainly by neutrons (purple). (b): Corresponding $Q$-plot of the simulated events. See text for details.

nuclear quenching factor $Q < 1$, as parametrised in equation (2.7). Furthermore, the respective value of $E_I$ and $E_H$ can be randomised by a Gaussian distribution according to the equations (2.8) and the parameters given in [Mar04b]. As a result, the simulated events can be displayed in the $(E_R, Q)$ plane for illustration purposes only, see figure 6.4(b). In this connexion, simulated events with energy deposits by nuclear recoils within a Germanium crystal can, in principle, be accompanied by low energy electron recoils. Consequently, the corresponding randomised $Q$-values for these 'mixed' events are potentially leaking out of the defined band structures, as indicated in figure 6.4(b). However, this occurs only in $\lesssim 0.3\%$ of the events.

### 6.1.3 Nuclear recoils by muon-induced neutrons

As discussed in the previous section, nuclear recoils in the Germanium bolometers in muon-induced hadronic showers are predominantly caused by neutrons, i.e. $\approx 95\%$ of the simulated nuclear recoil events are correlated to neutron interactions in the bolometer. Light fragments and heavy ions produced in inelastic scattering events in the electromagnetic or hadronic shower are involved in the remaining $\approx$ 5% of nuclear recoil events. In the simulation data, a neutron interacting in the bolometer can be traced back to its production vertex. For neutrons interacting in the bolometers with a registered energy deposit of $E_{\mathrm{dep}} > 1\ keV$ the production vertices are shown in figure 6.5. The same colour scheme as in figure 5.4 is used. As can be seen, the neutrons leading to energy deposits in

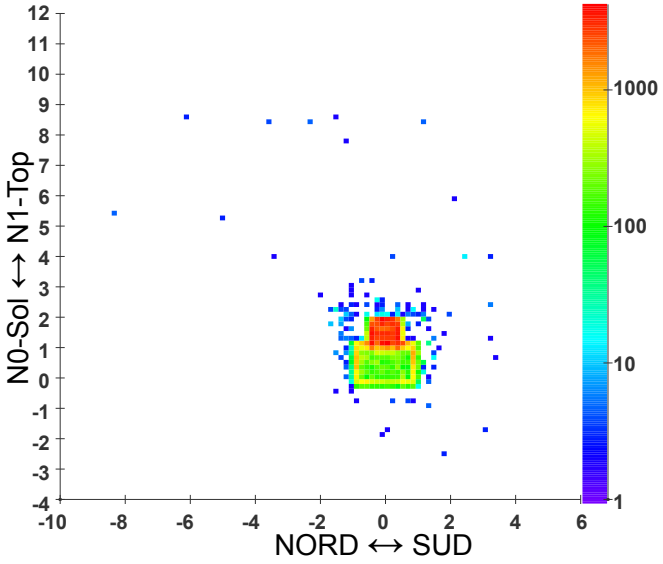


**Figure 6.5:** Production vertices of neutrons in muon-induced showers leading to an energy deposit by nuclear recoils of $E_{\mathrm{dep}} > 1\ keV$ in the bolometers. Shown is a side projection of the underground laboratory LSM, as in figure 5.4

the Germanium crystals are mainly produced in the lead shielding with very few neutrons originating from the rock surrounding the experimental hall. In fact, only a fraction $N^{\mathrm{rec}}_{\mathrm{rock}}/N^{\mathrm{rec}}_{\mathrm{total}} = 4.8 \pm 0.5 \times 10^{-4}$ of the total amount of recoil events $N^{\mathrm{rec}}_{\mathrm{total}}$ are associated with neutrons produced in the rock. Note that this fraction drops approximately by a factor of $\sim 3$ for muon energies below $E_\mu < 200\ GeV$.

In total, the accumulated simulation data corresponds to an effective exposure time in the underground laboratory of $t \approx 160\ 000\ d \approx 400\ y$ in the energy range of $200 < E_\mu < 2000\ GeV$ and around $t_{\mathrm{low}} \approx 70\ y$ in the lower energy range of $20 < E_\mu < 200\ GeV$. The simulation setup consists of 120 Germanium crystals of 320 $g$ each. Thus, the simulated bolometer events correspond to a nuclear recoil rate of muon-induced neutrons of:

$$\Gamma^{\mathrm{n}} \leq 2.6 \times 10^{-2}\ kg^{-1} \cdot d^{-1} \tag{6.3}$$

Taking into account also light fragments and heavier ions, the corresponding rate increases by $\approx 5\%$ to:

$$\Gamma_{\mathrm{rec}} \leq 2.8 \times 10^{-2}\ kg^{-1} \cdot d^{-1} \tag{6.4}$$

For both rates the statistical errors are less than $\sim 1\%$ and thus negligible. The background rate given as an upper limit reflects the considerations of the simulated muon energy range leading to a slight overestimation, as discussed in section 6.1.1. In the simulated geometry, on average $\sim 5-6$ bolometers simultaneously record an energy deposit. This is explained by the compact arrangement of the 120 crystals in

the cryostat and the high probability of multiple neutron interactions. The number of bolometers recording an energy deposit above threshold in a single muon event is called the multiplicity $m$. About $\sim 80\%$ of the simulated recoil events have $m > 1$. For the EDELWEISS-II Dark Matter search, in principle events with multiple hits are not considered as possible WIMP-nucleus interactions and are rejected. Therefore, the background rate of muon-induced nuclear recoils in the EDELWEISS-II experiment, as simulated with *Geant4*, can be approximated as:

$$\Gamma_{\mathrm{bg}} \lesssim 4.5 \times 10^{-3}\ kg^{-1} \cdot d^{-1} \tag{6.5}$$

where the majority of recoils can be accounted to neutrons.
Despite the applied approximations, the muon-induced neutron background would limit the sensitivity of the EDELWEISS-II Dark Matter search. However, the used threshold on the energy deposit in the bolometers of $E_{\mathrm{dep}} = 1\ keV$ is very optimistic. On the other hand, the assumed ideal separation of electron and nuclear recoil is not expected for the Germanium detectors, as shown in figure 6.4(b) and discussed in chapter 2.

To summarise, the *Geant4* simulations of the EDELWEISS-II experimental setup, together with the muon flux in the underground laboratory LSM, describe the muon-induced neutron background reasonably well within the given approximations and model uncertainties. As a result, the new shielding concept with the 50 *cm* of polyethylene and 20 *cm* of lead is suppressing the muon-induced neutron flux from the rock of the laboratory walls leading to energy deposits in the bolometers to:

$$\Gamma^{\mathrm{G4}}(\mathrm{rock}) \leq 1.4 \times 10^{-5}\ kg^{-1} \cdot d^{-1} \tag{6.6}$$

The discussed background rates can be compared to results obtained by previous *Geant3* simulations by [Cha04]. The rates are determined for neutrons of kinetic energy $E_n > 500\ keV$ interacting with Germanium detectors in a more simplified geometry and divided according to the production vertices of the neutrons:

$$\Gamma_{\mathrm{n}}^{\mathrm{G3}}(\mathrm{Pb}) = 5.5 \pm 0.8 \times 10^{-3}\ kg^{-1} \cdot d^{-1}$$
$$\Gamma_{\mathrm{n}}^{\mathrm{G3}}(\mathrm{rock}) = 6.2 \pm 0.9 \times 10^{-3}\ kg^{-1} \cdot d^{-1}$$

Also given are the event rates of single bolometer hits, i.e. an energy deposit is only recorded in one out of 120 crystals, thus multiplicity $m = 1$:

$$\Gamma_{\mathrm{bg}}^{\mathrm{G3}}(\mathrm{Pb}; m = 1) = 0.3 \pm 0.2 \times 10^{-3}\ kg^{-1} \cdot d^{-1}$$
$$\Gamma_{\mathrm{bg}}^{\mathrm{G3}}(\mathrm{rock}; m = 1) = 2.8 \pm 0.6 \times 10^{-3}\ kg^{-1} \cdot d^{-1}$$

Although the total muon-induced neutron event rate is approximately of the same order, i.e. $\Gamma_{\mathrm{n}} \sim \mathcal{O}(10^{-2})$ and $\Gamma_{\mathrm{bg}} \sim \mathcal{O}(10^{-3})$, the neutron flux from the surrounding rock is by two orders of magnitude higher in *Geant3* than in the simulations of this work. A possible reason for this large deviations could be the description of hadronic muon interactions in the different simulation codes. It is well established that

the realisation of photo nuclear interactions in *Geant3* disagrees significantly with theoretical calculations, as discussed in [Bat97] and references therein. Corrections to the total muon nuclear cross section to match theoretical calculations done by [Bez81] were made in [Cha04]. However, no information is given about the angular correlation of the neutrons produced in the shower. As shown in chapter 3.6, in *Geant4* a strong correlation of high energetic secondary neutrons with the incident muon is given. In spite of the constraints on the muons generated, e.g. reducing the amount of simulated muon events with no impact to the experimental setup, the neutrons produced in the rock outnumber the ones produced inside the laboratory hall by many orders of magnitude. However, these neutrons are predominantly moderated to thermal energies and consequently absorbed in the shielding materials of the EDELWEISS-II experimental setup. As a result, the rate of neutrons originating from the rock and interacting in the Germanium is suppressed as previously discussed.

In spite of the shielding material, the remaining nuclear recoils in the bolometers by muon-induced hadronic showers would limit the envisaged sensitivity of the EDELWEISS-II experiment. A reduction of this background rate by studying coincident energy deposits in the muon veto system is therefore mandatory and is done in the following section.

## 6.2 Muon veto and bolometer coincidences

One of the main features of the EDELWEISS-II experimental concept is the integration of a muon veto system. The purpose of this veto system, as discussed in chapter 2.2.2, is to correlate nuclear recoils in the Germanium crystals with cosmic ray muons as detected with the plastic scintillator modules. Following the results of the previous section, the simulated bolometer events are studied together with the information obtained in the veto system.

### 6.2.1 Remaining background rate

The performance of the veto system within the *Geant4* simulations is discussed in chapter 5.3. With the goal to study possible background events for the EDELWEISS-II Dark Matter search, the energy deposit in the bolometers is restricted to an energy range of $1 < E_{\mathrm{dep}}^{\mathrm{Ge}} < 250\ keV$. This energy range corresponds to the region of interest (RoI) for a possible WIMP-nucleus interaction with Germanium nuclei. By this means, the total of $\sim 10^6$ simulated bolometer hits reduces to $\approx 3.6 \times 10^5$, containing still all nuclear recoils ($\approx 1.7 \times 10^5$), since high energy deposits are predominantly caused by electron recoils. No further restriction in terms of separation of nuclear and electron recoils, as outlined in section 6.1.2, are made to the bolometer data.

In the analysis of the simulation data, a bolometer event in the region of interest

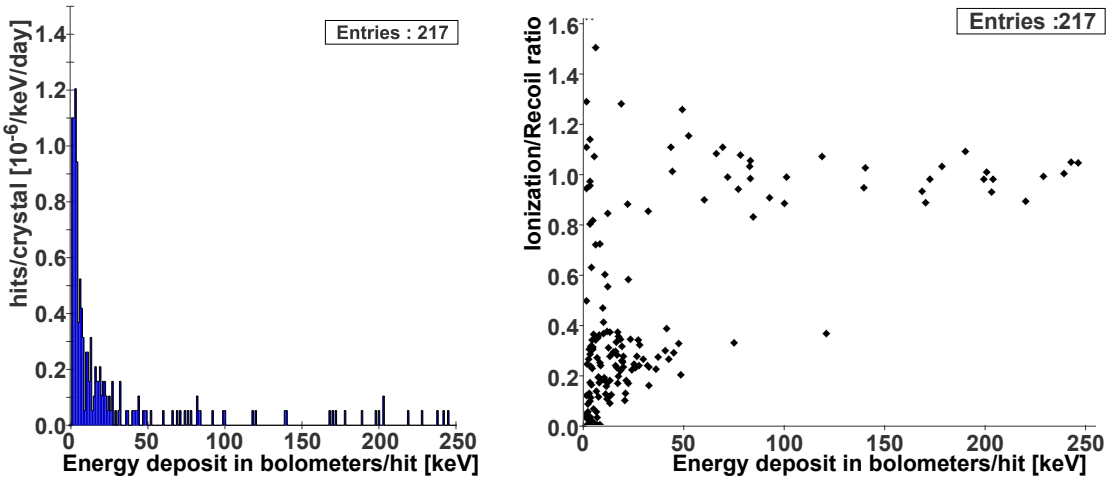


(a) Hits per crystal (b) $Q$-plot

**Figure 6.6:** (a): The simulated energy deposit spectrum in Germanium bolometers after applying the veto condition $E_{\text{dep}}^{\text{veto}} > 2\ MeV$. (b): Corresponding $Q$-plot.

is rejected in case of an energy deposit in any module of the veto system of $E_{\text{dep}}^{\text{veto}} > 2\ MeV$. This admittedly very good energy threshold on the veto system has no direct correspondence in the experimental data since the effective energy threshold of the modules is position-dependent due to the attenuation of the scintillation light. However, this 2 $MeV$-threshold is a realistic simplification of the hardware threshold realised. Implications from varying this threshold are discussed in section 6.2.3 in more detail.

The remaining simulated energy deposit spectrum, after applying the veto condition, is shown in figure 6.6. As can be seen, from the initial $\approx 3.6 \times 10^5$ hits a scarce remainder of 217 hits are left. Furthermore, the remaining hits are recorded in only 87 muon events. The multiplicty $m$, as defined in section 6.1.3, is on average $\langle m \rangle \approx 3.5$. The corresponding effective measuring time of the analysed simulation data, as previously mentioned, is $t \approx 160\ 000\ d$.
Accepting multiple hits in several of the 120 Germanium crystals per muon event ($m \geq 1$), the muon-induced background rate of energy deposits in the bolometers between $1\ < E_{\text{dep}}^{\text{Ge}} < 250\ keV$ is :

$$\mathbf{\Gamma_{bg}(E_{dep}^{veto} > 2\ MeV; m \geq 1)\ \leq\ 1.4 \pm 0.2 \times 10^{-5}\ kg^{-1} \cdot d^{-1}} \tag{6.7}$$

Applying the more stringent condition that only one crystal records an energy deposit ($m = 1$), the rate is:

$$\Gamma_{\text{bg}}(E_{\text{dep}}^{\text{veto}} > 2\ MeV; m = 1)\ \leq\ 0.4 \pm 0.1 \times 10^{-5}\ kg^{-1} \cdot d^{-1} \tag{6.8}$$

Though about 33 million of muons are simulated in the *Geant4* simulations, applying constraints on the initial data, e.g. energy deposit in the region of interest and

the bolometer multiplicity, and finally using information about coincident energy deposit in the veto system, a total of only 24 events remain. The possibility to separate electron and nuclear recoils is almost inessential for the simulation data of muon-induced background, since only about $\sim 15\%$ of the remaining hits are associated with electron recoils in the bolometers, see also figure 6.6(b).
The efficiency of the veto system can be expressed by the reduction $R$ of the event rate as:

$$\epsilon = \frac{1}{R} = \frac{N^{\text{veto}}}{N^{\text{total}}} \tag{6.9}$$

where the denominator represents the total number of events of the sample and the nominator the events left after applying the veto condition. Using the various event samples, the efficiency of the muon veto system is:

$$1 - \epsilon \ \geq (99.94 \pm 0.01)\% \tag{6.10}$$

where the statistical error is dependent on the chosen event sample. See table 6.3 for details. A similar analysis can be performed for the simulation data of the low muon energy range. An overview of the event rates, as determined for the given muon energy ranges only, is given in table 6.3. The bolometer event rate is reduced by a factor $\sim 2$ for the lower muon energy range in comparison to the intermediate energy range. This is a result of the reduced neutron production for lower muon energies, as discussed in section 6.1.1. After applying the veto condition, however, the remaining background rate is of the same order for both muon energy ranges. Hence, the veto efficiency $(1 - \epsilon)$ decreases. Apart from larger statistical errors, the efficiency determined for the lower muon energy range is approximately $(1 - \epsilon)_{m \geq 1} = (99.85 \pm 0.04)\%$.
The veto efficiency depends also on the veto energy threshold, e.g. $E_{\text{dep}}^{\text{veto}} > 2\ MeV$, as discussed in the following chapter. For instance, the detection of only secondaries of the muon-induced shower with the veto system, can in principle increase the effective muon detection area. However, the electromagnetic shower induced by muons is less prominent for lower muon energies. As a result, the detection efficiency for muons at a given distance to the muon veto system decreases with decreasing muon energies.
To conclude, the extrapolation of the background rates from a fractional muon energy range to the total muon flux, e.g. (6.7) and (6.8), is possible within the discussed uncertainties. In doing so, the possible reduction of muon-induced background events in the EDELWEISS-II Germanium bolometers with the muon veto system can be approximated to $R \approx 10^3$. The remaining background rate is $\Gamma_{\text{bg}} \lesssim 10^{-5}\ kg^{-1} \cdot d^{-1}$.

### 6.2.2 Remaining background events

The background rate in the Germanium bolometers can be reduced to approximately $\Gamma_{\text{bg}} \approx 10^{-5}\ kg^{-1} \cdot d^{-1}$. For the remaining events the energy deposit in the veto system is below threshold, e.g. $E_{\text{dep}}^{\text{veto}} < 2\ MeV$. Here, one can differentiate between two

| condition | muon energy range $200 < E_\mu < 2000\ GeV$ | | veto efficiency $1-\epsilon$ | reduction $R$ |
|---|---|---|---|---|
| | *no veto* | *veto* | | |
| hits (RoI) | $2.1 \pm 0.01 \times 10^{-2}$ | $1.3 \pm 0.1 \times 10^{-5}$ | $(99.94 \pm 0.004)\%$ | $1691 \pm 126$ |
| $m \geq 1$ (RoI) | $8.5 \pm 0.04 \times 10^{-3}$ | $5.0 \pm 0.6 \times 10^{-6}$ | $(\mathbf{99.94 \pm 0.007})\%$ | $1692 \pm 194$ |
| $m = 1$ (RoI) | $2.4 \pm 0.02 \times 10^{-3}$ | $1.4 \pm 0.3 \times 10^{-6}$ | $(99.94 \pm 0.01)\%$ | $1757 \pm 376$ |
| | muon energy range $20 < E_\mu < 200\ GeV$ | | | |
| hits (RoI) | $6.2 \pm 0.09 \times 10^{-3}$ | $1.3 \pm 0.3 \times 10^{-5}$ | $(99.80 \pm 0.04)\%$ | $492 \pm 107$ |
| $m \geq 1$ (RoI) | $5.2 \pm 0.08 \times 10^{-3}$ | $7.7 \pm 2.0 \times 10^{-6}$ | $(99.85 \pm 0.04)\%$ | $670 \pm 183$ |
| $m = 1$ (RoI) | $1.5 \pm 0.04 \times 10^{-3}$ | $2.4 \pm 1.1 \times 10^{-6}$ | $(99.84 \pm 0.07)\%$ | $640 \pm 306$ |

**Table 6.3:** Overview of the simulated bolometer events and the muon veto efficiency. The rates correspond to the fraction of the muon flux $\Phi_\mu/\Phi_{\text{tot}}$ as given in table 6.1. The energy deposit in the bolometers is in the range of $1 < E^{\text{Ge}}_{\text{dep}} < 250\ keV$ (RoI). All rates are given in $\left[kg^{-1} \cdot d^{-1}\right]$. The veto condition is an energy deposit in any module of $E^{\text{veto}}_{\text{dep}} > 2\ MeV$ coincident with the bolometer events.

event classes: First, the muon passed the veto system undetected. This means that the muon enters the experimental setup through the apparent gaps in the veto system. Due to the large gaps in the veto system at the northern side of the lower level, i.e. N0-Nord, and the ground floor, i.e. N0-Sol, muons can pass undetected nearby the bolometers, see also the discussion in section 5.1.2. A subsequent nuclear recoil in the bolometer can therefore not be associated with the incident muon and remains as background. Another possibility is given for muons striving the edges of the scintillator modules and the corresponding energy deposit in the module does not exceed the veto energy threshold.
The second event category includes events, where the muon passed only nearby the experimental setup without entering the volume inside the veto system. Secondaries created by the muon for example in the rock surrounding the experiment pass through the veto system undetected and eventually interact in the Germanium crystals. These events are therefore called 'outside-muon' events.

As already suggested in chapter 5.3.2, the muon veto system of EDELWEISS-II with its low energy threshold can be used to identify also outside-muon events. In the analysis of the simulation data, the detector volume, as defined in chapter 5.1.2, is used to classify the event in either muon events missed by the veto system or outside-muon events. In total, 562 events are recorded with energy deposit in the Germanium crystals and in which the muon did not enter the veto volume, i.e. outside-muon events. The corresponding background rate is:

$$\Gamma^{\text{out}}_{\text{bg}}(m \geq 1) \leq 9.2 \pm 0.4 \times 10^{-5}\ kg^{-1} \cdot d^{-1} \tag{6.11}$$

As discussed previously, the background rate after applying the veto condition is

almost an order of magnitude lower than $\Gamma_{\mathrm{bg}}^{\mathrm{out}}$. This can be explained by the electromagnetic shower associated with the muon and its detection in one of the module of the veto system. Referring to figure 5.7, an energy threshold in the veto system of $E_{\mathrm{dep}}^{\mathrm{veto}} \lesssim 10\ MeV$ allows the detection of secondary particles of the muon-induced shower. In this connexion, the muon not necessarily has to be detected in a neighbouring module. As a result, the effective detection area for cosmic ray muons with the EDELWEISS-II muon veto system increases with decreasing veto energy threshold applied. The consequences on the remaining background rate are discussed in the following section.

### 6.2.3 Veto energy threshold dependence

The applied veto energy threshold of $E_{\mathrm{dep}}^{\mathrm{veto}} > 2\ MeV$ in the previous sections represents the aimed energy threshold of the veto system [Rei98]. However, the energy deposit per module is not directly measured.
The scintillation amplitudes obtained by the photomultipliers on each side of the module depend on the light absorption coefficient of the scintillator material. This means that with increasing distance of the photon origin to the photomultipliers, the measured amplitude decreases. As a result, the summed amplitudes of coincident measurements of the two sides, and hence the position of the Landau maxima for vertical cosmic ray muons in ADC-channels, varies along the module axis. A measurement of the effective light yield for vertical cosmic ray muons along the module axis has been performed in Karlsruhe exemplary for two modules before installation at the LSM underground laboratory [Hab04]. The outcomes of the measurements attest a very good separation of muon from background events. Furthermore, the applied high voltages for the photomultipliers on each side of the modules and the discriminator threshold were chosen according to calibration measurements with vertical muons. At this, not only the effective light yield was taken into account, but also the possibility of streaking muons at the edges of the modules were considered. Here, muons pass only through a fraction of the thickness of the module. To ensure the detection of all muon events the effective discriminator threshold were chosen as low as possible, with respect to the expected event rate at the LSM underground laboratory. Since after each veto hit a certain deadtime, e.g. $t \approx 100\ \mu s$, is applied in the analysis of the bolometer data the effective measuring time for Dark Matter searches decreases. As a summary, the threshold set on the muon veto system corresponds at best to an energy deposit of $E_{\mathrm{dep}} > 2\ MeV$. In fact, more likely is a slightly higher averaged threshold along the length of the individual veto modules. Therefore, the results of the veto efficiency of muon-induced bolometer events, as discussed in the previous section, are studied depending on the applied veto energy threshold.

As can be seen in figure 6.7, the background rate $\Gamma_{\mathrm{bg}}(m \geq 1)$ increases as expected with increasing energy threshold for the veto condition. For example, setting the veto energy threshold to approximately $E_{\mathrm{dep}} \approx 9\ MeV$, the veto system is only sensitive to full muon hits since the low energy deposit of secondaries is cut off. As a result,

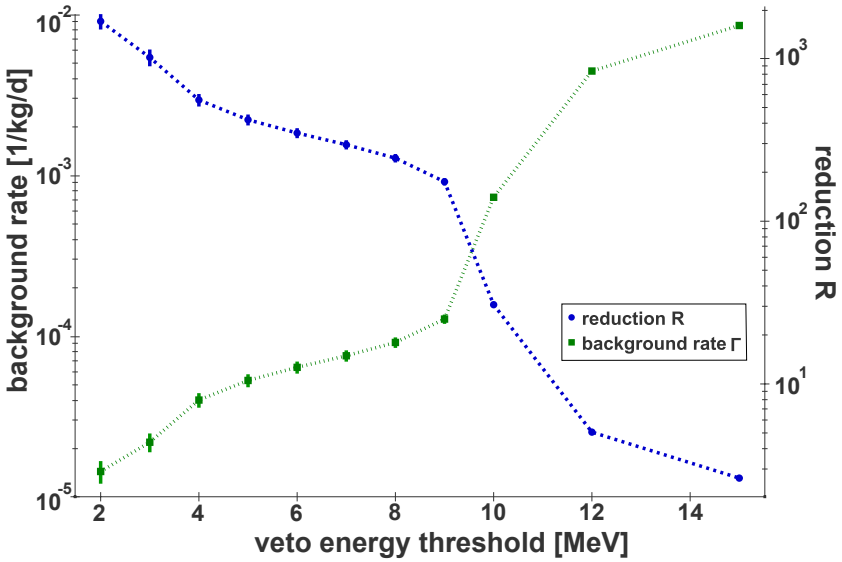


**Figure 6.7:** Remaining background rate in $\left[kg^{-1} \cdot d^{-1}\right]$ (green) as a function of the veto energy threshold. Also shown is the reduction factor $R$ (blue).

the remaining background rate corresponds to the previously discussed bolometer rate induced by outside-muon events, i.e. $\Gamma_{\mathrm{bg}} = \Gamma_{\mathrm{bg}}^{\mathrm{out}} \approx 10^{-4}\ kg^{-1} \cdot d^{-1}$. By a further increase of the veto energy threshold, e.g. $E_{\mathrm{dep}} \gtrsim 10\ MeV$, muons passing through the veto volume would not be detected and the remaining background approaches the initial background rate, i.e. $\Gamma_{\mathrm{bg}} \cong \Gamma_{\mathrm{bg}}^{\text{no veto}} \approx 10^{-2}\ kg^{-1} \cdot d^{-1}$.
The corresponding values for the reduction factor $R$ are also plotted in figure 6.7.

## 6.3 Conclusions

High energetic neutrons produced by cosmic ray muons are potentially limiting the sensitivity of direct Dark Matter searches, due to the indistinguishability of nuclear recoils caused by neutrons or WIMPs. On this account, the experimental setup of EDELWEISS-II includes an active muon veto detector placed around the passive shielding materials. In the simulations of this work, the specific muon flux in the underground laboratory LSM, together with a detailed geometry of the experimental hall and the complete experimental setup is used to study the performance of the muon veto system. The geometrical muon detection efficiency of the system is determined to $\epsilon = 98.2\%$. Furthermore, in taking into account nuclear recoils in the Germanium bolometers of the EDELWEISS-II experiment, the veto efficiency in an end-to-end simulation is studied for the first time. In this connexion, the simulation toolkit *Geant4* `8.1.p01` with a dedicated user defined physics list provides sufficient accuracy in comparison with the scarce experimental data. As a result of the simulations, the muon-induced background rate in the bolometers is reduced at best to a remaining rate in the order of $\Gamma_{\mathrm{bg}} \sim 10^{-5}\ kg^{-1} \cdot d^{-1}$ demonstrating the potential

of the veto system. However, the deduced background rate is strongly dependent on the energy threshold applied to the veto system. Relaxing the requirements of the veto condition, e.g. increasing the minimal energy deposit in the veto system, the remaining background rate of $\Gamma_{\mathrm{bg}} \sim 10^{-4}\ kg^{-1} \cdot d^{-1}$ in the simulations is still one order of magnitude lower than necessitated to reach sensitivities $\sim 10^{-8}\ pb$ on the WIMP-nucleus scattering cross section. The latter background rate is associated with muons passing through the rock nearby the experimental setup and would naturally be considered as the irrevocable limit of the system. However, the potential further reduction is explained by the possibility to detect the electromagnetic shower of the close-by muons and consequently increasing the effective detection area of the veto system. The total veto efficiency of muon-induced background for the EDELWEISS-II experiment, as simulated with *Geant4*, is:

$$1 - \epsilon \ \geq \ (99.94 \pm 0.01)\% \tag{6.12}$$

Taking into account the approximations on the muon flux, the veto energy threshold and the simulation code uncertainties, one can approximate the systematic error on the result (6.12). At this, the introduced systematic error to the total muon flux at the underground laboratory and the uncertainties of the muon generator is estimated to around $\sim 30\%$. As discussed in chapter 3, the model uncertainties on the neutron production in comparison with experimental data is less than a factor $\sim 2$. Equivalent approximations can be done on the neutron interaction rate in Germanium and the recorded energy deposit. As a side remark, simulations using the *Geant4* toolkit on elastic and inelastic scattering of neutrons particular off Germanium nuclei indicate some problems on the energy and momentum conservation in the programming code. For instance, the program class of *Geant4* for inelastic scattering processes is found to miscalculate the kinematics of the process [Sch07]. However, the results obtained in the simulations of this work are neither strongly dependent on the angular dependence of the recoiling Germanium nuclei nor the scattered neutron. Moreover, since the error occurs only in inelastic scattering processes, an estimated uncertainty on the recorded energy deposit of around $\times 2$ is reasonable.
In total, the veto efficiency including systematic errors can be approximated to:

$$1 - \epsilon \ \gtrsim (99.94 \pm 0.01\ ^{+0.06}_{-0.1})\% \tag{6.13}$$

This translates to a potential reduction of energy deposit events in the Germanium with the EDELWEISS-II muon veto system in the order of $R \approx \mathcal{O}(10^3)$.

# 7 Conclusions and Outlook

The second phase of the EDELWEISS experiment is currently operating in the underground laboratory LSM searching for Dark Matter particles recoiling on Germanium nuclei. The use of heat and ionisation detectors enables to discriminate between electron and nuclear recoils. Consequentially neutrons are the main background which will in turn limit the sensitivity of the experiment. Neutrons, besides from natural radioactivity through ($\alpha$,n) reactions, are produced by cosmic ray muons in the surrounding rock and in the experimental setup. Therefore a neutron moderator of 50 $cm$ of polyethylene is installed for EDELWEISS-II. Moreover, to correlate recoil events in the Germanium bolometers with a cosmic ray muon, an active muon detector system with a surface of $\sim 100\ m^2$ consisting of 42 individual plastic scintillator modules is placed hermetically around the polyethylene shielding.

It has been shown in the present work that the simulation toolkit *Geant4*, as used for background studies of underground experiments such as EDELWEISS, provides compatible results with the scarce experimental data and theoretical predictions, as well as with other simulation codes such as `FLUKA`. On this purpose, the muon-induced production of neutrons has been studied for different muon energies and for materials relevant for the EDELWEISS experiment. The obtained results are in reasonable good agreement with measurements taking into account the large spread in the experimental data. However, comparison to the differential cross section of neutron production in thin targets may indicate that the neutron production in *Geant4* as well as in `FLUKA` is significantly underestimated [Pan07]. The theoretical models implemented in the simulation codes require further investigation and validation with experimental data. Within the EDELWEISS collaboration, a dedicated neutron detector will be installed in the underground laboratory next to the veto system. The goal is, besides measuring the ambient neutron flux, to associate neutrons with coincident muon detection in the EDELWEISS-II muon veto system. In close relation to this work, design studies are currently performed using *Geant4* and a first prototype of the neutron detector has been built at Forschungszentrum Karlsruhe [Kluon].

In this work, the muon flux and energy spectrum in the underground laboratory LSM has been determined analytically using a detailed profile of the Fréjus mountain. A first preliminary comparison of the simulation results with measurements of muon rates with the veto system as installed at the LSM has been performed. A general agreement for the specific geometries of the individual sides of the veto system and the corresponding exposure according to the rock overburden could be found. A more detailed study of the veto data is in preparation with the goal

to reconstruct muon tracks and hence determine the angular spectrum of muons underground [Chaon].

Investigating the potential coincidences of muon-induced background events in the Germanium crystals and an energy deposit in the veto system in an end-to-end simulation, a remaining background of:

$$\Gamma_{\mathrm{bg}} \;\leq\; 1.4 \pm 0.2 \times 10^{-5}\; kg^{-1} \cdot d^{-1} \tag{7.1}$$

has been found. Though this result is dependent on the applied model and the experimental performance of the veto system, a reduction of the nuclear recoil events in the bolometers in the order of $r \approx \mathcal{O}(10^3)$ seems feasible.

It was shown that most neutrons leading to energy deposit in the Germanium crystals are produced in the surrounding lead by secondary particle production. Neutrons produced with high kinetic energies in the nearby rock are predominantly moderated or absorbed in the shielding material or can be correlated to the incident muon by use of the veto system. However, secondary particles migrating far from the muon track, entering the veto volume undetected and again producing neutrons, though with lower energies, classify the remaining recoil events. As a result the energy transfer in nuclear recoils to the Germanium nuclei is very small. Hence the remaining background rate is strongly dependent on the applied energy threshold of the Germanium bolometers.

The study of the muon-induced background, as done in this work, provides essential information for the shielding concept of future experiments. As a result of an end-to-end simulation the muon-induced background could be further reduced by a factor of $\sim 100$ in comparison with earlier simulations based on a corrected version of the *Geant3* physics implementation of muon nuclear interactions. Besides the specific muon flux in the underground laboratory as a result of the mountain overburden, the full $3D$ implementation of the experimental setup is essential. By investigating the full topology of the rare background events, more precise predictions can be made on the efficiency of an implemented veto system and on the remaining background rate. As shown in this thesis, taking into account full topology of muon-induced events from muon spallation processes down to the simulated energy deposit in the bolometers, rather than assuming an average interaction rate of an approximated neutron flux in the detector volume, provides the detailed knowledge to achieve a background reduction which is by two orders of magnitude better than previous simulations. This result is of great importance in developing the design of larger scale Dark Matter experiments such as EURECA, aiming for a sensitivity on the WIMP-nucleon cross section of $10^{-10}$pb [Kra06]. The EURECA experiment is based on a modular design of cryogenic bolometers summing up to a total of about one tonne of detector material. There are plans to extend the existing underground laboratory LSM substantially, allowing a dedicated space for a one-tonne-scale Dark Matter search [Bau07]. This would be a unique opportunity to develop an integrated

shielding concept including the underground cavity itself into the design. First studies are performed [Bauon] based on the results of this work, e.g. the use of a second polyethylene shielding inside the inner lead shielding of a cryostat to moderate secondary neutrons. Having demonstrated the significant effect of actively vetoing not only muons but also muon-induced secondary particles provides essential input for the active shielding of future Dark Matter experiments.

# A Muon flux underground

High energy cosmic ray muons are produced in the atmosphere in the decay of energetic mesons. Contrary to the main secondary particles of cosmic ray showers, e.g. hadrons, electrons and $\gamma$-rays, which interact immediately with the rock and are quickly absorbed, only high energetic muons can penetrate deep underground. As described in equation (4.2), the muon flux declines with energy by one power more than the primary cosmic ray flux. For typical underground laboratories the muon flux is suppressed to sea level approximately by a factor of $10^4 - 10^6$. However, the mean muon energy increases with depth. To study the muon flux underground, the interactions of muons with matter are first reviewed.

Muons lose energy not only by ionisation, but also by radiative processes such as bremsstrahlung, direct pair-production and photo nuclear muon interaction or muon deep inelastic scattering. The energy loss of moderately relativistic muons by **ionisation** is determined by the Bethe-Bloch formula [Bet30]:

$$\left[\frac{dE}{dx}\right]_{\text{ion}} = 4\pi N_{\text{AV}} r_e^2 m_e c^2 \frac{Z}{A}\frac{(z)^2}{\beta^2}\left[\frac{1}{2}ln\left(\frac{2m_e c^2\beta^2\gamma^2 T_{max}}{I^2}\right) - \beta^2 - \frac{\delta(\beta\gamma)}{2}\right] \quad \text{(A.1)}$$

with Avogadro's number $N_{\text{AV}}$, the classical electron radius $r_e$, the electron rest mass $m_e$, the atomic number $Z$ and mass $A$ of the absorber material and the charge of the incident particle $z = z_\mu = 1$. The mean excitation energy in the material is $I$. The energy of the muon divided by its mass is in this representation $\gamma = E_\mu/m_\mu c^2$ and $\beta = 1 - (1/\gamma^2)$. $\delta(\beta\gamma)$ is the density effect correction to the ionisation energy loss. The value of the maximum energy transferable to a free electron in a single collision is $T_{max}$ and can be written as:

$$T_{max} = \frac{2m_e c^2\beta^2\gamma^2}{1 + 2\gamma m_e/m_\mu + (m_e/m_\mu)^2} \quad \text{(A.2)}$$

Ionisation energy loss depends only weakly on the muon energy and can be described approximately for standard rock with an accuracy of around 5% for muon energies above 10 $GeV$ by [Gai90]:

$$\left[\frac{dE_\mu}{dX}\right]_{\text{ion}} \approx 1.9 + 0.08\ ln(\frac{E_\mu}{GeV})\ \frac{MeV}{g/cm^2} \quad \text{(A.3)}$$

and in first approximation for minimal ionising particles:

$$\left[\frac{dE_\mu}{dX}\right]_{\text{ion}} \approx 2\ \frac{MeV}{g/cm^2} \quad \text{(A.4)}$$

with $X = \rho \cdot x$ is expressed in terms of column density in units $[g/cm^2]$. The cross section for radiation processes, e.g. bremsstrahlung, $e^+e^-$-pair production and muon nuclear interactions are much smaller than for ionisation. However, on average the energy loss rate for theses processes is proportional to the muon energy $E_\mu$ and becomes important for very high muon energies. The basic energy loss formulae will be given here as in [GEA07a], [Sta04] and [Loh85].

Muons slowed down or deflected in the coulomb field of atomic electrons or the atomic nuclei emit **bremsstrahlung** photons. The cross section for muon bremsstrahlung is:

$$\left(\frac{d\sigma}{d\nu}\right)_{\text{brems}} = \alpha \left(2r_e \frac{m_e}{m_\mu}\right)^2 Z(Z+1)\frac{1}{\nu}\left[\frac{4}{3}(1-\nu)+\nu^2\right]\xi(\delta) \tag{A.5}$$

where $\nu$ is the fraction of energy transferred to the photon. To take into account the effect of atomic electrons $Z^2$ is replaced by $Z(Z+1)$. The screening function $\xi(\delta)$ depends on the minimum momentum transfer to the nucleus: $\delta = m_\mu^2\nu/(2E_\mu(1-\nu))$. This function can be parametrised according to experimental data for different nuclei and can be found in [GEA07a]. The muon energy loss by bremsstrahlung can be calculated analytically by integration:

$$\left[\frac{dE_\mu}{dx}\right]_{\text{brems}} = E_\mu \frac{N_{\text{AV}}}{A}\int_{\nu_{\min}}^{\nu_{\max}} \nu \left(\frac{d\sigma}{d\nu}\right)_{\text{brems}} d\nu \cong E_\mu b_b(E_\mu) \tag{A.6}$$

with $\nu_{min} = 0$ and $\nu_{max} = 1 - \frac{3}{4}\sqrt{e}(m_\mu/E_\mu)Z^{1/3}$. The energy loss is in first order approximation proportional to the muon energy.

**Muon pair production** takes place if a virtual muon-induced photon is absorbed in the coulomb field of an atomic nucleus.

$$\mu \ + \ Z \rightarrow \mu \ + \ e^+e^-Z' \tag{A.7}$$

The cross section for $e^+e^-$-pair production as derived from QED calculations in a general parametrised form is:

$$\left(\frac{d^2\sigma}{d\nu d\rho}\right)_{\text{pair}} = \frac{2}{3\pi}(r_e\alpha)^2 Z(Z+1)\frac{1-\nu}{\nu}\left[\Phi_e(E_\mu,\rho,\nu) + \left(\frac{m_e}{m_\mu}\right)^2 \Phi_\mu(E_\mu,\rho,\nu)\right] \tag{A.8}$$

where $\rho = (E^+ - E^-)/(E^+ + E^-)$ is the asymmetry parameter of the electron-positron pair. The functions $\Phi_e$ and $\Phi_\mu$ correspond to different QED diagrams and also contain atomic and nuclear form factors. The explicit form is given in [Loh85]. To obtain the muon energy loss due to pair production the twofold integral:

$$\left[\frac{dE_\mu}{dx}\right]_{\text{pair}} = 2E_\mu \frac{N_{\text{AV}}}{A}\int_{\nu_{\min}}^{\nu_{\max}} \nu \int_0^{\rho_{\max}} \left(\frac{d^2\sigma}{d\nu d\rho}\right)_{\text{pair}} d\rho d\nu \cong E_\mu b_p(E_\mu) \tag{A.9}$$

has to be solved numerically, where the energy transfer lies between $\nu_{\min} = \frac{4m_\mu}{E_\mu}$ and $\nu_{\max} = 1 - \frac{3}{4}\sqrt{e}\frac{m_\mu}{E_\mu}Z^{1/3}$. The pair production is one of the most important muon interaction processes and is the dominant process for high energy muons in the $TeV$ range. The contribution to the energy loss rate increases approximately with the muon energy and accounts for almost the half of the energy loss for $TeV$ muons.

The **muon photo nuclear reaction** or muon deep inelastic scattering ($\mu$-DIS) is described by the absorption of a virtual photon by the nucleus (see also figure 3.2). The cross section of this reaction can be calculated using two structure functions corresponding to two virtual photon polarisation directions:

$$\left(\frac{d^2\sigma}{d\nu dt}\right)_{\text{DIS}} = \frac{\alpha}{\pi}\left[\Sigma_t\sigma_t + \Sigma_l\sigma_l\right], \tag{A.10}$$

with the interaction cross section of transversely and longitudinally polarised virtual photons $\sigma_t$ and $\sigma_l$, the functions $\Sigma_r$ and $\Sigma_l$ representing the virtual photon flux, respectively. The energy loss of the incident muon (or energy transfer) is hereby represented by $\nu$ and the absolute value of the square of the four-momentum transferred from the muon to the nucleus is $t = -q^2$. The integration over $t$ is done following Hand's formalism by connecting the virtual photon cross section with the experimental measured one $\sigma_{\text{exp}} = \sigma_{\gamma N}F(t)$. The inelastic form factor can be written as $F(t) = 1/(1 + t/\Lambda^2)$ where $\Lambda$ is an experimental parameter, determined to $\Lambda^2 = 0.4\ GeV^2$. Thus the differential muon nuclear cross section can be written as:

$$\left(\frac{d\sigma}{d\nu}\right)_{\text{DIS}} = \Psi(\nu)\Phi(E, v), \quad \text{with} \tag{A.11}$$

$$\Psi(\nu) = \frac{\alpha}{\pi}\frac{A_{\text{eff}}N_{\text{AV}}}{A}\sigma_{\gamma N}(\nu)\frac{1}{\nu}, \quad \text{and} \tag{A.12}$$

$$\Phi(E, v) = v - 1 + \left[1 - v + \frac{v^2}{2}\left(1 + \frac{2\mu^2}{\Lambda^2}\right)\right] ln\frac{\frac{E^2(1-v)}{\mu^2}\left(1 + \frac{\mu^2v^2}{\Lambda^2(1-v)}\right)}{1 + \frac{Ev}{\Lambda}\left(1 + \frac{\Lambda}{2M} + \frac{Ev}{\Lambda}\right)}, \tag{A.13}$$

with the muon energy $E_\mu = E$, the relative energy loss $v = \nu/E$, $\mu$ and $M$ are the muon and nucleon masses and $A_{\text{eff}}$ includes the nuclear shadowing effect and is parametrised by $A_{\text{eff}} = 0.22A + 0.78A^{0.89}$. To obtain the energy loss rate one again integrates in $\nu$. The upper limit for the integral is taken to $\nu_{\max} = 1 - m_\mu/E_\mu$, while a reasonable choice in *Geant4* for the lower limit is $\nu_{\min} = 0.2\ GeV$. The average energy loss for $\mu$-DIS increases also almost linearly with the muon energy for $TeV$ muon energies and can be written approximately as:

$$\left[\frac{dE_\mu}{dx}\right]_{\text{DIS}} \cong E_\mu b_{\text{DIS}}(E_\mu). \tag{A.14}$$

The total muon energy loss can then be written as:

$$\frac{dE_\mu}{dx} = a \ + \ bE_\mu, \tag{A.15}$$

where $b = b_{\text{brems}} + b_{\text{pair}} + b_{\text{DIS}}$ is the sum of the fractional energy loss of the three radiation processes.

# B Geant4 materials

To describe the physical properties of materials in the *Geant4* simulation toolkit, an abstract class implements the necessary facilities. A material can be a single element or a mixture of elements, while elements are made either of single isotopes or a mixture of isotopes. The physical properties, such as radiation and interaction length, excitation energy loss, coefficients necessary for Bethe-Bloch formula, etc. are derived from the element composition.

The elements used in the simulations of this work are listed in table B.1 as implemented in the *Geant4* material class. In this connexion, only Germanium is constructed by its natural abundances of isotopes, see table B.2. The rock composition used for the EDELWEISS-II simulations in the LSM underground laboratory is given in table B.3. The alternative rock compositions, as tested in chapter 3, are available in table B.4 and B.5. The walls of the underground laboratory are simulated by a concrete according to table B.6.

| element | symbol | atomic number | atomic mass $[g/mole]$ |
|---|---|---|---|
| Hydrogen | H | 1 | 1.00794 |
| Helium | He | 2 | 4.0026 |
| Carbon | C | 6 | 12.011 |
| Nitrogen | N | 7 | 14.00674 |
| Oxygen | O | 8 | 15.9994 |
| Natrium | Na | 11 | 22.98977 |
| Magnesium | Mg | 12 | 24.305 |
| Aluminium | Al | 13 | 26.981539 |
| Silicon | Si | 14 | 28.0855 |
| Phosphor | P | 15 | 30.973761 |
| Sulfur | S | 16 | 32.066 |
| Chlorine | Cl | 17 | 35.453 |
| Potassium | K | 19 | 39.0983 |
| Calcium | Ca | 20 | 40.078 |
| Titanium | Ti | 22 | 47.867 |
| Manganese | Mn | 25 | 54.93805 |
| Iron | Fe | 26 | 55.854 |
| Copper | Cu | 29 | 63.546 |
| Lead | Pb | 82 | 207.2 |

**Table B.1:** Atomic masses used in *Geant4* simulations [Yao06].

| isotope | atomic mass $[g/mole]$ | rel. abundance [%] |
|---|---|---|
| $^{70}Ge$ | 69.9240 | 20.52 |
| $^{72}Ge$ | 71.9216 | 27.43 |
| $^{73}Ge$ | 72.9233 | 7.76 |
| $^{74}Ge$ | 73.9210 | 36.54 |
| $^{76}Ge$ | 75.9213 | 7.76 |

**Table B.2:** The composition of natural Germanium as used in the *Geant4* simulations. The density of Germanium is set to $\rho = 5.31\ g/cm^3$.

| element | C | O | Mg | Al | Si |
|---|---|---|---|---|---|
| [%] | 6.56 | 48.6849 | 0.8856 | 4.7732 | 14.1776 |
| element | S | K | Ca | Mn | Fe |
| [%] | 0.4025 | 1.2504 | 20.4815 | 0.0953 | 2.6890 |

**Table B.3:** Rock compostion in the LSM underground laboratory as used in *Geant4* simulations. Values of relative abundance of elements are taken from [Rho93]. The density is $\rho = 2.74\ g/cm^3$.

| element | C | O | Mg | Al | Si |
|---|---|---|---|---|---|
| [%] | 11.1175 | 61.94 | 0.7417 | 3.6010 | 10.2755 |
| element | S | K | Ca | Mn | Fe |
| [%] | 0.2555 | 0.651 | 10.4025 | 0.0353 | 0.98 |

**Table B.4:** Alternative interpretation of rock compositon, taken from [Rho93]. The density is $\rho = 2.74\ g/cm^3$.

| element | H | C | O | Na | Mg | Al | Si |
|---|---|---|---|---|---|---|---|
| [%] | 0.125 | 2.0662 | 31.3634 | 0.4047 | 0.8168 | 2.8065 | 7.8651 |
| element | P | K | Ca | Ti | Mn | Fe | |
| [%] | 0.0743 | 0.3285 | 49.7041 | 0.134 | 0.0659 | 4.2455 | |

**Table B.5:** Rock composition in the LSM underground laboratory taken from [Cha98]. The density is $\rho = 2.65\ g/cm^3$.

| element | H | C | O | Al | Si | K | Ca |
|---|---|---|---|---|---|---|---|
| [%] | 0.1658 | 2.4693 | 34.2121 | 0.5547 | 3.2342 | 0.0321 | 59.3318 |

**Table B.6:** The composition of the concrete walls of LSM underground laboratory. The density is $\rho = 2.4\ g/cm^3$.

# Bibliography


[Aal05] C. E. Aalseth et al. (Majorana Collaboration), *The proposed Majorana $Ge^{76}$ double-beta decay experiment*, Nucl. Phys. Proc. Suppl. **138** (2005), 217–220.

[AF05] M. S. Armel-Funkhouser et al. (CDMS Collaboration), *Exclusion Limits on the WIMP-Nucleon Cross-Section from the First Run of the Cryogenic Dark Matter Search in the Soudan Underground Lab*, Phys. Rev. **D72** (2005), 052009, astro-ph/0507190.

[Afo03] C. Afonso et al. (EROS Collaboration), *Limits on Galactic Dark Matter with 5 Years of EROS SMC Data*, Astron. Astrophys. **400** (2003), 951, astro-ph/0212176.

[Agl89] M. Aglietta et al., *Neutron flux generated by cosmic ray muons at 5200 $hg/cm^2$ s.r. underground: Depth - neutron intensity curve*, Nuovo Cim. **C12** (1989), 467–477.

[Agl98] M. Aglietta et al. (LVD Collaboration), *Muon depth - intensity relation measured by LVD underground experiment and cosmic-ray muon spectrum at sea level*, Phys. Rev. **D58** (1998), 092005, hep-ex/9806001.

[Agl99] M. Aglietta et al. (LVD Collaboration), *Measurement of the neutron flux produced by cosmic-ray muons with LVD at Gran Sasso*, $26^{\text{th}}$ International Cosmic Ray Conference, Salt Lake City, 1999.

[Ago03] S. Agostinelli et al. (Geant4 Collaboration), *GEANT4: A simulation toolkit*, Nucl. Instrum. Meth. **A506** (2003), 250–303.

[Ahm02] Q. R. Ahmad et al. (SNO Collaboration), *Direct evidence for neutrino flavor transformation from neutral-current interactions in the Sudbury Neutrino Observatory*, Phys. Rev. Lett. **89** (2002), 011301, nucl-ex/0204008.

[Ahr03] J. Ahrens et al. (The IceCube Collaboration), *IceCube: The next generation neutrino telescope at the South Pole*, Nucl. Phys. Proc. Suppl. **118** (2003), 388–395, astro-ph/0209556.

[Ake06] D. S. Akerib et al., *The SuperCDMS proposal for dark matter detection*, Nucl. Instrum. Meth. **A559** (2006), 411–413.

[Alc00] C. Alcock et al., *The MACHO Project: Microlensing Results from 5.7 Years of Large Magellanic Cloud Observations*, Astrophys. J. **542** (2000), 281–307, astro-ph/0001272.

[All06] J. Allison et al. (Geant4 Collaboration), *Geant4 developments and applications*, IEEE Trans. Nucl. Sci. **53** (2006), 270.

[Aln05a] G. J. Alner et al., *The DRIFT-II dark matter detector: Design and commissioning*, Nucl. Instrum. Meth. **A555** (2005), 173–183.

[Aln05b] G. J. Alner et al., *Nuclear recoil limits from the ZEPLIN I liquid xenon WIMP dark matter detector*, New Astron. Rev. **49** (2005), 245–249.

[Aln07] G. J. Alner et al., *First limits on WIMP nuclear recoil signals in ZEPLIN-II: A two phase Xenon detector for dark matter detection*, ArXiv e-prints (2007), astro-ph/0701858.

[Ama06] J. Amare et al., *Dark matter searches with NaI scintillators in the Canfranc underground laboratory: ANAIS experiment*, J. Phys. Conf. Ser. **39** (2006), 123–125.

[Amb03] M. Ambrosio (MACRO Collaboration), *Measurement of the residual energy of muons in the Gran Sasso underground Laboratories*, Astroparticle Physics **19** (2003), 313.

[Ang04] J. Angrik et al. (KATRIN Collaboration), *KATRIN design report 2004*, FZK Scientific Report (2004), FZKA-7090.

[Ang05] G. Angloher et al., *CRESST-II: Dark matter search with scintillating absorbers*, Nucl. Phys. Proc. Suppl. **138** (2005), 153–155.

[Ang07] J. Angle et al., *First Results from the XENON10 Dark Matter Experiment at the Gran Sasso National Laboratory*, ArXiv e-prints (2007), astro-ph/07060039.

[Apr05] E. Aprile et al., *The XENON Dark Matter Search Experiment*, Nucl. Phys. Proc. Suppl. **138** (2005), 156–159, astro-ph/0407575.

[Ara05] H. M. Araújo, V. A. Kudryavtsev, N. J. C. Spooner, and T. J. Sumner, *Muon-induced neutron production and detection with Geant4 and* `FLUKA`, Nucl. Instrum. Meth. **A545** (2005), 398–411, hep-ex/0411026.

[Arm02] B. Armbruster et al. (KARMEN collaboration Collaboration), *Upper limits for neutrino oscillations muon-antineutrino to electron-antineutrino from muon decay at rest*, Phys. Rev. **D65** (2002), 112001.

[Ata05] M. Atac et al., *ZEPLIN IV: A future large-scale liquid Xenon Dark Matter detector*, New Astron. Rev. **49** (2005), 283–287.

[Aub06] F. Aubin et al., *The PICASSO direct dark matter search experiment*, AIP Conf. Proc. **828** (2006), 265–270.

[Bal03] E. A. Baltz and P. Gondolo, *Improved constraints on supersymmetric dark matter from muon g-2*, Phys. Rev. **D67** (2003), 063503, astro-ph/0207673.

[Bal04] E. A. Baltz and P. Gondolo, *Markov chain Monte Carlo exploration of minimal supergravity with implications for dark matter*, JHEP **10** (2004), 052, hep-ph/0407039.

[Bar04] F. Barao (AMS-02 Collaboration), *AMS: Alpha Magnetic Spectrometer on the International Space Station*, Nucl. Instrum. Meth. **A535** (2004), 134–138.

[Bat97] G. Battistoni, A. Ferrari, C. Forti, and E. Scapparone, *Simulation of muon transport at high energy: Comparison of few different codes*, Nucl. Instrum. Meth. **A394** (1997), 136–145.

[Bat04] M. Battaglia et al., *Updated post-WMAP benchmarks for supersymmetry*, Eur. Phys. J. **C33** (2004), 273–296, hep-ph/0306219.

[Bau01] L. Baudis et al., *First results from the Heidelberg dark matter search experiment*, Phys. Rev. **D63** (2001), 022001, astro-ph/0008339.

[Bau07] D. Bauer and G. Gerbier, *Dark Matter Detection with Cryogenic Detectors*, The $10^{\text{th}}$ international conference on Topics in Astroparticle and Underground Physics (TAUP2007), 2007.

[Bauon] M. Bauer, Ph.D. thesis, Eberhard-Karls Universität Tübingen, in preparation.

[Bek04] J. D. Bekenstein, *Relativistic gravitation theory for the MOND paradigm*, Phys. Rev. **D70** (2004), 083509, astro-ph/0403694.

[Ben00] A. Benoit et al. (EDELWEISS Collaboration), *Event categories in the EDELWEISS WIMP search experiment*, Phys. Lett. **B479** (2000), 8–14, astro-ph/0002462.

[Ben01] A. Benoit et al. (EDELWEISS Collaboration), *First results of the EDELWEISS WIMP search using a 320-g heat-and-ionization Ge detector*, Phys. Lett. **B513** (2001), 15–22, astro-ph/0106094.

[Ben02] A. Benoit et al. (EDELWEISS Collaboration), *Improved exclusion limits from the EDELWEISS WIMP search*, Phys. Lett. **B545** (2002), 43–49, astro-ph/0206271.

[Ben05] A. Benoit et al. (EDELWEISS Collaboration), *Sensitivity of the EDELWEISS WIMP search to spin-dependent interactions*, Phys. Lett. **B616** (2005), 25–30, astro-ph/0412061.

[Ben07a] P. Benetti et al., *First results from a Dark Matter search with liquid Argon at 87 K in the Gran Sasso Underground Laboratory*, ArXiv e-prints (2007), astro-ph/0701286.

[Ben07b] A. Benoit et al. (EDELWEISS Collaboration), *Measurement of the response of heat-and-ionization germanium detectors to nuclear recoils*, Nucl. Instrum. Meth. **A577** (2007), 558–568, astro-ph/0607502.

[Ber87] C. Berger et al. (Fréjus Collaboration), *The Fréjus nucleon decay detector*, Nucl. Instr. Meth. **A262** (1987), 463.

[Ber89] C. Berger et al. (Fréjus Collaboration), *Experimental study of muon bundles observed in the Fréjus detector*, Phys. Rev. **D40** (1989), no. 7, 2163–2171.

[Ber98] L. Bergström, J. Edsjö, and P. Gondolo, *Indirect detection of dark matter in km-size neutrino telescopes*, Phys. Rev. **D58** (1998), no. 10, 103519, hep-ph/9806293.

[Ber00] R. Bernabei et al. (DAMA Collaboration), *Search for WIMP annual modulation signature: Results from DAMA $NaI-3$ and DAMA $NaI-4$ and the global combined analysis*, Phys. Lett. **B480** (2000), 23–31.

[Ber02] R. Bernabei et al., *The liquid Xenon set-up of the DAMA experiment*, Nucl. Instrum. Meth. **A482** (2002), 728–743.

[Ber06a] L. Bergström and A. Goobar, *Cosmology and Particle Astrophysics*, 2nd ed., no. ISBN: 978-3-540-32924-4, Springer-Verlag, 2006.

[Ber06b] R. Bernabei et al., *From DAMA/NaI to DAMA/LIBRA at LNGS*, Eur. Phys. J. **A27** (2006), 57–62.

[Ber07] R. Bernabei et al., *Future goals for the possible DAMA/1ton*, Società Italiana di Fisica **625** (2007).

[Bet30] H. Bethe, *Zur Theorie des Durchgangs schneller Korpuskularstrahlen durch Materie (in German)*, Annalen der Physik **397** (1930), 325–400.

[Bez73] L. B. Bezrukov, V. I. Beresnev, G. T. Zatsepin, O. G. Ryazhskaya, and L. N. Stepanets, *Investigation of depth intensity curve of nuclear events induced by muons*, Yad. Fiz. **17** (1973), 98–103.

[Bez81] L. B. Bezrukov and E. V. Bugaev, *Nucleon shadowing effects in photon nucleus interaction (in Russian)*, Yad. Fiz. **33** (1981), 1195–1207.

[Bia96] N. Bianchi et al., *Total hadronic photoabsorption cross section on nuclei in the nucleon resonance region*, Phys. Rev. **C54** (1996), 1688–1699.

[Blu84] G. R. Blumenthal, S. M. Faber, J. R. Primack, and M. J. Rees, *Formation of galaxies and large-scale structure with cold dark matter*, Nature **311** (1984), 517–525.

[Bod90] B. Bodmann et al., *The Anticounter for the KARMEN Experiment*, Nucl. Instrum. Meth. **A286** (1990), 214–219.

[Boe00] F. Boehm et al., *Neutron production by cosmic-ray muons at shallow depth*, Phys. Rev. **D62** (2000), 092005, hep-ex/0006014.

[Bog06] A. G. Bogdanov et al., *Geant4 Simulation of Production and Interaction of Muons*, IEEE Trans. Nucl. Sci. **53, 2** (2006), 513– 519.

[Bor75] V. V. Borog and A. A. Petrukhin, *The Cross-Section of the Nuclear Interaction of High Energy Muons*, 14$^{\text{th}}$ International Cosmic Ray Conference, München, International Cosmic Ray Conference, vol. 6, 1975, p. 1949.

[Bör93] G. Börner, *The Early Universe: Facts and Fiction*, 4$^{\text{th}}$ ed., Springer-Verlag, 1993.

[Bou04] M. Boulay, A. Hime, and J. Lidgard, *Design constraints for a liquid Neon detector for Dark Matter and solar neutrino interactions*, Nucl. Phys. Proc. Suppl. **143** (2004), 486.

[Bou06] M. G. Boulay and A. Hime, *Technique for direct detection of Weakly Interacting Massive Particles using scintillation time discrimination in liquid Argon*, Astropart. Phys. **25** (2006), 179–182.

[Bra99] M. Bravin et al. (CRESST Collaboration), *The CRESST dark matter search*, Astropart. Phys. **12** (1999), 107–114, hep-ex/9904005.

[Bri86] J. F. Briesmeister et al., *MCNP: A General Monte Carlo Code For Neutron And Photon Transport: Version 3A*, 1986, LA-7396-M, Rev.2.

[Bro06] A. Broniatowski, B. Censier, A. Juillard, and L. Berge (EDELWEISS Collaboration), *Cryogenic germanium detectors for dark matter search: Surface events rejection by charge measurements*, Nucl. Instrum. Meth. **A559** (2006), 378–380.

[Bru93] R. Brun, F. Bruyant, M. Maire, A. C. McPherson, and P. Zanarini, *GEANT - Detector description and simulation tool*, CERN Program Library Long Write-up **W5013** (1993), CERN-DD/EE/84-1.

[Cas73] G. L. Cassiday, J. W. Keuffel, and J. A. Thompson, *Calculation of the Stopping-Muon Rate Underground*, Phys. Rev. **D7** (1973), no. 7, 2022–2031.

[Ceb02] S. Cebrian et al., *The ROSEBUD experiment at Canfranc: 2001 report*, Nucl. Phys. Proc. Suppl. **110** (2002), 97–99, astro-ph/0112272.

[Cen04] B. Censier, A. Broniatowski, A. Juillard, L. Berge, and L. Dumoulin (EDELWEISS Collaboration), *Surface trapping and detector degradation in Ge bolometers for the EDELWEISS Dark Matter search: experiment and simulation*, Nucl. Instrum. Meth. **A520** (2004), 156–158.

[Cha98] V. Chazal et al., *Neutron background measurements in the underground laboratory of Modane*, Astropart. Phys. **9** (1998), 163–172.

[Cha04] L. Chabert, *Étude du bruit de fond neutron induit par les muons dans l'expérience EDELWEISS-II (in French)*, Ph.D. thesis, L'Université Claude Bernard - Lyon 1, 2004.

[Cha07a] A. Chantelauze, *private communication*, November 2007.

[Cha07b] A. Chantelauze (EDELWEISS Collaboration), *Status of the EDELWEISS-II Dark Matter Search*, to appear in SUSY2007 proceedings (2007), 4 pp., astro-ph/07105849.

[Chaon] A. Chantelauze, *Investigations of muon-induced background for the EDELWEISS-II experiment*, Ph.D. thesis, Universität Karlsruhe (TH), in preparation.

[Coc04] A. Coc et al., *Updated Big-Bang Nucleosynthesis compared to WMAP results*, AIP Conf. Proc. **704** (2004), 341–350.

[Col77] P. D. B. Collins, *An Introduction to Regge Theory and High Energy Physics*, Cambridge University Press, 1977.

[Col07] J. Collar et al. (COUPP Collaboration), *COUPP - a search for dark matter with a continuously sensitive bubble chamber*, FERMILAB-PROPOSAL-0961.

[Cop03] C. J. Copi and L. M. Krauss, *Comparing WIMP interaction rate detectors with annual modulation detectors*, Phys. Rev. **D67** (2003), 103507, astro-ph/0208010.

[Dal57] R. H. Dalitz and D. R. Yennie, *Pion Production in Electron-Proton Collisions*, Phys. Rev. **105** (1957), no. 5, 1598–1615.

[Dav81] M. Davis, M. Lecar, C. Pryor, and E. Witten, *The formation of galaxies from massive neutrinos*, Astrophys. J. **250** (1981), 423–431.

[dB96a] A. de Bellefon et al. (EDELWEISS Collaboration), *Dark matter search in the Fréjus Underground Laboratory: the EDELWEISS experiment*, Nucl. Instrum. Meth. **A370** (1996), 230–232.

[dB96b] A. de Bellefon et al. (EDELWEISS Collaboration), *Dark matter search with a low temperature sapphire bolometer*, Astropart. Phys. **6** (1996), 35–44.

[dB02] W. de Boer, C. Sander, M. Horn, and D. Kazakov, *Positron fraction from dark matter annihilation in the CMSSM*, Nucl. Phys. Proc. Suppl. **113** (2002), 221–228, arXiv:astro-ph/0207557.

[dB05] W. de Boer et al., *EGRET excess of diffuse galactic gamma rays as tracer of dark matter*, Astron. Astrophys. **444** (2005), 51–67, astro-ph/0508617.

[dS01] P. di Stefano et al. (EDELWEISS Collaboration), *Background discrimination capabilities of a heat and ionization germanium cryogenic detector*, Astropart. Phys. **14** (2001), 329–337, astro-ph/0004308.

[dS05] P. di Stefano et al. (EDELWEISS Collaboration), *EDELWEISS dark matter search update*, New Astron. Rev. **49** (2005), 251–254.

[Egu03] K. Eguchi et al. (KamLAND Collaboration), *First results from KamLAND: Evidence for reactor antineutrino disappearance*, Phys. Rev. Lett. **90** (2003), 021802, hep-ex/0212021.

[Eit06] K. Eitel (EDELWEISS Collaboration), *Direct Dark Matter search with heat-and-ionization detectors*, Prog. Part. Nucl. Phys. **57** (2006), 366–374.

[Els05] D. Elsaesser and K. Mannheim, *Supersymmetric dark matter and the extragalactic gamma ray background*, Phys. Rev. Lett. **94** (2005), 171302, astro-ph/0405235.

[Eni87] R. I. Enikeev et al., *Underground hadron generated by cosmic ray muons (in Russian)*, Yad. Fiz. **46** (1987), 1492–1501.

[Fas03] A. Fasso et al., *The physics models of FLUKA: Status and recent development*, ArXiv e-prints (2003), hep-ph/0306267.

[Fer05] A. Ferrari, P. R. Sala, A. Fasso, and J. Ranft, *FLUKA: A multi-particle transport code (Program version 2005)*, 2005, CERN-2005-010.

[Fio07] S. Fiorucci et al. (EDELWEISS Collaboration), *Identification of backgrounds in the EDELWEISS-I dark matter search experiment*, Astropart. Phys. **28** (2007), 143–153, astro-ph/0610821.

[Fix96] D. J. Fixsen et al., *The Cosmic Microwave Background Spectrum from the Full COBE FIRAS Data Set*, Astrophys. J. **473** (1996), 576, astro-ph/9605054.

[Fri22] A. Friedmann, *On the Curvature of Space*, Z. Phys. **10** (1922), 377Ű386, Original title:*Über die Krümmung des Raumes*, English translation in: General Relativity and Gravitation **31** (1999), 1991.

[Fuk98] Y. Fukuda et al. (Super-Kamiokande Collaboration), *Evidence for oscillation of atmospheric neutrinos*, Phys. Rev. Lett. **81** (1998), 1562–1567, hep-ex/9807003.

[Gai90] T. Gaisser, *Cosmic Rays and Particle Physics*, Cambridge University Press, 1990.

[Gai07a] R. Gaitskell, *Noble Travails: Noble Liquid Dark Matter Detectors*, APS meeting Jacksonville, 2007.

[Gai07b] R. Gaitskell and J. Filippini, *An interactive plotter for experimental and theoretical data*, available online, October 2007, `http://dmtools.berkeley.edu/limitplots/`.

[Gam46] G. Gamow, *Expanding Universe and the Origin of Elements*, Phys. Rev. **70** (1946), 572–573.

[Gam48] G. Gamow, R. A. Alpher, and H. Bethe, *The Origin of Chemical Elements*, Phys. Rev. **73** (1948), 803–804.

[Gat04] E. Gates et al., *Discovery of New Ultracool White Dwarfs in the Sloan Digital Sky Survey*, Astrophys. J. Lett. **612** (2004), L129–L132, astro-ph/0405566.

[GEA07a] GEANT4 (Geant4 Collaboration), *Geant4: Physics Reference Manual*, 2007, Geant4 collaboration: online publication.

[GEA07b] GEANT4 (Geant4 Collaboration), *Geant4: User-Guide for Application Developers*, 2007, Geant4 collaboration: online publication.

[Geh99] N. Gehrels and P. Michelson, *GLAST: the next-generation high energy gamma-ray astronomy mission*, Astropart. Phys. **11** (1999), 277–282.

[Ger05] G. Gerbier et al. (EDELWEISS Collaboration), *Looking for SUSY with EDELWEISS-I and II*, Nucl. Phys. Proc. Suppl. **138** (2005), 59–64.

[Ger07] G. Gerbier, *Search for Dark Matter with EDELWEISS: status and future*, The $10^{\text{th}}$ international conference on Topics in Astroparticle and Underground Physics (TAUP2007), September 2007.

[Gir05] T. A. Girard et al., *SIMPLE dark matter search results*, Phys. Lett. **B621** (2005), 233–238, hep-ex/0505053.

[Goo85] M. W. Goodman and E. Witten, *Detectability of certain dark-matter candidates*, Phys. Rev. **D31** (1985), 3059.

[Gro73] D. E. Groom et al., unpublished, 1973, Univ. of Utah, Internal Note No. UUCR 102.

[Hab04] F. Habermehl, *Entwicklung der Datenaufnahme und Tests der Vetomodule für das EDELWEISS-II $\mu$-Vetozählersystems (in German)*, Master's thesis, Universität Karlsruhe (TH), 2004.

[Han07] S. Hannestad, A. Mirizzi, G. G. Raffelt, and Y. Y. Y. Wong, *Cosmological constraints on neutrino plus axion hot dark matter*, J. Cosm. Astrop. Phys. **8** (2007), 15, astro-ph/07064198.

[Her95] R. Hertenberger, M. Chen, and B. L. Dougherty, *Muon induced neutron and pion production in an organic liquid scintillator at a shallow depth*, Phys. Rev. **C52** (1995), 3449–3459.

[Hub29] E. Hubble, *A Relation between Distance and Radial Velocity among Extra-Galactic Nebulae*, Proc. Nat. Acad. Sci. **15** (1929), no. 3, 168–173.

[Jui06] A. Juillard et al. (EDELWEISS Collaboration), *Development of Ge/NbSi detectors for EDELWEISS-II with identification of near-surface events*, Nucl. Instrum. Meth. **A559** (2006), 393–395.

[Jun96] G. Jungman, M. Kamionkowski, and K. Griest, *Supersymmetric dark matter*, Phys. Rept. **267** (1996), 195–373, hep-ph/9506380.

[Kai84] A. B. Kaidalov and K. A. Ter-Martirosyan, *Multihadron production at high energies in the model of quark gluon strings*, Sov. J. Nucl. Phys. **40** (1984), 135–140.

[Kam98] M. Kamionkowski and A. Kinkhabwala, *Galactic halo models and particle dark-matter detection*, Phys. Rev. **D57** (1998), 3256–3263, hep-ph/9710337.

[Kat07] T. Katori (MiniBooNE Collaboration), *Charged-Current Interaction Measurements in MiniBooNE*, ArXiv e-prints (2007), hep-ex/07094498.

[Kha95] F. F. Khalchukov et al., *Hadrons and other secondaries generated by cosmic ray muons underground*, Nuovo Cim. **C18** (1995), 517–529.

[Kim06] Y. D. Kim (XMASS Collaboration), *The status of XMASS experiment*, Phys. Atom. Nucl. **69** (2006), 1970–1974.

[KK99] H. V. Klapdor-Kleingrothaus, L. Baudis, G. Heusser, B. Majorovits, and H. Pas (GENIUS Collaboration), *GENIUS: A supersensitive germanium detector system for rare events*, hep-ph/9910205.

[Kluon] H. Kluck, *Enticklung eines Prototyps eines Neutrondetektors für das EDELWEISS-Experiment (in German)*, Master's thesis, Universität Karlsruhe (TH), in preparation.

[Kra86] L. M. Krauss, M. Srednicki, and F. Wilczek, *Solar System Constraints and Signatures for Dark Matter Candidates*, Phys. Rev. **D33** (1986), 2079–2083.

[Kra05a] C. Kraus et al., *Final results from phase II of the Mainz neutrino mass search in tritium beta decay*, Eur. Phys. J. **C40** (2005), 447–468, hep-ex/0412056.

[Kra05b] L. M. Krauss and C. J. Copi, *Different halo models and DAMA / CDMS / EDELWEISS and future detectors*, New Astron. Rev. **49** (2005), 185–192.

[Kra06] H. Kraus et al., *EURECA: The European future of cryogenic dark matter searches*, J. Phys. Conf. Ser. **39** (2006), 139–141.

[Kud03] V. A. Kudryavtsev, N. J. C. Spooner, and J. E. McMillan, *Simulations of muon-induced neutron flux at large depths underground*, Nucl. Instrum. Meth. **A505** (2003), 688–698, hep-ex/0303007.

[Lee06] S. Lee et al., *KIMS: Dark matter search experiment in Korea*, AIP Conf. Proc. **878** (2006), 106–110.

[Lem31] G. Lemaître, *Expansion of the universe, A homogeneous universe of constant mass and increasing radius accounting for the radial velocity of extragalactic nebulae*, Mon. Not. Roy. Astron. Soc. **91** (1931), 483–490.

[Lem06] R. Lemrani and G. Gerbier (EDELWEISS Collaboration), *Update of neutron studies in EDELWEISS*, J. Phys. Conf. Ser. **39** (2006), 145–147.

[L'H87] M. L'Hour, Rev. Archeol. Ouest **4** (1987), 113.

[Lin63] J. Lindhard et al., Math. Fys. Medd. Dan. Vid. Selsk. **33** (1963), 10–14.

[Loh85] W. Lohmann, R. Kopp, and R. Voss, *Energy loss of muons in the energy range 1 GeV to 10000 GeV*, CERN Reports (1985), CERN-85-03.

[Luk88] P. Luke, *Voltage-assisted calorimetric ionization detector*, Appl. Phys. J. **64** (1988), 6858.

[Mar97] S. P. Martin, *A Supersymmetry Primer*, hep-ph/9709356.

[Mar98] S. Marnieros, *Couches minces d'isolant d'Anderson. Application à la bolométrie à très basse température (in French)*, Ph.D. thesis, L'Université Paris XI d'Orsay, 1998.

[Mar04a] S. Marnieros et al. (EDELWEISS Collaboration), *Identification of near surface events using athermal phonon signals in low temperature Ge bolometers for the EDELWEISS experiment*, Nucl. Instrum. Meth. **A520** (2004), 185–188.

[Mar04b] O. Martineau et al. (EDELWEISS Collaboration), *Calibration of the EDELWEISS cryogenic heat-and-ionisation germanium detectors for dark matter search*, Nucl. Instrum. Meth. **A530** (2004), 426–439, astro-ph/0310657.

[Mat94] J. C. Mather et al., *Measurement of the Cosmic Microwave Background spectrum by the COBE FIRAS instrument*, Astrophys. J. **420** (1994), 439–444.

[Mei06] D. Mei and A. Hime, *Muon-induced background study for underground laboratories*, Phys. Rev. **D73** (2006), 053004, astro-ph/0512125.

[Mil83] M. Milgrom, *A Modification of the Newtonian dynamics as a possible alternative to the hidden mass hypothesis*, Astrophys. J. **270** (1983), 365–370.

[Miu07] K. Miuchi et al., *Detector performance of the NEWAGE experiment*, ArXiv e-prints (2007), physics/0701118.

[Mor02] A. Morales et al., *Improved constraints on WIMPs from the international germanium experiment IGEX*, Phys. Lett. **B532** (2002), 8–14, hep-ex/0110061.

[Nav97] J. F. Navarro, C. S. Frenk, and S. D. M. White, *A Universal Density Profile from Hierarchical Clustering*, Astrophys. J. **490** (1997), 493–508, astro-ph/9611107.

[Nav00] X. F. Navick et al. (EDELWEISS Collaboration), *320-g ionization-heat bolometers design for the EDELWEISS experiment*, Nucl. Instrum. Meth. **A444** (2000), 361–363.

[Nav07] X. F. Navick (EDELWEISS Collaboration), *Surface events identification in the EDELWEISS germanium bolometers*, AIP Conf. Proc. **897** (2007), 65–69.

[Neg85] B. Neganov, Otkrytia i izobreteniya **146** (1985), 215.

[Nis07] H. Nishimura, *The NEWAGE experiment*, The 10$^{\text{th}}$ international conference on Topics in Astroparticle and Underground Physics (TAUP2007), 2007.

[Nol06] G. Nollez, *private communication*, 2006.

[Obe05] L. Oberauer, F. von Feilitzsch, and W. Potzel, *A large liquid scintillator detector for low-energy neutrino astronomy*, Nucl. Phys. Proc. Suppl. **138** (2005), 108–111.

[Oka97] N. Okada and O. Yasuda, *A sterile neutrino scenario constrained by experiments and cosmology*, Int. J. Mod. Phys. **A12** (1997), 3669–3694, hep-ph/9606411.

[Pac86] B. Paczynski, *Gravitational microlensing by the galactic halo*, Astrophys. J. **304** (1986), 1–5.

[Pan07] L. Pandolo, *Neutron- and muon-induced background in underground physics experiments*, ILIAS 4$^{\text{th}}$ Annual Meeting, Chambery, France, 2007.

[Pec77] R. D. Peccei and H. R. Quinn, *CP conservation in the presence of pseudoparticles*, Phys. Rev. Lett. **38** (1977), 1440–1443.

[Pee93] P. J. E. Peebles, *Principles of physical cosmology*, Princeton Series in Physics, Princeton University Press, 1993.

[Pen65] A. Penzias and R. Wilson, *A Measurement of Excess Antenna Temperature at 4080 Mc/s.*, Astrophys. J. **142** (1965), 419–421.

[Per96] M. Persic, P. Salucci, and F. Stel, *The Universal rotation curve of spiral galaxies: 1. The Dark Matter connection*, Mon. Not. Roy. Astron. Soc. **281** (1996), 27, astro-ph/9506004.

[Per07] W. J. Percival et al., *Measuring the Matter Density Using Baryon Oscillations in the SDSS*, Astrophys. J. **657** (2007), 51–55, astro-ph/0608635.

[Pic07] P. Picozza et al., *PAMELA: A payload for antimatter matter exploration and light-nuclei astrophysics*, Astropart. Phys. **27** (2007), 296–315, astro-ph/0608697.

[Raf97] G. G. Raffelt, *Dark Matter: Motivation, Candidates and Searches*, hep-ph/9712538.

[Rei98] J. Reichenbacher, *Untersuchung der optischen Eigenschaften grossflächiger Plastikszintillatoren für den KARMEN-Upgrade (in German)*, Master's thesis, Universität Karlsruhe (TH), 1998.

[Rho93] W. Rhode, *Study of Ultra High Energy Muons with the Fréjus Detector (in German)*, Ph.D. thesis, Universität Wuppertal, 1993.

[Rho96] W. Rhode et al. (Fréjus Collaboration), *Limits on the flux of very high-energetic neutrinos with the Fréjus detector*, Astropart. Phys. **4** (1996), 217–225.

[Rop64] L. D. Roper, *Evidence for a $P_{11}$ Pion-Nucleon Resonance at 556 MeV*, Phys. Rev. Lett. **12** (1964), no. 12, 340–342.

[Ros04] L. J. Rosenberg, *ADMX dark-matter axion search*, AIP Conf. Proc. **698** (2004), 332–340.

[Ros07] L. Roszkowski, R. Ruiz de Austri, and R. Trotta, *Implications for the constrained MSSM from a new prediction for $b \to s\gamma$*, JHEP **07** (2007), 075, hep-ph/07052012.

[Rub80] V. C. Rubin, N. Thonnard, and J. Ford, W. K., *Rotational properties of 21 SC galaxies with a large range of luminosities and radii, from NGC 4605 (R = 4kpc) to UGC 2885 (R = 122 kpc)*, Astrophys. J. **238** (1980), 471.

[Rub85] V. C. Rubin, D. Burstein, J. Ford, W. K., and N. Thonnard, *Rotation velocities of 16 SA galaxies and a comparison of Sa, Sb, and SC rotation properties*, Astrophys. J. **289** (1985), 81.

[Rub06] A. Rubbia, *ArDM: A ton-scale liquid argon experiment for direct detection of dark matter in the universe*, J. Phys. Conf. Ser. **39** (2006), 129–132, hep-ph/0510320.

[Sak65] A. D. Sakharov, Zh. Eksp. Teor. Fiz. **49** (1965), 345, [Soviet Phys. JETP 22, 241 (1966)].

[San02] R. H. Sanders and S. S. McGaugh, *Modified Newtonian Dynamics as an Alternative to Dark Matter*, Ann. Rev. Astron. Astrophys. **40** (2002), 263–317, astro-ph/0204521.

[San05a] V. Sanglard, *Recherche de la matiére noire non-baryonique à l'aide de détecteurs cryogéniques à double composante ionisation et chaleur : Analyse et Interprétation des données de l'expérience EDELWEISS-I (in French)*, Ph.D. thesis, L'Université Claude Bernard - Lyon 1, 2005.

[San05b] V. Sanglard et al. (The EDELWEISS Collaboration), *Final results of the EDELWEISS-I dark matter search with cryogenic heat-and-ionization Ge detectors*, Phys. Rev. **D71** (2005), 122002, astro-ph/0503265.

[San07] D. Santos, O. Guillaudin, T. Lamy, F. Mayet, and E. Moulin, *MIMAC : A Micro-TPC Matrix of Chambers for direct detection of Wimps*, J. Phys. Conf. Ser. **65** (2007), 012012, astro-ph/0703310.

[Sav04] C. Savage, P. Gondolo, and K. Freese, *Can WIMP spin dependent couplings explain DAMA data, in light of null results from other experiments?*, Phys. Rev. **D70** (2004), 123513, astro-ph/0408346.

[Sch90] M. Schubnell, *Untersuchung der Isotropie der kosmischen Strahlung bei Energien* $> 10^{13}$ *eV mit dem Freéjus-Untergrunddetektor (in German)*, Ph.D. thesis, Universität Wuppertal, 1990.

[Sch05] S. Schönert et al. (GERDA Collaboration), *The GERmanium Detector Array (GERDA) for the search of neutrinoless* $\beta\beta$ *decays of Ge-76 at LNGS*, Nucl. Phys. Proc. Suppl. **145** (2005), 242–245.

[Sch07] S. Scholl, *private communication*, 2007.

[Sco95] D. Scott, J. Silk, and M. J. White, *From microwave anisotropies to cosmology*, Science **268** (1995), 829–835, astro-ph/9505015.

[Sei07] W. Seidel, *The CRESST experiment*, The $10^{\text{th}}$ international conference on Topics in Astroparticle and Underground Physics (TAUP2007), September 2007.

[Ser03] G. Servant and T. M. P. Tait, *Is the lightest Kaluza-Klein particle a viable dark matter candidate?*, Nucl. Phys. **B650** (2003), 391–419, hep-ph/0206071.

[Shu00] T. Shutt et al., *A solution to the dead-layer problem in ionization and phonon-based dark matter detectors*, Nucl. Instrum. Meth. **A444** (2000), 340–344.

[SI00] D. P. Snowden Ifft, C. J. Martoff, and J. M. Burwell, *Low pressure negative ion drift chamber for dark matter search*, Phys. Rev. **D61** (2000), 101301, astro-ph/9904064.

[Sil85] J. Silk, K. A. Olive, and M. Srednicki, *The photino, the sun, and high-energy neutrinos*, Phys. Rev. Lett. **55** (1985), 257–259.

[Sli13] V. M. Slipher, *The radial velocity of the Andromeda Nebula*, Lowell Observatory Bulletin **2** (1913), 56–57.

[Sli15] V. M. Slipher, *Spectrographic Observations of Nebulae*, Popular Astronomy **23** (1915), 21–24.

[Smo92] G. F. Smoot et al., *Structure in the COBE differential microwave radiometer first year maps*, Astrophys. J. **396** (1992), L1–L5.

[Spe03] D. N. Spergel et al. (WMAP Collaboration), *First Year Wilkinson Microwave Anisotropy Probe (WMAP) Observations: Determination of Cosmological Parameters*, Astrophys. J. Suppl. **148** (2003), 175–194, astro-ph/0302209.

[Spe07] D. N. Spergel et al., *Three-Year Wilkinson Microwave Anisotropy Probe (WMAP) Observations: Implications for Cosmology*, Astrophys. J. Suppl. **170** (2007), 377–408, astro-ph/0603449.

[Sta04] T. Stanev, *High Energy Cosmic Rays*, Praxis Books in Astrophysics and Astronomy, Springer-Verlag, 2004.

[Ste89] F. Stecker, *Cosmic Gamma-Rays from Dark Matter and Antimatter Annihilation*, Nucl. Phys. **10B** (1989), 93–107.

[Suf99] Y. Sufue et al., *Central rotation curves of spiral galaxies*, Astrophys. J. **523** (1999), 136–146.

[Sum05] T. J. Sumner (ZEPLIN Collaboration), *The ZEPLIN III dark matter project*, New Astron. Rev. **49** (2005), 277–281.

[Tis07] P. Tisserand et al. (EROS-2 Collaboration), *Limits on the MACHO content of the Galactic Halo from the EROS-2 Survey of the Magellanic Clouds*, Astron. Astrophys. **469** (2007), 387–404, arXiv:astro-ph/0607207.

[Tur90] M. S. Turner, *Windows on the Axion*, Phys. Rept. **197** (1990), 67–97.

[Ull01] P. Ullio, M. Kamionkowski, and P. Vogel, *Spin dependent WIMPs in DAMA?*, JHEP **07** (2001), 044, hep-ph/0010036.

[Wan01] Y. F. Wang et al., *Predicting neutron production from cosmic-ray muons*, Phys. Rev. **D64** (2001), 013012, hep-ex/0101049.

[Wan05] H. Wang, *The ZEPLIN II dark matter detector status*, Nucl. Phys. Proc. Suppl. **138** (2005), 52–55.

[Wei34] C. Weizsäcker, Z. Phys. **88** (1934), 612.

[Wei93] Y. Wei, *The neutrino induced muon flux at the Fréjus underground experiment*, Ph.D. thesis, Universität Wuppertal, 1993.

[Wel06] J. Wellisch, *private communication*, 2006.

[Wil35] E. Williams, Math. Fys. Medd. Dan. Vid. Selsk. **XIII** (1935), 4.

[Wul03] H. R. Wulandari, *Study on neutron-induced background in the Dark Matter experiment CRESST*, Ph.D. thesis, Technische Universität München, 2003.

[Yao06] W.-M. Yao et al., *Review of Particle Physics*, Journal of Physics G **33** (2006), 1+, Particle Data Group: main publication.

[Yel02] S. Yellin, *Finding an upper limit in the presence of an unknown background*, Phys. Rev. **D66** (2002), no. 3, 032005, physics/0203002.

[Yor00] D. G. York et al., *The Sloan Digital Sky Survey: Technical Summary*, Astron. J. **120** (2000), 1579–1587, astro-ph/0006396.

[Yvo96] D. Yvon et al. (EDELWEISS Collaboration), *First results of the EDELWEISS experiment*, Nucl. Phys. Proc. Suppl. **48** (1996), 77–79.

[Zav06] E. Zavattini et al. (PVLAS Collaboration), *Experimental observation of optical rotation generated in vacuum by a magnetic field*, Phys. Rev. Lett. **96** (2006), 110406, hep-ex/0507107.

[Zio05] K. Zioutas et al. (CAST Collaboration), *First results from the CERN axion solar telescope (CAST)*, Phys. Rev. Lett. **94** (2005), 121301, hep-ex/0411033.

[Zwi33] F. Zwicky, *Spectral displacement of extra galactic nebulae*, Helv. Phys. Acta **6** (1933), 110–127.

# Acknowledgements

The completion of this thesis would not have been possible without the steady support of numerous people. First of all, I would like to thank my PhD supervisor Prof. Dr. Johannes Blümer for giving me the opportunity to work at the institute and to participate in the EDELWEISS-II project.
My special thanks go to Prof. Dr. Josef Jochum, who kindly accepted to serve as co-referee.
I would like to express my appreciation to Dr. Klaus Eitel, whose generous support during the last years enabled me to complete this thesis. I benefited greatly from his ideas and insights, his endless constructive input and his patience in countless discussions. I could not have imagined having a better advisor and mentor for my PhD. Besides, his knowledge on wine was highly appreciated during our numerous travels to France.
I have also benefited from many discussions with members of the EDELWEISS collaboration. I would particularly like to thank Dr. Gilles Gerbier for detailed discussions on my thesis and my future career plans. Thanks also to Dr. Gerard Nollez for providing me with the *Geant4* code of the innermost detector geometry.
I also thank Dr. Vitaly Kudryavtsev for the discussions on the muon flux measurements at LSM. I appreciate as well that he gave me his results from `FLUKA` simulations. Also thanks to Dr. Henrique M. Araújo for the results from *Geant4*`6.2` simulations.
A special 'merci' to Astrid Chantelauze for her contribution on the comparison with first preliminary data of the muon veto system and the relaxed atmosphere in our shared office. Special thanks also for the fun we had on top and underneath the French-Italian Alps: Vive Les Mottets!
This study has benefited from many discussions with colleagues, both in the institute and within the former VIDMAN network and since 2007 within the SFB-TR 27 cooperation.
I would like to thank Victoria Lowe and Sven Over for cross-checking on my English grammar.
The last and very special thanks go to my family, and especially my parents, for their absolute confidence in me. Their love and caring bolstered me not only during the completion of this thesis but throughout my whole life. Though having admittedly no clue about the subject of this thesis, they always make an effort to follow my lengthy explanations about astrophysics and Dark Matter.